# BENCHMARK AND EARTH ABUNDANT ELECTROCATALYSTS FOR ACIDIC WATER OXIDATION

by

Maxine J. Kirshenbaum

Submitted in partial fulfilment of the requirements
for the degree of Master of Science

at

Dalhousie University
Halifax, Nova Scotia
August 2019

# TABLE OF CONTENTS

# LIST OF TABLES

# LIST OF FIGURES

# Abstract

Solar-mediated hydrogen technology is a promising candidate for the low-carbon production of chemical fuels. Solar-mediated water electrolysis is a mature form of $H_2$ technology that functions by rupturing water molecules to release $H_2$ and $O_2$ gas. Water electrolysis can be performed at any pH, but presently only acidic conditions offer sufficient gas separation and solution conductivity. Large-scale integration of solar-mediated acidic water electrolysis is limited by the oxygen evolution reaction (OER), which requires oxidatively stable catalysts to proceed at appreciable rates and energies. The only materials known to possess acceptable levels of activity, stability and selectivity for acidic OER are iridium oxide ($IrO_x$)-based systems.

$IrO_x$ serves as a "benchmark" material against which other OER catalysts are compared. The performance of $IrO_x$ is largely determined by its method of preparation and the conditions under which it is tested, neither of which are controlled for in the literature. To catalogue the impact of fabrication and electrolyte conditions on $IrO_x$ OER performance, $IrO_x$ films were prepared using common literature techniques and evaluated under equivalent electrolyte conditions. Further, the OER performance of $IrO_x$ films was evaluated in different electrolytes and molarities. The results of this study revealed preparation-dependent OER performances and film-dependent sensitivities to electrolyte composition. Identification of fabrication- and electrolyte-dependent properties for $IrO_x$ films allows for better comparison between literature electrocatalyst systems.

The scarcity and cost of Ir limits the sustainability and scalability of water electrolysis. Earth abundant (EA) alternatives are required for this technology to be an economical large-scale energy solution. The current repertoire of EA materials for acidic OER all show poor stability and/or activity compared to analogous $IrO_x$-based systems. Titanium diboride ($TiB_2$) is a corrosion-resistant material with theorized and demonstrated catalytic behaviour. Its suitability as an acid-stable electrocatalyst for OER was investigated. It was found to have the highest chemical stability of known active EA materials for acidic OER and superior activity relative to other electrochemically-stable EA systems. However, $TiB_2$ films showed limited mechanical stability and delaminated after ~ 10 h operation.

# LIST OF ABBREVIATIONS AND SYMBOLS

OER = oxygen evolution reaction

HER = hydrogen evolution reaction

EA = earth abundant

SHC = solar-to-hydrogen conversion

PEM = polymer exchange membrane

RHE = reversible hydrogen electrode

RE = reference electrode

CE = counter electrode

WE = working electrode

$E^o$ = standard electrode potential (V)

$E_{eq}$ = equilibrium potential (V)

$E_{cell}$ = cell potential (V)

$E_{anodic}$ = anodic potential (V)

$E_{RE\ vs.\ RHE}$ = reference electrode potential relative to the RHE

$E_{H2O\ vs.\ RHE}$ = standard reaction potential for water splitting relative to the RHE

$E_{OC}$ = open circuit potential

$R_u$ = uncompensated resistance

$R_{CT}$ = charge transfer resistance

$\eta$ = overpotential

$j_o$ = exchange current density

$j$ = current density

$I$ = current

$R_{rxn}$ = reaction rate

F = Faraday's constant

n = number of $e^-$ involved in a reaction

SIROF = sputtered iridium oxide film

T-SIROF = thermally annealed sputtered iridium oxide film

AIROF = anodic iridium oxide film

T-AIROF = thermally annealed anodic iridium oxide film

DC = drop cast

SC = spin coat

ED = electrodeposited

T-ED = thermally annealed electrodeposited

TD = thermal decomposition

TDPS = thermal decomposition of a precursor salt

FTO = fluorine-doped tin oxide

DI = deionized

LSV = linear sweep voltammetry

CV = cyclic voltammetry

CA = chronoamperometry

CC = chronocoulometry

CP = chronopotentiometry

EIS =electrochemical impedance spectroscopy

XPS = X-ray photoelectron spectroscopy

SEM = scanning electron microscopy

F.E. = Faradaic efficiency

XRD = X-ray diffraction

g-XRD = grazing incidence XRD

ICP = inductively coupled plasma

ICP-OES = inductively coupled plasma optical emission spectroscopy

B.E. = binding energy

$\Phi_m$ = material work function

$E_k$ = kinetic energy

$h$ = Plank's constant

v = frequency

$A_{geo}$ = geometric surface area

ECSA = electrochemically active surface area

$C_{DL}$ = double-layer capacitance

$\Delta\eta = \eta_{t=24\ h} - \eta_{t=0}$ = overpotential instability

# ACKNOWLEDGEMENTS

I’d like to thank my supervisor, Dr. Mita Dasog, for all her support and mentorship. I’d also like to thank the Dasog group for their support and motivation.

# CHAPTER 1. INTRODUCTION

## 1.1 Background

The current climate crisis is largely, if not entirely, driven by anthropogenic activity.[1] Immediate and serious action is required to prevent the global mean temperature from rising >1.5 $^{\circ}$C above pre-industrial temperatures before 2050.[1,2] Greenhouse gases (GHG) play a major role in the increasing surface temperature of the planet. GHGs trap incident solar radiation in the atmosphere, reducing the energy that escapes the Earth. This disrupts the planetary energy balance and increases its radiative forcing.[3] Carbon dioxide ($CO_2$) and methane ($CH_4$) are the two most abundant GHG in the atmosphere.[1,3,4] Many environmental and climate change protocols are focused on the reduction of carbon emissions due to the potency of these GHG.[1,2,5] Reducing carbon emissions will help slow the rate of climate change, with faster and stricter actions proving to be the most promising mitigation strategies.[6]

Nations are starting to draft and implement ambitious targets to meet international climate guidelines.[7] These targets include strategies for shifting the dependency of the energy industry towards renewable energy.[4,6] Currently, the fossil fuel industry serves as the largest source of carbon emissions and the amount of carbon emitted globally increases every year.[4,8] The rising carbon emissions are reflective of the growing global population, industrialization/colonization of rural and developing spaces, as well as increasing consumption by Westernized societies.[4,6,8,9] In order to satisfy the ever-growing global energy demands while simultaneously meeting the emissions targets being set worldwide, the existing energy infrastructure needs to be replaced with low-, or

zero-, carbon alternatives. Furthermore, the energy infrastructure being introduced into "developing" areas must be built around renewable energy.[1,6,7] Wide-spread and fast transition to renewable-based energy economies, in conjunction with the deployment of carbon sequestering technology and energy conservation practices, is the only way the effects of climate change might be slowed to a rate that meets 2050 targets.[4,6]

Efforts are being made to transition global economies to low carbon energy sources such as solar, wind, hydro, tidal, biomass, and geothermal sources. However, there are limitations inherent to renewable sources that must be addressed for them to be globally adopted.[10–13] Some of these limitations are similar to those of fossil-fuel sources, such as the variable regional accessibility to dense energy "reservoirs" for large-scale energy extraction. The world is currently dependent on countries that have access to large fossil-fuel reserves for energy.[4,11,14] The ability of a region to rely on a certain form of (renewable) energy depends on the surrounding geography and climate. Tidal and wave energy are limited to coastal regions while hydro energy is inaccessible to arid regions.[14] Wind energy is restricted to predictably windy areas which also tend to be coastal.[15] Solar energy is arguably a universal resource, however large solar operations are most compatible in places with high radiation year-round.[13–15]

The intermittency of renewable energies conflicts with societal energy demands, which require consistent and predictable energy access.[9,10] To overcome the mismatch in energy supply vs. demand, renewable energy must be captured while it is available and stored in a different energy form. Doing so allows reservoirs of renewable energy to be built up and accessible for periods of high demand. This also introduces the opportunity to replace fossil-fuel reserves, thereby shifting the energy landscape towards low-carbon

targets.[10,11] Solar energy is the most abundant energy source available to Earth and considerable research effort has been focused on the development of solar-mediated renewable technologies.[9,16,17] Converting solar energy into chemical fuels (densest form of energy after nuclear) is an attractive solution as it can be stored, transported, and used on demand. Research in this field has focused on converting $H_2O$ and $N_2$ into $H_2$ and $NH_3$,[18,19] respectively, as the products can be fed to a fuel cell to generate electricity without generating $CO_2$ as a by-product during combustion (Figure 1.1).

Figure 1.1: Scheme of hydrogen technology. a) renewable energy is converted to

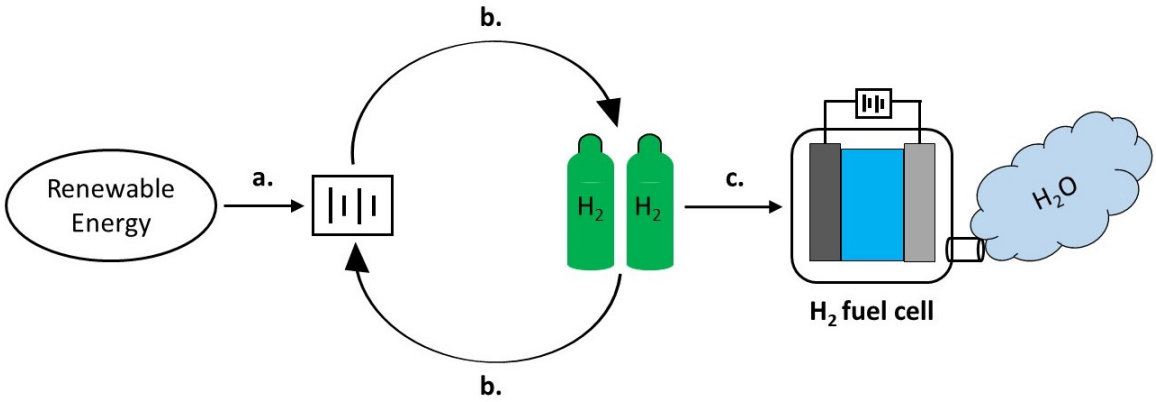


electrical energy, b) electrical energy is converted to chemical energy (or vice-versa) and, c) chemical energy ($H_2$) is used in a combustion fuel cell.

Currently, $H_2$ is primarily manufactured by way of the fossil fuel industry.[18,20,21] Production methods include steam reformation, partial oxidation and gasification of different forms of carbon and hydrocarbons (Equations 1.1-1.4, respectively).[11,12]

$$CH_4 + H_2O \rightarrow CO + 3\,H_2 \qquad (1.1)$$

$$CO + H_2O \rightarrow CO_2 + H_2 \qquad (1.2)$$

$$C_{10}H_{20} + 5\,O_2 \rightarrow 5\,CO + 10\,H_2 \qquad (1.3)$$

$$7\,C + 2\,O_2 + 4\,H_2O \rightarrow 2\,CO_2 + 4\,CO + CH_4 + 2\,H_2 \qquad (1.4)$$

Each production route above results in the formation of GHGs and toxic gases as reaction by-products. Water electrolysis can be used as a low-carbon method of $H_2$ production, especially when it is coupled to a renewable power source. Solar-mediated water electrolysis offers a chemical fuel formation process that produces $H_2$ from $H_2O$ instead of carbon precursors, thereby reducing industry dependence on fossil fuels.[18] Chemical fuel species such as $NH_3$ can also be formed by performing solar-mediated water electrolysis in the presence of $N_2$.[22]

All solar-mediated $H_2$ generation schemes rely on the splitting of water molecules to extract $H_2$ gas.[11] As shown in Figure 1.2, each production method also leads to the formation of $O_2$. Water thermolysis uses solar-generated heat to convert water from a liquid to a vapour.[11,23] The water molecules dissociate when heated and the constituent atoms collide to form $H_2$ and $O_2$ gas (Figure 1.2A). This method of water splitting requires high temperatures (>1000$^{\circ}$C) and typically uses concentrated solar thermal radiation.[11,18] Biophotolysis refers to the generation of $H_2$ using biological organisms, often bacteria or algae, that have been selected for based on their $H_2$ production capabilities (Figure 1.2B).[11] This approach to $H_2$ generation takes advantage of the photosynthetic pathways of these organisms and the by-production of $H_2$ that results from the digestion of sugar and other hydrocarbons. Photocatalytic (PC) and photoelectrochemical (PEC) water splitting are similar and often overlapping technologies whereby incident solar radiation is used to excite semiconducting materials that facilitate the reduction and oxidation of water molecules at their surface (Figure 1.2C

and D).[11,12,24] The key difference between the two technologies is that PC systems do not use external electrical biases to generate $H_2$, whereas PEC cells do use a voltage source. Water electrolysis is similar to PEC, however it does not involve the direct conversion of solar radiation into chemical energy.[24] Instead, the incident solar radiation is first transformed into electrical energy using an array of photovoltaic cells. The resulting electricity is used to facilitate the splitting of water electrochemically, thereby producing $O_2$ and $H_2$ gas (Figure 1.2E).

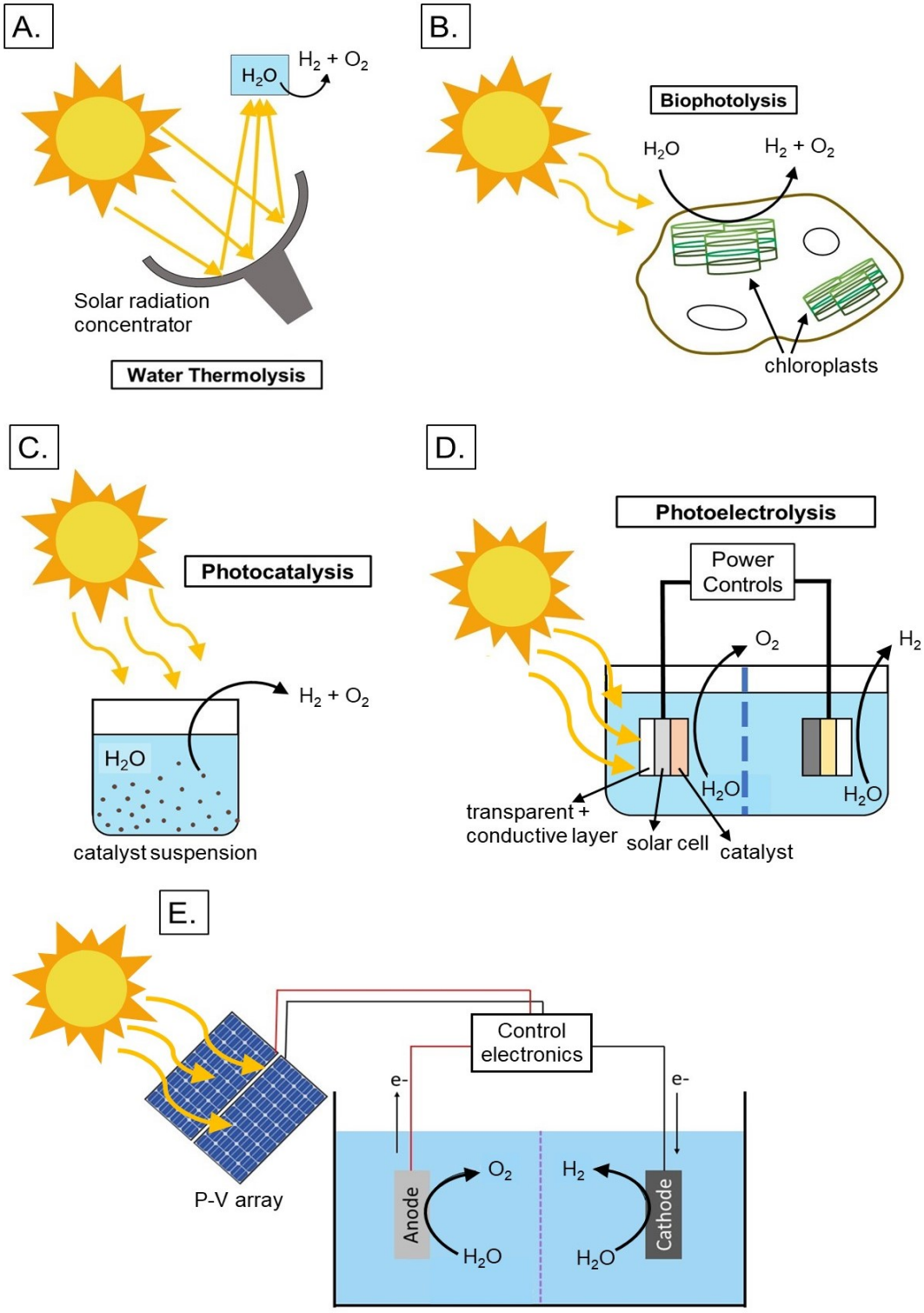


Figure 1.2: Simplified illustrations of solar-mediated $H_2$ production technologies. A) solar themolysis (using concentrated solar radiation), B) biophotolysis (facilitated by a photosynthetic organism), C) PC (using a photocatalyst suspension), D) PEC (tandem set up), E) water electrolysis (using a P-V array).

Water electrolysis is the most mature of the solar-mediated $H_2$ production technologies.[12] Water electrolysis technology has been used at industrial scales since the 1900s,[20] however solar-mediated systems are only just starting to be developed for such purposes. Traditionally, water electrolysis has been mediated using electricity that originates from non-renewable sources.

## 1.2 Water electrolysis

Water electrolysis is an electrochemical process whereby water molecules are decomposed into two component gases, $O_2$ and $H_2$. Since the reaction involves the breaking apart of water molecules it is often referred to as the water splitting reaction.[24,25] The overall electrochemical reaction can be written as

$$2\,H_2O \rightarrow 2\,H_2 + O_2 \qquad E° = 1.23\,V \qquad (1.5)$$

Water electrolysis involves two half reactions, a reduction (cathodic) reaction to produce $H_2$ and an oxidation (anodic) reaction to produce $O_2$. These are referred to as the hydrogen evolution reaction (HER) and the oxygen evolution reaction (OER). The mechanism of the two half reactions depends on the pH of the electrolyte used in the electrochemical cell. Water splitting can be performed under acidic, neutral and/or basic pH conditions. Under basic conditions, hydroxy ions ($OH^-$) are the dominant ionic species and the half reactions can be summarized as[26]

$$4\,OH^- \rightarrow O_2 + 2\,H_2O + 4\,e^- \qquad (1.6)$$

$$2\,H_2O + 2\,e^- \rightarrow H_2 + 2\,OH^- \qquad (1.7)$$

Under acidic conditions, protons are the dominant ionic species and the ionic and cathodic reactions can be written as[26]

$$2\,H_2O \rightarrow O_2 + 4\,H^+ + 4\,e^- \qquad (1.8)$$

$$2\,H^+ + 2\,e^- \rightarrow H_2 \qquad (1.9)$$

The half reactions under neutral conditions are typically written the same as for acidic conditions or using the half reactions where $H_2O$ is a reagent (equations 1.7 and 1.8).[27]

The reactions associated with the HER and OER are pH-dependent. This is illustrated by the Pourbaix diagram shown in Figure 1.3,[28] where the species involved in, as well as the relative amount of energy demanded by, the half reactions shifts along with pH. The reaction energies, or potentials, at a given pH are determined using the Nernst equation,

$$E_{eq.} = E^\circ + \frac{RT}{nF} ln \frac{[ox]}{[red]} \qquad (1.10)$$

where $E_{eq.}$ is the equilibrium potential, $E^o$ is the standard reaction potential, R is the gas constant, T is temperature, n is the number of electrons involved in the half reaction, F is Faraday's constant and [ox], [red] is the oxidation and reduction species concentration, respectively.[29] The Nernst equation predicts the minimum energy required for a reaction proceed. Equation 1.10 can be rewritten in terms of pH when $H^+$ is used as the reduction species ([red]) and $P_{O_2} \sim 1$ atm,

$$E_{eq.} = E^\circ - \frac{RT}{nF} ln\,(\mathrm{pH}) \qquad (1.11)$$

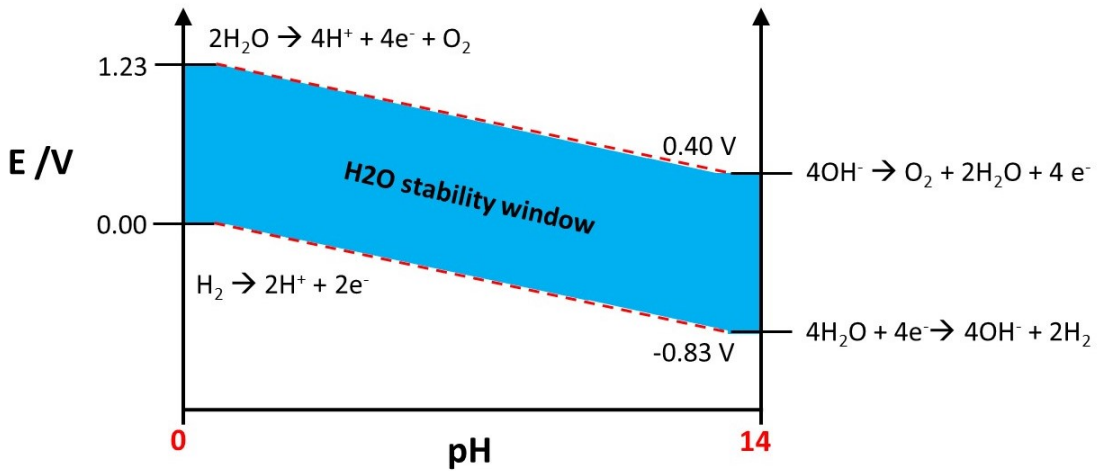


Figure 1.3: Pourbaix diagram for the water splitting process.[28]

Water electrolysis can be performed under basic, neutral or acidic conditions. While neutral conditions are generally the safest and least corrosive, the solution resistance and high reaction potentials result in prohibitive operational energy requirements.[16] Water electrolysis performed in a high or low pH regime is more efficient due to the presence of charge carriers in the electrolyte. Charge carriers assist in the transport of ions through solution, thereby minimizing resistive energy losses.

Base-mediated water electrolyzers are currently employed in select industrial settings,[18] however their integration is limited by cost and safety factors.[12,14,16,30] Basic solutions tend to be more expensive than acidic solutions and require more complex treatment of waste/spent electrolyte. Furthermore, water electrolyzers rely on specialized membranes to selectively separate the OER and HER compartments such that ion transport is allowed but $O_2$ and $H_2$ are blocked. Alkaline water electrolyzer membrane technology is currently limited by sub-par membrane permeabilities.[16,26] This poses both

safety and device efficiency concerns since $O_2$ and $H_2$ can react explosively under pressure/heat and poor charge transport increases energy requirements.

Membrane technology is more progressed for acid- than base-mediated water electrolyzer systems. This is primarily due to advances in proton-exchange membrane (PEM) technology because the cells are usually acidic.[21,31,32] PEMs operate in a manner similar to the water electrolyzer cell, however one side of the anode and cathode are attached to a conductive membrane that replaces the liquid electrolyte phase. From a materials perspective, the main factor limiting the scope of acid-mediated water electrolysis is the anode.[12,16,20,32] Development of more affordable and efficient water oxidation catalysts would allow the technology to be a realistic option for chemical fuel production.

Water splitting systems require more energy to drive a reaction forward than that predicted by the Nernst equation ($E_{eq}$). This additional energy is known as the overpotential, η. In acidic electrolyte, the η required to elicit $j = 10\ mA \cdot cm^{-2}$ for OER exceeds that of HER. This is in part due to the relative number of electrons transferred during the two half reactions. HER is a 2 $e^-$ transfer process whereas OER is a 4 $e^-$ transfer process. There are more energetic and kinetic barriers implicated by the 4 $e^-$ transfer pathway of OER than the 2 $e^-$ transfer pathway of HER.[27,31,33]

### 1.3 Acid-mediated water electrolysis

The OER is a kinetically complex reaction involving up to 4 $e^-$ transfers. There have been numerous mechanisms proposed for the OER, two of which are shown in

Figure 1.4.[34] For an ideal system, Tafel analysis can be performed to elucidate the rate-limiting step (RLS) on a material surface. The Tafel equation can be written as

$$\eta = b \cdot \log(j) - \log(j_o) \qquad (1.12)$$

where $b$ represents the Tafel slope and $j_{ox}$ is the oxidative current density.[29,33,35] Every step in a reaction mechanism can be assigned a characteristic Tafel slope. The Tafel slope measured for a material therefore provides insight on the RLS at the surface. In some cases, the Tafel slope can be used to approximate back to a suitable reaction mechanism.

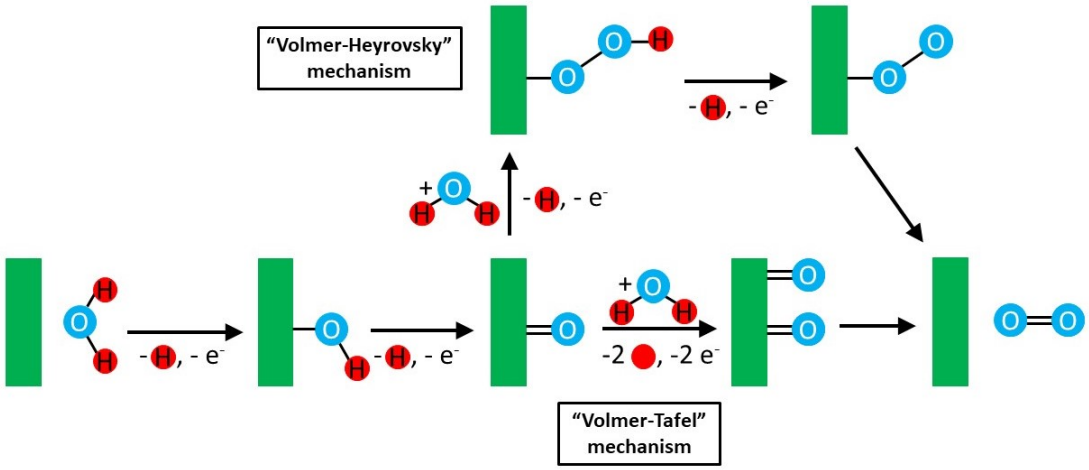


Figure 1.4: Simplified schematic of two proposed OER mechanisms.

For OER, mechanistic studies are difficult to perform due to the number of $e^-$ transfers required by the reaction and the existence of multiple proposed reaction mechanisms. The information available through Tafel analysis is limited because different OER mechanisms have the same Tafel slopes associated with different RLSs. Furthermore, there are specific conditions that must be met in order for Tafel analysis to provide meaningful mechanistic information on multistep $e^-$ transfer processes, including the assumption of a single, linear reaction mechanism and the absence of surface-altering

processes at the electrode surface (e.g., film dissolution or adsorption).[29] High bubble activity, structural rearrangement and/or surface corrosion tend to occur in parallel to OER and can lead to Tafel slopes that are not representative of the OER surface reactions.[36] Tafel plots can also show discontinuities for materials over log(*j*), indicating a change in the active surface.[35] Owing to these complexities, there is still uncertainty surrounding the processes involved in the OER.

Tafel analysis can be used to compare the intrinsic activity of a material and the charge-transfer efficiency of the overall electrode system.[36] If Figure 1.5 is taken to represent two different OER systems, then material B shows higher intrinsic activity relative to material A because a small change in potential generates a proportionally large current response. Assuming the measured current is related to Faradaic (i.e., charge transfer) processes, this implies the surface of B is able to facilitate an increased number of reactions with less energetic input. Similarly, if Figure 1.5 represents two electrodes of the same material, then the charge transfer efficiency of electrode B exceeds that of electrode A. Parameters such as film-support contact and surface inhomogeneity can influence the charge-transfer properties of a given electrode and can mask the activity of the surface material.[37] Care must be taken when collecting and interpreting Tafel slopes to ensure the information being gained is representative of the active material.

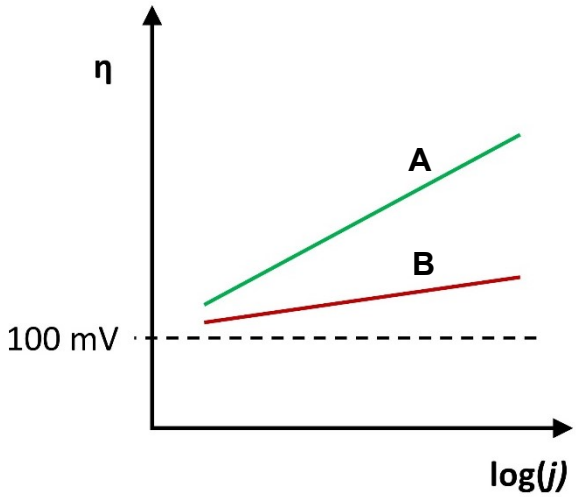


Figure 1.5: Tafel plot for an anodic process at the surface of two different materials (A, B).

The kinetic complexity of OER pre-disposes it to a high reaction η.[35,38,39] Electrocatalysts can be used to lower the kinetic barrier of an electrochemical reaction, thereby decreasing the associated η. A good OER electrocatalyst can significantly reduce the overall energy demanded by a water splitting system. Furthermore, active electrocatalysts typically have small Tafel slopes (high catalytic efficiency). While stable and active HER electrocatalysts have been demonstrated for acid-mediated water electrolysis,[40,41] the harsh oxidative conditions of acidic OER severely limit the scope of potential electro-oxidation catalysts.[27,31,41]

## 1.4 Heterogeneous acid-stable water oxidation catalysts

### *1.4.1 Acidic OER catalyst materials*

Catalytic materials work by lowering the energetic barrier (activation energy) of a reaction, thereby providing a more energetically accessible route for product formation.

Electrocatalytic materials lower the activation energy of an electrochemical reaction, thereby lowering the overpotential required to drive it forward.[39,41,42] The ideal electrocatalyst would facilitate the electrochemical reaction of interest with little η requirement.[27] This is rarely the case, especially under harsh operational conditions such as those required for acid-mediated water electrolysis.[16,27,31] Instead, target η can be set using application-based parameters and/or operational requirements. For solar-to-hydrogen conversion (SHC) technology operating under 1 sun illumination, the goal is to keep the total η requirement (i.e., $\eta_{OER} + \eta_{HER}$) within 500 mV.[27,41,43] With ~100 mV put aside for HER, the η target for OER is ~ 350 mV. Figure 1.6 shows a representative activity-stability plot used to evaluate the evolution of electrocatalyst(s) η over time. Materials with low and stable η appear low on the plot and close to the bisecting line. If a material has an that increases over operational time, it will be displaced from the bisecting line and appear higher on the plot. Promising candidates for integration into SHC technology exhibit small and stable η.

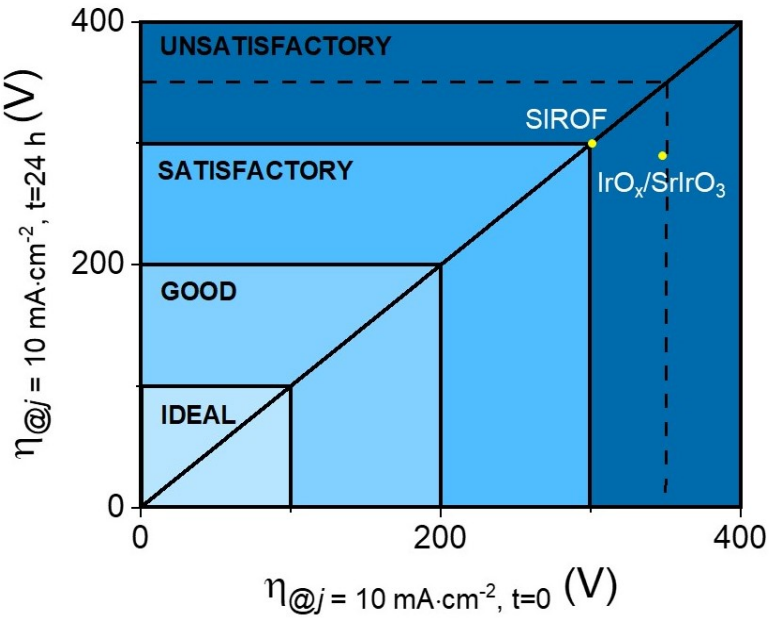


Figure 1.6: OER catalyst performance screening using figures of merit for SHC technology (under 1 sun illumination). Two literature $IrO_x$ systems are shown (sputtered $IrO_x$ (SIROF),[44] $IrO_x/SrIrO_3$[45]) for 0.5 M $H_2SO_4$. Dashed lines indicate $\eta_{OER}$ targets.

The harsh anodic and oxidizing conditions required by acidic water oxidation effectively corrodes many materials and renders them inactive and/or unstable. To date, the only materials that have been shown to have acidic OER activities within ~350 mV are from the Pt-group metals. In general, it was found that the order of OER reactivity for these metals follows to order: Os > Ru > Ir > Pt >Au at $j$ = 5 mA·cm$^{-2}$.[31,46] Os has effectively been ruled out due to its rapid dissolution under operational conditions and high toxicity.[46] Ru is the next most active of the metals, however it is also unstable under acidic conditions at OER potentials.[25,31,46] In comparison, Ir films prepared and tested using the same conditions show improved stability to Ru films.[46,47]

*1.4.2 Catalogue of Ir and IrOx films for OER*

There exists a multitude of Ir and $IrO_x$ systems with proficiencies for the OER in acidic media.[44,48–52] The properties of the oxide systems show fabrication-dependent properties.[53–60] In the literature, films tend to be grouped based on the fabrication technique. However, the fabrication conditions and film support used can blur the lines between film categories.[37,49,61]

Figure 1.7 outlines the most commonly cited $IrO_x$ systems in the OER literature. It should be noted that $IrO_x$ systems based on Perovskite[45] and other specialized material classes are not included. Ir metal electrodes form a thin oxide film at their surface upon exposure to OER potentials. These systems show high OER activity but undergo rapid dissolution and therefore deactivation.[46,49,50,62,63] Ir metals films can be anodically or thermally pre-treated to form thicker oxide films. Anodic oxidation of Ir films (AIROFs) is performed by repeated potential cycling Ir substrates (typically in the range of $0.4 < E < 1.3\text{-}1.4$ V vs. RHE) or through application of a constant anodic potential,[64–67] with the former being shown to invoke competitive Ir dissolution mechanisms during film growth.[63] The cycling range and rate used to grow the oxide influence the structure of the formed film, with shorter timescales and lower anodic potentials ($E_{anodic} < 1.0$ vs. RHE) forming adsorbed films, compact oxides at longer timescales and higher anodic potentials ($E_{anodic} > 1.0$ V vs. RHE) and a porous film forming after repetitive cycling with the compact form.[50,64,68] It is the porous $IrO_x$ form that shows high OER activity. Because the films are grown directly from the metal substrate, the film-support interfacial contact is strong, however AIROFs are highly susceptible to corrosion at OER potentials and thicker films show reduced mechanical stability.[50,69]

Thermally annealing AIROFs (T-AIROFs) increases the stability of the films but can decreases the activity relative to the hydrated form.[49] Geiger et al.[62] showed a non-linear dependence of film activity and stability on annealing temperature, with moderate annealing conditions (100-300 °C) leading to an increase in film stability but loss of activity and higher temperatures (300 °C < T ≤ 400 °C) showing improved stability with recovery of some activity. Thermal oxidation of Ir metal surfaces leads to the formation of compact oxide films (T-Ir) that show reduced activity and improved stability relative to Ir films and AIROFs.[47,49,62] T-Ir and T-AIROF films show converging activity and stability at moderate temperatures,[49] however T-Ir films show lower activity and greater stability at higher temperatures (< 500 °C).[62] T-Ir have been shown to suffer reduced stability when annealed at T ≥ 600 °C but it is not currently known why this stability inversion is observed.[62] AIROFs are amorphous films, as are T-AIROFs and T-Ir films annealed at low to moderate temperatures (≤ 400 °C).

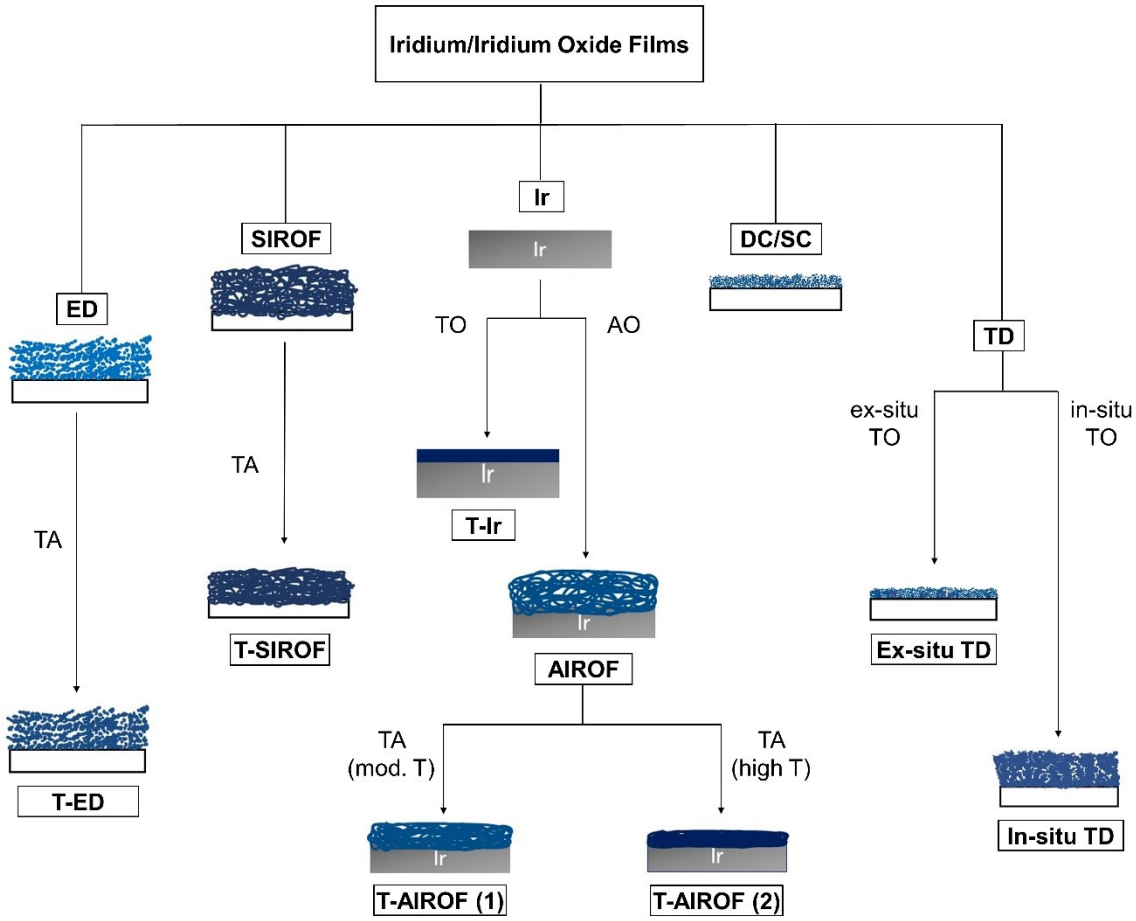


Figure 1.7: Flow-chart of various $IrO_x$ films. (AO = anodic oxidation, TO = thermal oxidation, TA = thermal annealing; mod. = moderate).

Sputtered $IrO_x$ films (SIROFs) form porous, amorphous films. The porosity, crystallinity and surface morphology of SIROFs are dependent on the sputter deposition conditions, with higher ratios of $O_2$ leading to less dense and more amorphous films,[70] higher chamber pressures forming rougher films,[71] and higher temperatures resulting in more crystalline films.[72,73] The electrochemical properties of SIROFs are in turn influenced by the deposition conditions. SIROFs appear to have thickness dependent OER performances, with thicker films showing lower activities, however the relationship between OER performance and film thickness does not appear to be well characterized.[74]

SIROFs have been compared to AIROFs in terms of activity but show markedly better η-stability.[44] While SIROFs are reported to exhibit high chemical stability, no evidence (e.g., dissolution profiling) was provided to support the claims.[44] Anodic oxidation of SIROFs using cyclic voltammetry (CV) cycling (-0.4 < E <1.3 V vs. RHE) has been shown to form a more open-pore film.[74] Thermally annealing SIROFs (T-SIROFs) in air leads to a phase change and dehydration, although the temperatures of such transformations appear depend on the film deposition and annealing conditions.[72,73,75] No comparative OER performance studies have been performed for T-SIROFs and SIROFs, however T-SIROFs do appear exhibit reduced OER activity relative to SIROFs.[60] There do not appear to be electrochemical stability comparisons available for SIROFs and T-SIROFs at this time.

Electrodeposited films can be prepared through the electrodeposition of $Ir(OH)_n^{x-}$ using CV,[76] chronoamperometry (CA)/chronocoulometry (CC)[77,78] or chronopotentiometry (CP).[79] The resulting films are hydrous and have surface morphologies and electrocatalytic properties that are dependent on the pH, temperature and composition of the deposition solution, as well as the electrochemical technique used for the deposition.[60,78,80] In general, ED films show comparable electrochemical stability and reduced OER activity relative to AIROFs. The pH-dependence of ED film electrochemical properties varies, with some films reported to exhibit potential-pH shifts[79] and others found to have pH-independent OER characteristics.[78] All reported ED films appear to be chemically unstable under acidic OER conditions.[78–80] Annealing T-ED films at moderate temperatures (100-300 °C) appears to improve the cyclability and mechanical stability of the films,[78,80] however a thorough investigation on the influence

of annealing temperature on ED film OER properties does not appear to have been done for this system. It is possible that such a study would reveal a similar trend to the one observed for AIROFs.

Particle suspensions can be drop-cast or spin-coated (DC/SC) onto support surfaces. The activity of such films is dictated by the active $IrO_x$ species and its mass-loading. DC/SC films of nanostructured $IrO_x$ show high activities relative to films composed of larger $IrO_x$ particles,[81–83] which is expected based on the larger surface area of nanomaterials.[83–85] The stability of DC/SC films is limited by the poor mechanical adhesion of the particulate films at moderate to high OER potentials. Most DC/SC systems use conductive polymer membranes, such as Nafion, as binder solutions to improve the contact of particles to other particles and to the support. However, the binder can contribute to film aggregation under operational conditions. Use of binders also restricts the thermal treatment of films to temperatures ≤150 °C,[86] which in turn limits the improvement of mechanical stability typically observed for higher-temperature annealing.[27,61]

Thermal-chemical films are formed by the decomposition of precursor Ir complexes (TD). Historically, chloride precursors[57,87–90] have been used but acetate precursors are also feasible.[37] Decomposition can be performed in-situ on the support[37,56,87] or separately (ex-situ) in a reaction vessel.[57] Ex-situ TD films are formed from a slurry of the decomposed powder product, which can be drop-cast or painted onto the support. Films formed in the presence of the support tend to be more mechanically stable relative to ex-situ films, which translates to better electrochemical stability.[61] The deposition process of ex-situ films is analogous to DC/SC films, thus similar contact

issues arise. TD films show high OER activities when they are prepared at moderate temperatures and lower activities when prepared at higher temperatures,[37,81,91] with the inverse trend being observed for operational stability. The electrochemical properties of TD films are dependent on the deposition solvents and support substrate,[37,51,91] with the former probably being most relevant to ex-situ TD films. TD films tend to be amorphous, with higher decomposition temperatures yielding films with larger crystallites.[37,91]

### *1.4.3 Earth-abundant water oxidation catalysts*

Electro-oxidation catalysts for solar-mediated acidic water electrolysis must show high activity, stability and selectivity under operational conditions. These conditions are strongly oxidizing due to the acid electrolyte and high anodic potentials ($E_{cell}$ > 1.23 V). Ru-based systems are unstable under oxidative conditions and thus are not compatible with this technology. Ir oxide systems show improved stability but lower activity compared to $RuO_x$ systems prepared and studied under equivalent conditions.[46,47] Currently, $IrO_x$ is the only family of materials known to possess a necessary mix of activity and stability under acidic OER conditions.

The growing demand for renewable energy technology and limited database of acid-stable OER catalysts has led to research efforts in the development of low Ir-loading anode materials. Loading can be reduced by maximizing the surface area and specific activity of $IrO_x$ system and/or mixing $IrO_x$ with more abundant materials (e.g., $Ta_2O_5$, $TiO_2$, $SnO_2$).[45,88,89,92,93] Ir-based materials will likely play a transitionary role in the integration of hydrogen technology within the broader energy landscape.[11] However, the

cost and limited abundance of Ir make it an unsustainable catalyst material for long-term, large-scale water electrolysis. It will become necessary to build energy systems using Earth-abundant (EA) materials, thus it is necessary to develop EA replacements.

There is a global research effort to develop EA electrode materials for water splitting systems. Many families of EA materials have been shown to possess high OER activity and stability under basic conditions, partly because the potentials required for base-mediated water oxidation are less anodic than those of acid-mediated OER.[24,41,43,94] In contrast, fewer than 10 EA systems have been found to possess moderate-to-good activity towards acidic OER (Figure 1.8).[41,95–100] Nearly all show severe stability limitations, either chemical and/or mechanical in nature, and those with the most stable electrochemical performance tend to show unacceptable levels of chemical leaching. $IrO_x$-based electrocatalysts have been, and continue to be, used to investigate the properties inherent to active acid-stable water oxidation catalysts.

| Catalyst | η /mV |
|---|---|
| $Ni_xMn_{x-1}Sb_{1.6-1.8}$ | 735 |
| Ba[Co-POM] | 289 |
| $Ni_2Ta$ (polycrystalline) | 570 |
| $CoFePbO_x$ | ~700 |
| $Co_3O_2$ | 570 |
| $TiB_2$ | 560 |

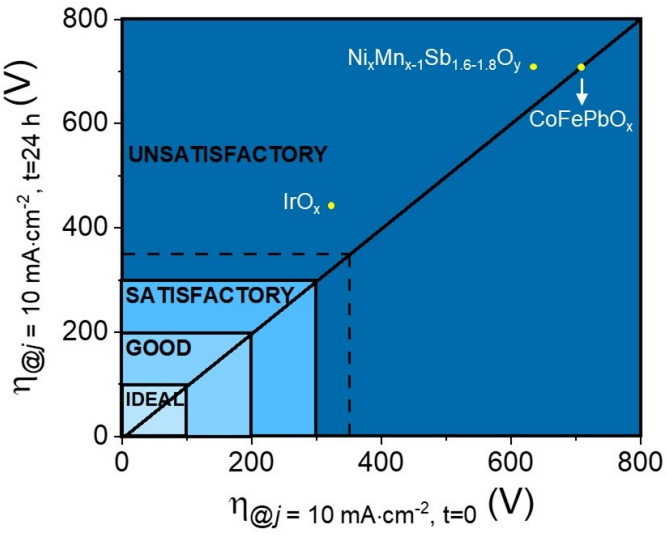


Figure 1.8: Activities of Earth abundant materials for OER in acidic media and the overpotential stability plot of EA systems[95,100] for 24 h electrolysis at $j$ = 10 mA · $cm^{-2}$ 1.0 M $H_2SO_4$. An $IrO_x$ benchmark system is included for reference.[41]

*1.4.4 Benchmark protocols for OER and HER electrocatalyst screening*

Over the past few years there has been a movement towards developing a standardized means of evaluating materials for potential water splitting applications. Providing community-wide guidelines for the way results are reported enables better comparison between materials. McCrory et al.[41] detailed a general benchmarking protocol for assessing the activity, selectivity and composition of HER and OER catalyst systems. The guidelines put forward crucial experimental figures of merit, such as testing/recording catalyst activities at $j$ = 10 mA · $cm^{-2}$ and using 1.0 M electrolyte solutions. These parameters should help streamline the evaluation of materials compatibility with solar water splitting devices operated under 1 sun illumination because they reflect probable commercial cell conditions.

Techniques such as X-ray photoelectron spectroscopy (XPS), chronopotentiometry (CP), chronoamperometry (CA) and voltammetry are used to assess the composition, stability and activity of OER materials, respectively. Ideally, the long-term stability, activity and selectivity of a material should be reported. CP allows the electrochemical stability and activity of a material at $j = 10\ \mathrm{mA \cdot cm^{-2}}$ to be evaluated for a defined time period. Alternatively, extended CA experiments performed at a previously defined $\eta_{@j\,=\,10\ \mathrm{mAcm\text{-}2}}$ can be used for stability measurements. The hallmark of a stable material is a potential (CP) or current density (CA) that is stable over operational time. However, materials can exhibit stable electrochemical activity while simultaneously suffering from chemical instability. Complimentary analysis of electrolyte composition should be done in parallel with CP/CA experiments to assess the (chemical) stability of a material over the experimental timeframe. Faradaic efficiencies afford a measure of catalyst selectivity under operational conditions. When recorded over a few hours or days, the results can reveal time-dependent selectivity.

## 1.5 Motivation for Research

The research detailed in this report was completed to improve the understanding and repertoire of anodic materials for the acid-mediated water oxidation reaction. The systematic evaluation of electrocatalysts requires new systems to be studied in comparison to a model system. This model system is usually the best studied and/or performing material for a given class of electrolysis and can be referred to as the "benchmark" catalyst system. In the case of acidic OER, the benchmark material system

is $IrO_x$. There is no standardized means of preparing $IrO_x$ films and until recently there were no benchmarked conditions for studying these systems. While $IrO_x$ has been extensively studied, many of these studies fall outside the context of modern OER research/application.

A systematic evaluation of different $IrO_x$ film types in different acidic environments was performed using benchmarked figures of merit for solar-mediated OER. Catalyst film properties show a strong dependence on fabrication and characterization conditions. The goal was to compare how different films composed of the same benchmark material performed under conditions relevant to SHC technologies. Furthermore, the influence of electrolyte species and concentration on the OER performances of $IrO_x$ films was investigated using common literature electrolyte conditions. The study serves as a point of reference for the literature to better understand of how electrolyte impacts the performance of $IrO_x$ films and may allow for more meaningful comparison between literature systems.

Following the investigation of the benchmark system, a class of EA materials was investigated as potential acid-stable electro-oxidation catalysts. There is a need to develop EA catalyst systems that are compatibles electrodes for scalable water splitting devices. The quest for active, acid-stable EA anode materials has shown slow progression due to the inherent instability of tested systems in corrosive environments. Transition metal borides are known to be stable under oxidative conditions and are even used as corrosion-resistant coatings in industrial settings. Computational studies have shown them to have attractive d-band features for catalysis.[101–103] The conductive nature of

metal borides, as well as their stability characteristics, suggested this class of materials to be suitable catalyst candidates for the acid mediated OER.

# CHAPTER 2. EXPERIMENTAL TECHNIQUES

## 2.1 Electrode Preparation

Electrodes were prepared using fluorine-doped tin oxide (FTO) glass substrates as catalyst film supports (Figure 2.1A). FTO-glass substrates were purchased from Sigma-Aldrich. All FTO-glass substrates were ultrasonicated for at least 15 minutes in DI water, acetone and isopropanol or ethanol, respectively. Substrate were left to dry before film deposition and/or electrode preparation.

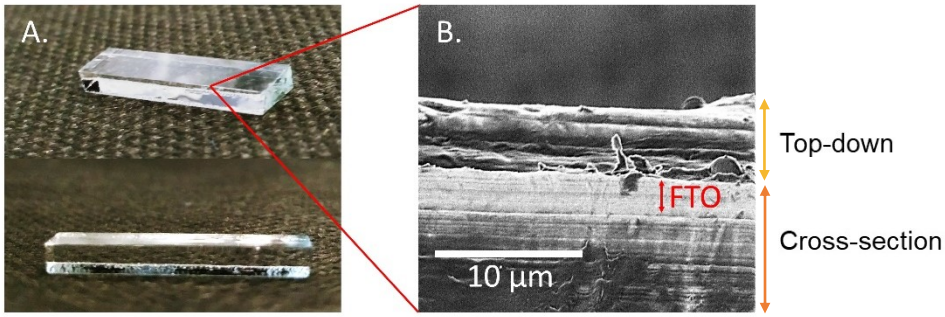


Figure 2.1: A) Images of an FTO-glass substrate and, B) SEM image of FTO film on a glass substrate.

Figure 2.2 illustrates the process followed for electrode preparation once a catalyst/FTO-glass substrate was ready for electrochemical investigation. Solid copper (Cu) wires (#22 gauge, Elenco®) were stripped on both ends. One end was then coiled, and the uncoiled end was fit through a glass tube. The coiled wire was placed flat against one side of an FTO-glass substrate and the coil and surrounding area were coated with silver (Ag) paint (Figure 2.2A, B). The Ag paint was used to establish an electrical connection between the conductive FTO surface and Cu wire. The Ag coating was left to

dry for at least 30 minutes before being coated with a layer of clear nail polish (Figure 2.2C). Nail polish increased the strength of the support-wire attachment prior to application of the epoxy. The coat was left to dry for at least 30 minutes. Once dry, epoxy was used to seal off all areas other than the desired active surface (Figure 2.2d). Epoxy coatings were cured for at least 12 h before electrodes were exposed to aqueous environments. Thin film electrodes were prepared by coating FTO-glass with a catalyst film prior to electrode fabrication.

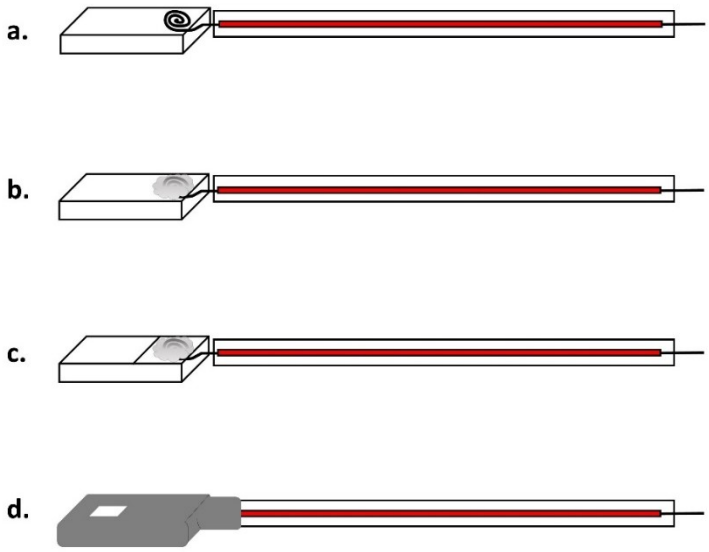


Figure 2.2: Scheme of electrode preparation. A) Cu wire coil placed on an FTO-glass substrate, B) Cu wire/FTO contact area coated with Ag paint, C) Ag painted area coated with clear nail polish and, D) finished (epoxied) electrode.

Experiments were conducted in acidic electrolyte, thus requiring an acid-stable epoxy. Table 2.1 lists the product, brand and acid-stability of trialed epoxies. Stability was assessed using 1.0 M $H_2SO_4$ and $HClO_4$ electrolyte solutions. Loctite EA9460$^{TM}$ was used to seal all electrodes discussed in this report. Electrodes were left to set for at least 12 h following application of epoxy.

Table 2.1: List of epoxies and their stability in 1.0 M acid.

| Epoxy Name | Brand | Acid Stability |
|---|---|---|
| **Double/Bubble® Epoxy (04001)** | Hardman | Not stable |
| **Gorilla Epoxy** | Gorilla Glue | Not stable |
| **Speed Set™ Epoxy** | LePage | Not stable |
| **Loctite EA 9460™** | Henkel | Stable > 24 h |

The epoxy was used to seal off exposed wiring, Ag paint and support edges from electrolyte. It was also used to control the geometric surface area ($A_{geo}$) of the electrode. $A_{geo}$ varied between 0.07-0.16 $cm^2$, with the difference being accounted for by normalizing the measured/applied current by $A_{geo}$.

FTO-glass ("blank") electrodes were used to assess the support's electrochemical stability and activity with respect to OER in 1.0 M $HClO_4$ and 1.0 M $H_2SO_4$. The support material was found to have an initial overpotential ≥ 0.7 V that was unstable over time. The potential typically increased gradually over the first few hours (~2-4 h) of electrolysis and then sharply dropped. The pattern often repeated over the course of 24 h CP experiments (performed at $j = 10\ mA \cdot cm^{-2}$). The instability of the potential trend was likely caused by dissolution of the conductive FTO layer. A brown solid was found to form on the counter electrode (CE), suggesting that dissolution of the support surface exposed the Cu wiring and Ag paint to electrolyte.

## 2.2 Electrochemical Techniques

The electrocatalytic activity of a material is typically assessed using linear sweep voltammetry (LSV), while the electrochemical stability can be probed using CP. LSV experiments measure the current response of a material as the applied potential is linearly increased. CP experiments measure the potential response of a material that is being held at a constant current for a set amount of time.

The activity of an electrocatalytic material can be defined by its η. For anode materials under investigation for OER catalysis, the η can be written as

$$\eta = E_{WE\ vs.\ RE} + E_{RE\ vs.\ RHE} - E^{o}_{H_2O\ vs.\ RHE} \qquad (2.1)$$

where $E_{WE\ vs.\ RE}$ is the working electrode (WE) potential relative to the reference (RE), $E_{RE\ vs.\ RHE}$ is the RE potential relative to the reference hydrogen electrode (RHE) and $E^{o}_{H_2O\ vs.\ RHE}$ is the theoretical minimum potential required to split water. An effective electrocatalyst will have a small η when operated at a specified current density. The oxygen evolution reaction has an $E^{o}$ of 1.23 V and a Ag/AgCl (1 M KCl) electrode was used as the RE used for acidic water oxidation experiments. Thus, the η for an electrocatalyst for the OER can be written as

$$\eta = [E_{WE\ vs.\ RE} + 0.059(\mathrm{pH}) + 0.222\ \mathrm{V}] - [1.23\ \mathrm{V} - 0.059(\mathrm{pH})] \qquad (2.2)$$

The electrochemical stability of a material can be assessed by observing how its potential response evolves over time when a constant current is applied. An electrochemically-stable electrocatalyst will have an unchanging potential for the time over which it is operated. The evolution of an electrocatalyst's activity over time can also

be evaluated through CP, since changes/instability in WE potential correspond to changes/instability in WE η.

The configuration of the electrochemical cells used for the projects detailed in the following chapters are illustrated in Figure 2.3. A conventional three-electrode cell was used for all electrochemical experiments outlined in Ch. 3 (Figure 2.3A). A stir bar was used to minimize diffusion-based contributions from experimental observations. For electrochemical experiments performed on metal boride systems (Ch. 4), a modified pressed-flow cell was used (Figure 2.3B). Electrolyte was continuously circulated through the system by a pump, thereby mitigating diffusion limitations. Electrolyte was saturated with $O_2$ (g) for 30 min prior to experimentation in both cell set-ups.

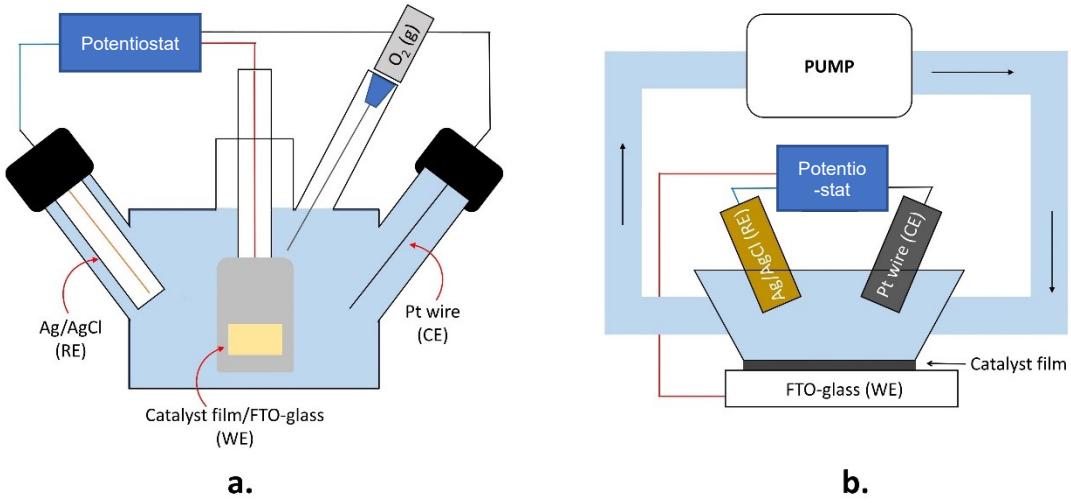


Figure 2.3: Illustrations of A) a conventional and, B) a modified pressed-flow cell used for 3-electrode electrochemical experiments.

The materials investigated in this thesis were electrochemically characterized in acidic media using $HClO_4$ and/or $H_2SO_4$ solutions with concentrations of 0.10 M, 0.50 M and/or 1.0 M. An Ag/AgCl electrode stored in 1.0 M KCl ($E^o$ = 0.2222 V vs. RHE) was

used as the RE for acid-mediated experiments. A Pt wire was used as the CE for all experiments. Electrochemical experiments under basic conditions were performed using an Hg/HgO RE stored in 0.1 M NaOH ($E^o$ = 0.989 V vs. RHE).

### 2.3 Faradaic Efficiency (F.E.)

Faradaic efficiency (F.E.) reflects a system's ability to selectively perform an electrochemical reaction of interest. It is the efficiency by which the material of interest performs a certain electrochemical charge transfer process. F.E. is calculated by comparing the amount of product formed experimentally to the amount predicted theoretically.

A common way of performing F.E. is using an inverted burette set up, as illustrated in Figure 2.4. As shown, the cathode and anode are placed in two separate compartments of an electrochemical cell, with a frit connecting the two chambers. Current is supplied to the system and electrochemical reactions proceed at the surface of both electrodes. In Figure 2.4, the efficiency of the anode material to facilitate OER is measured by collecting the evolved $O_2$ (g). The composition of the evolved gas was further confirmed qualitatively with gas chromatography analysis. The CE facilitates the complimentary HER. The amount of $O_2$ (g) generated in a given timeframe by the anode material is compared to the theoretical amount of $O_2$ (g) generated for 100% current (charge) efficiency toward OER. F.E.s lower than 100% suggest alternative processes are present and consuming some of the current.

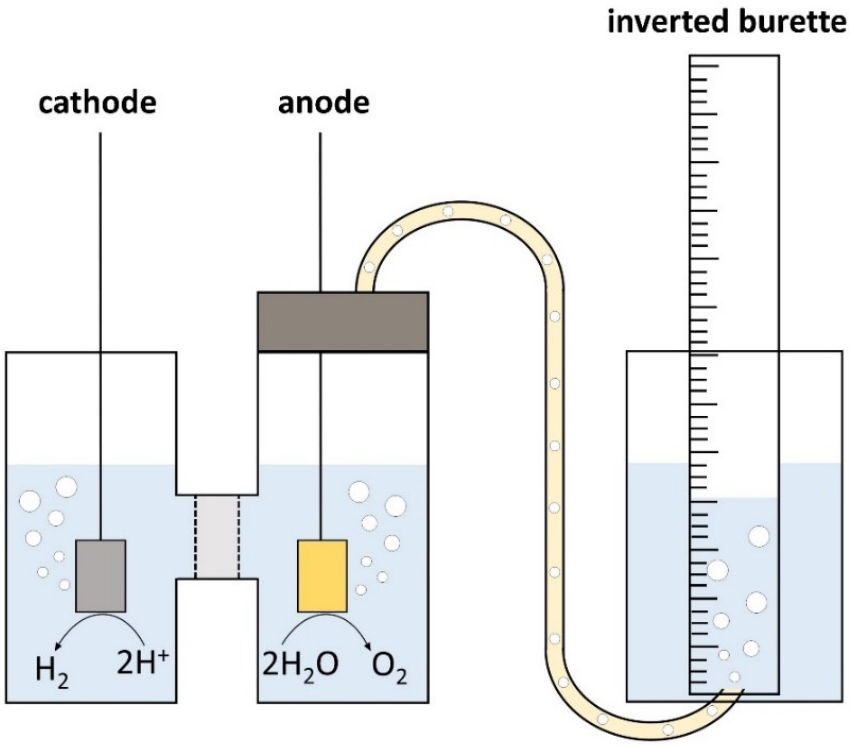


Figure 2.4: Illustration of inverted burette set-up for F.E. measurement. The anode generates $O_2$ (g) and the amount produced is measured as a volume change in the inverted burette.

The F.E. can be written as

$$F.E. = \frac{n_{experimental}}{n_{theoretical}} \times 100\% \qquad \text{(Equation 2.3)}$$

where $n_{\text{experimental}}$ is the measured amount (moles) of product formed and $n_{\text{theoretical}}$ is the theoretical amount (moles) of product formed. The $n_{\text{theoretical}}$ for a system can be determined from the amount of charge (Q), or current, passed for a given time and the number of $e^-$ ($n_{e^-}$) required to produce one equivalent of product,

$$n_{theoretical} = \frac{n_{e^-} \cdot F}{I \cdot t} \qquad (2.4)$$

where F is Faraday's constant (96485 C·mol$^{-1}$), *I* is current and *t* is time. For acid-mediated OER, 4 e$^-$ are consumed to produce one equivalent of $O_2$ ($n_{e^-}$ = 4). Thus, $n_{\text{theoretical}}$ becomes

$$n_{theoretical} = \frac{3.86e^5\ C{\cdot}mol^{-1}}{I \cdot t} \qquad (2.5)$$

In an inverted burette experiment the amount of $O_2$ produced is recorded as a volume change. $n_{\text{experimental}}$ is calculated from the volume change using the molar mass (Mm) and density of the product,

$$n_{experimental} = \frac{(V_{initial} - V_{final}) \cdot d}{Mm} \qquad \text{(Equation 2.6)}$$

$$n_{experimental} = \frac{\Delta V \cdot d}{Mm} \qquad \text{(Equation 2.7)}$$

where V is volume and *d* is density. In the case of $O_2$ evolution, the density of $O_2$ is 1.429 g/mL (at standard pressure and temperature) and the molar mass is 18.015 g·mol$^{-1}$. Thus, $n_{experimental,\ O_2}$ becomes

$$n_{experimental} = \Delta V \cdot 0.08\ mL \cdot mol^{-1} \qquad \text{(Equation 2.8)}$$

F.E. is often plotted as moles of product produced ($n_{experimental}$) and expected ($n_{theoretical}$) over time (Figure 2.5). If the experimental trendline deviates from the

theoretical one, then the F.E. < 100% and the system is losing energy to some parasitic process.

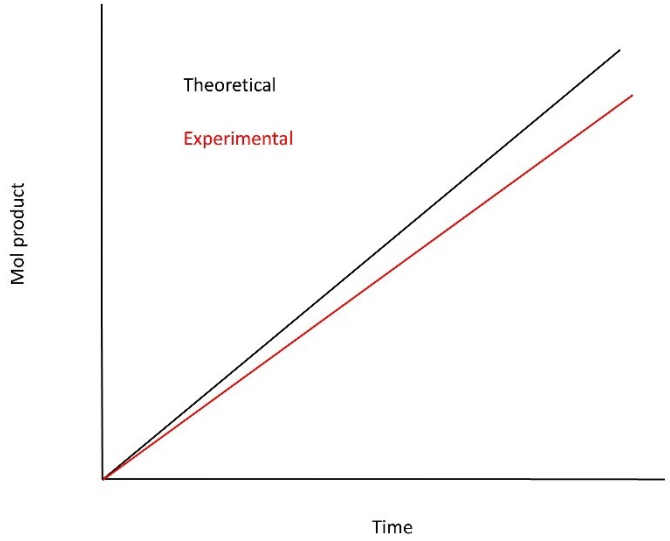


Figure 2.5: Example of a F.E. plot for a material with F.E.< 100%.

The F.E. reported in this thesis were performed using an inverted burette set up with a Pt wire counter electrode and the WE operated at $j = 10\ mA \cdot cm^{-2}$. The F.E.s were recorded for CP experiments performed at $10\ mA \cdot cm^{-2}$ and the collected $O_2$ was analyzed using gas chromatography.

## 2.4 Scanning Electron Microscopy (SEM)

SEM utilizes the particle-wave duality of electrons to generate high-resolution images of material surfaces. SEM images are produced by the inelastic interaction of source $e^-$ with atoms in the material.[104] Figure 2.6A shows a simplified illustration of how SEM images are generated. An $e^-$ gun shoots a beam of $e^-$ at a sample and the ejected $e^-$ are collected by a detector. An SEM image is comprised of the detection of $e^-$ from many

point-like sections of the sample surface, which are compiled/collected by scanning the sample surface in a rectangular grid-like pattern (*raster scan*).[105,106] For a material to be visualized using SEM, the sample must be conductive, or coated with a conductive film to prevent sample charging.

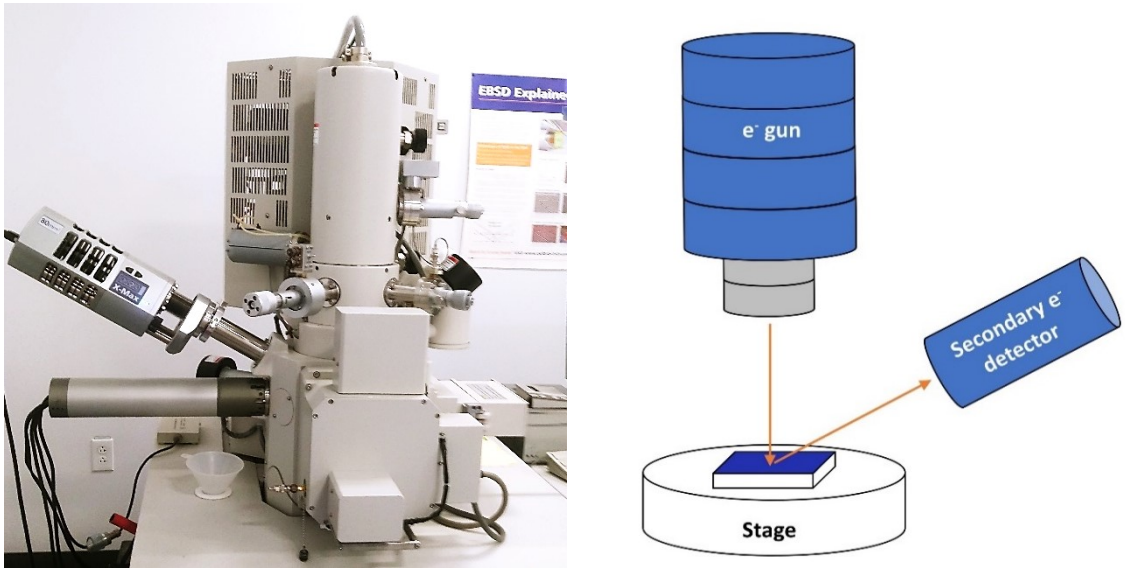


Figure 2.6: A) Image of SEM instrument located at Dalhousie University Sexton campus and, B) illustration of SEM instrumentation.

When $e^-$ from the $e^-$ beam (primary $e^-$) hit the sample one of the resulting interactions/processes involves the displacement of sample $e^-$. Valence $e^-$ ejected from atoms within the sample by the $e^-$ beam are known as secondary $e^-$ (SE, Figure 2.7). SE are outer-shell $e^-$ and those ejected from the sample typically have binding energies < 50 eV.[104,106] For SE to be detected, they must traverse and escape the sample. Those closer to the sample surface have a greater probability to escape, which thereby limits the depth from which SEM signals originate. The maximum signal depth of SEM is approximately 50 nm and can be as low as a tens of angstroms (Figure 2.8).[104,105]

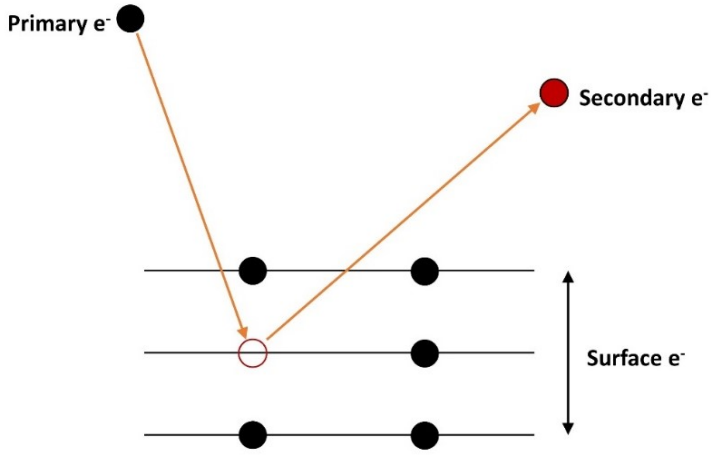


Figure 2.7: Scheme of secondary electron generation in SEM.

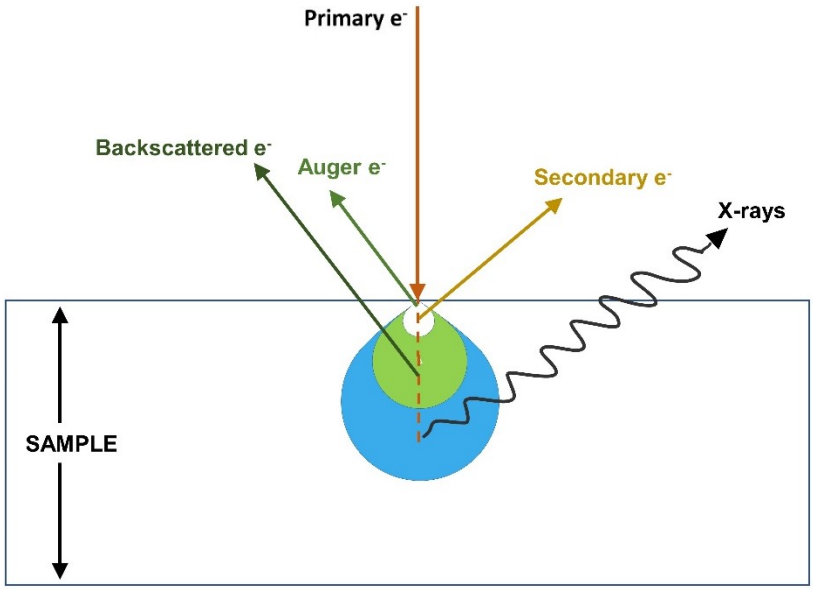


Figure 2.8: Penetration and signal depths for SEM-based characterization techniques.

The small depth of escape for SE allows SEM to be a surface-sensitive technique. The narrow area sampled in each "pixel" of the raster scan leads to nanometer spatial resolution.[107] The extent of spatial resolution is dependent on the width of the $e^-$ beam, with the escape width being only slightly larger than that of the incident beam.[104] The surface-sensitivity and spatial resolution of SEM produces images that afford a detailed

understanding of sample surface morphology and topography. SEM uses accelerating voltages between 0.5-30 kV, with larger voltages having a greater penetration depth and thus reduced resolution/surface-sensitivity.[105,106] Samples can also become altered at high voltages or experience significant build-up of charge at the surface, which further affects image resolution. Furthermore, the composition of the sample affects the resolution/sensitivity attainable as the penetration depth of the $e^-$ beam increases with the atomic mass of the elements.[105,106]

For the projects included in this thesis, a Hitachi S-4700 Field Emission Gun SEM was used in SE mode. A mono-crystalline tungsten (W) metal probe tip generates an $e^-$ beam via the application of an electric field at the tip, which enables $e^-$ to tunnel between the probe and sample. The tunneling $e^-$ are accelerated from the tip by a user-defined accelerating voltage. Samples were sputter-coated with a 12 nm film of gold/palladium (Au/Pd) to prevent surface charging during the imaging process.

## 2.5 X-ray Diffraction (XRD)

### *2.6.1 X-ray diffraction theory and conventional analysis*

X-ray diffraction (XRD) derives structural information for a material through the elastic scattering of incident X-rays by atoms within the sample.[104] The spacing of atoms within a material allows them to act as natural diffraction gradients for X-rays. This leads to constructive and destructive interference of the scattered light waves, which produces a structure-dependent diffraction pattern. The diffraction pattern can be defined by applying Bragg's law to the crystal planes of a material's 3-D structure,

$$(h, k, l)\lambda = 2d \sin 2\theta \qquad (2.9),$$

where ($h$, $k$, $l$) are Miller indices of a given reflection plane, $\lambda$ is the incident X-ray wavelength, d is the distance between atoms in a given plane and $2\theta$ is the angle between the incident X-ray path and the scattered X-ray path (Figure 2.9). The Miller indices represent the integer values associated with the positioning of crystal planes within the 3D crystal cell.

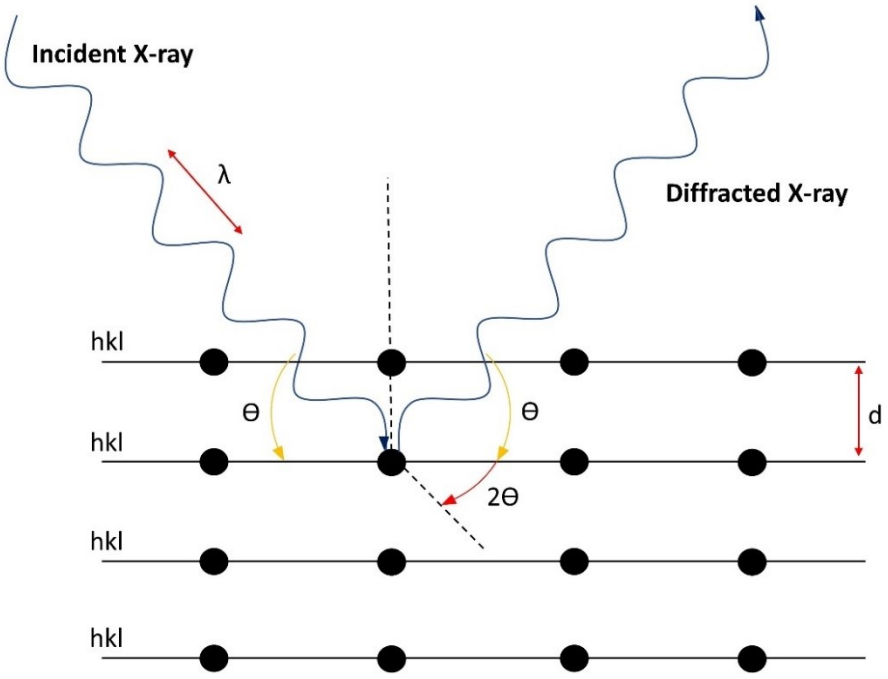


Figure 2.9: XRD by atoms in a crystal as predicted by Bragg's law.

The distance between covalently bound atoms is $d \sim 0.1$ nm, thus the wavelength of the radiation used for diffraction must be on the same scale as $d$. In many instruments, the photon(s) emitted from the copper (Cu) L- to K-shell transition is used as the X-ray source. A focused beam of high energy $e^-$ strikes a metal (e.g., Cu) target and bumps a core $e^-$ off an atom (Figure 2.10A). This leaves a vacancy in the inner shell of the atom,

which is filled by an outer $e^-$ (Figure 2.10B). This electronic transition from a high energy orbital to a low energy orbital causes a high energy photon (X-ray) to be emitted. The emitted X-radiation is used for XRD.

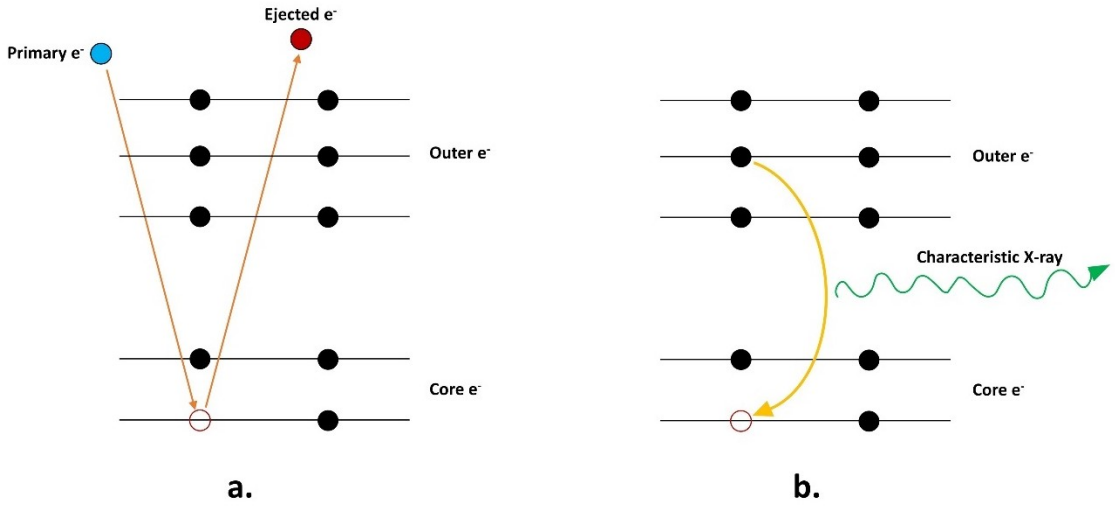


Figure 2.10: A) An $e^-$ collides with and ejects a core $e^-$ from an atom in the sample and, B) an outer $e^-$ fills the inner-orbital vacancy, resulting in emission of a characteristic X-ray.

Multiple photons are emitted by this type of transition, as shown in Figure 2.11. A filter can be placed in the path of the X-rays before reaching the sample to remove the $K_\beta$ radiation and reduce the amount of signal splitting seen in a pattern. Alternatively, a monochromator can be placed before the detector to remove scattered $K_{\alpha 2}$, $K_\beta$ and Bremsstralung x-rays. A general XRD set-up is shown in Figure 2.12. The slits are used to focus the x-rays and minimize environmental.

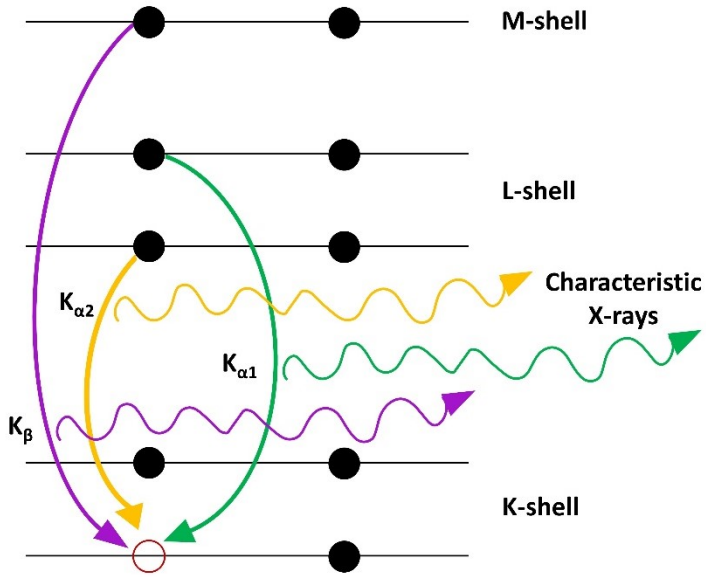


Figure 2.11: Generation of Cu $K_{\alpha 1}$, $K_{\alpha 2}$ and $K_{\beta}$ characteristic X-rays.

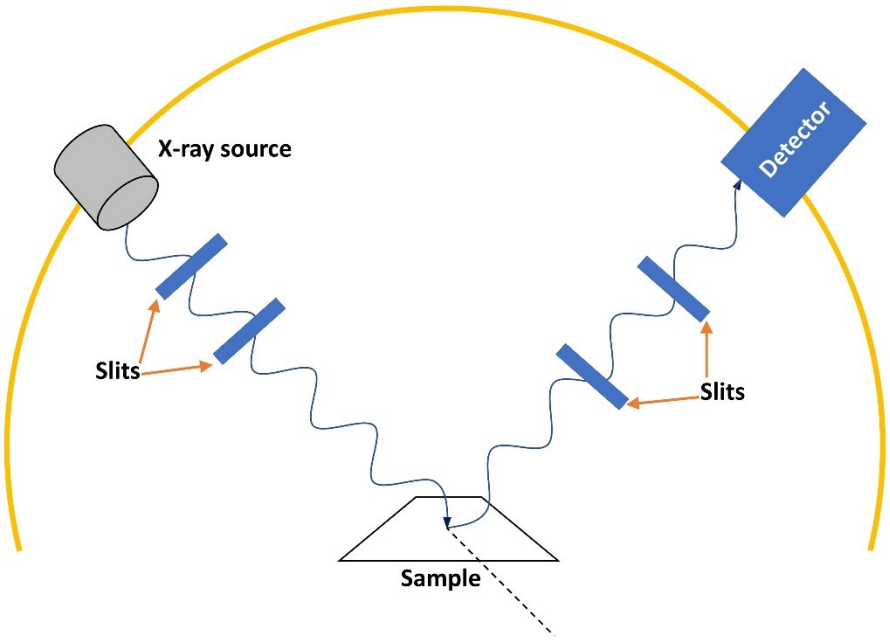


Figure 2.12: General XRD scheme. The detector moves along a circular path to scan the desired 2Θ range.

*2.6.2 Grazing-incidence angle X-ray diffraction*

Grazing-incidence angle XRD (g-XRD) is a modified XRD technique which enables the selective detection of surface diffraction patterns. Conventional XRD (Section 2.6.1) is not a surface-sensitive technique as it uses a high incident angle to irradiate a sample, thereby allowing photons to penetrate the bulk of a sample. In contrast, g-XRD uses a shallow incident angle, typically near that required for total internal reflection, to decrease the sampling depth of the incident photons.[108] Figure 2.13 shows the schematic of a g-XRD set-up, where the x-ray source is held at a smaller angle relative to the surface than that shown in Figure 2.12. The detector still moves along a fixed circular path, however the 2Θ range will be covered at lower heights relative to those in a conventional XRD.

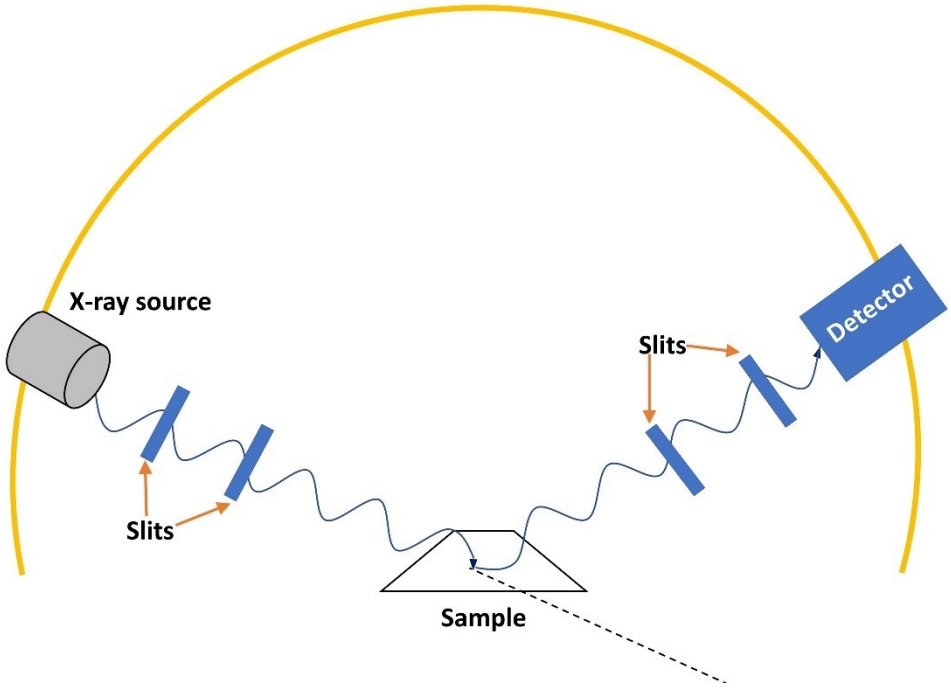


Figure 2.13: Grazing angle XRD scheme for surface-sensitive analysis.

g-XRD increases the contributions of surface-origin X-ray signals. By decreasing the incident angle height, the depth of the atoms contributing to the detected signals also decreases. This in turn limits the atoms that contribute to the measured signal to those near the surface. Since the signal is now primarily composed of X-rays diffracted by surface atoms, the resulting diffraction pattern will have amplified surface peak intensities compared to that of a conventional XRD pattern.[109]

g-XRD experiments were performed on the $IrO_x$ films discussed in Ch. 3 of this thesis. Both conventional and g-XRD data was collected using a Siemens D5000 diffractometer with Cu $K_{\alpha 1}$ radiation ($\lambda$ = 1.5418 Å) and scintillation counter detector. g-XRD data was acquired using an accelerating voltage of 45 kV, current of 40 mA, fixed incident angle of 4°, step width of 0.05 and 3 counts/s dwell time. Conventional-XRD patterns were generated using an accelerating voltage of 30 kV, current of 35 mA, step width of 0.05 and 3 counts/s dwell time.

## 2.6 X-ray Photoelectron Spectroscopy (XPS)

XPS is a characterization technique that provides both structural and compositional information using the binding energies of $e^-$ ejected from a sample. The X-rays used to generate an XPS spectrum are produced in a comparable manner to that outlined in Section 2.6 (Figure 2.11), however lower-energy X-rays are used for XPS.

An X-ray gun is used to bombard a sample with X-rays, which collide with atoms in the specimen and eject tightly-bound core $e^-$ (Figure 2.14). The ejected $e^-$ are collected

by an energy analyzer that sorts the $e^-$ based on their energies before they are quantified by a detector.

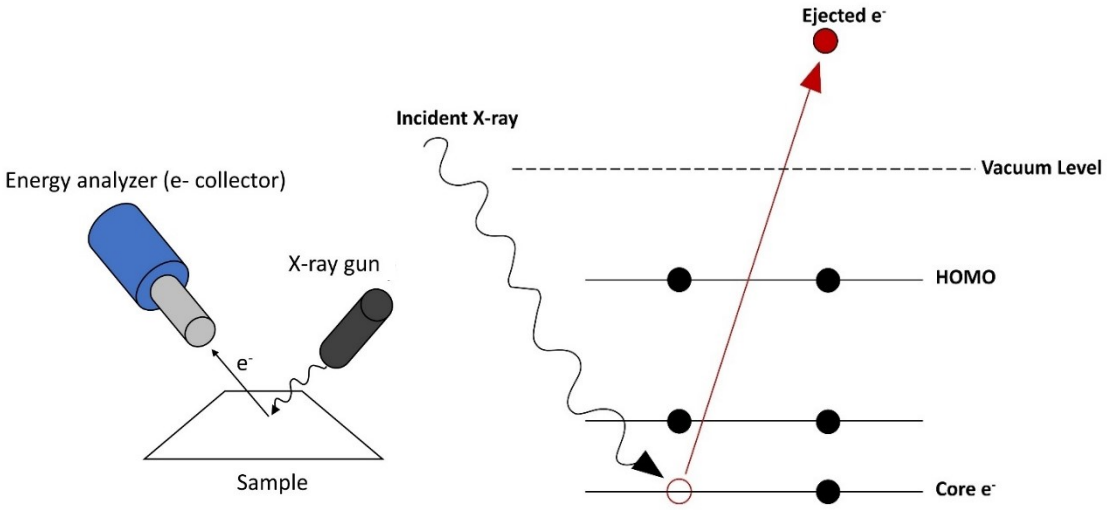


Figure 2.14: Scheme of A) XPS set-up and B) photoelectron generation process for XPS measurement.

An incident X-ray with energy $h\nu$ is used to eject an $e^-$ from the inner shell of an atom (Figure 2.14B). The ejected $e^-$ has a binding energy (B.E) related to the atom and orbital from which it originated. The ejected $e^-$ must have enough energy transferred to it such that it is able to escape the sample and become a free $e^-$. This escape energy requirement can be represented using the material work function, $\Phi_m$. The $\Phi_m$ is defined as the energy required for an $e^-$ to be removed from a material into a vacuum.

The $e^-$ that escape from the sample have a kinetic energy associated with them, which can be written as

$$E_k = h\nu - (B.E + \Phi_m) - \Phi_a \qquad (2.10)$$

where $E_k$ is the kinetic energy of the ejected $e^-$ and $\Phi_a$ is the work function of the energy analyzer system.[104] The energy analyzer measures and sorts incoming $e^-$ based on their

$E_k$. The measured $E_k$ values and work functions can then be used to determine the B.E of the $e^-$ in the sample,

$$B.E = h\nu - (\Phi_m + \Phi_a) - E_k \qquad (2.11)$$

XPS spectra are generated by quantifying the number of $e^-$ with a particular B.E sorted by the energy analyzer system. Each element has a unique region of B.E.s associated with it. The oxidation state and/or positioning of an atom within a material determines the positioning of the electron $e^-$ within this characteristic B.E region.[104]

XPS is a surface-sensitive technique since $e^-$ must travel out of a sample to vacuum level in order to be detected.[104] $e^-$ that are not near the surface of the sample must travel further through the sample to escape, thus there is more opportunity for energy loss through scattering interactions. The probability of escape for an $e^-$ can therefore be written in terms of distance from the surface,[104]

$$P(d_n) = e^{-(d/IMFP)} \qquad (2.12)$$

where $P(d_n)$ is the probability of an $e^-$ escaping the sample as a function of distance, d is the distance of the $e^-$ from the surface and IMFP is the inelastic mean free path for a material. The IMFP represents the average distance an $e^-$ travels before it is scattered inelastically within a material. As the distance increases the probability of escape decreases. Nearly all the $e^-$ that reach the energy analyzer are from within 3λ of the surface, with most coming from within 1(IMFP).[104]

XPS characterization was performed on $IrO_x$ and $TiB_2$ samples in Ch. 3 and 4, respectively. The data was collected using a Kratos Axis Ultra system with a pressure of

$1x10^{-9}$ Torr and a monochromatic Al $K_\alpha$ x-ray source ($\lambda$=1486.6 eV). The ejected $e^-$ were collected at $0^\circ$ with respect to the surface normal using a retarding pass energy of 160 eV for the survey XPS scans, 20 eV for high-resolution (HR) core level scans. CasaXP software (VAMAS) was used to interpret and fit HR XP spectra.

## 2.8 Inductively coupled plasma- optical emission spectroscopy (ICP-OES)

### *2.8.1 Plasma generation*

ICP is used as a means of vaporization, ionization and excitation of liquid or gas analytes. Solid materials must be dispersed in solution or acid-digested prior to plasma treatment.[110] The plasma is generated using a plasma torch, which circulates argon gas (Ar) through a double-walled tube (Figure 2.15A).[111] Seed $e^-$ are used to spark the formation of ionized ($Ar^+$), while the resulting free $e^-$ and continuous flow of Ar sustain the plasma thereafter (Figure 2.15B and C). A radiofrequency (RF) coil located at the opening of the torch applies an alternating RF field to the plasma, which accelerates the free electrons and spurs the formation of more $Ar^+$.[111] This induction of high-energy $e^-$-atom collisions via the applied RF field is responsible for the technique nomenclature.[110] The plasma takes on a laminar shape as the ionized species oscillate with the applied magnetic and electric fields.[110] The oscillations of charged species composing the plasma result in an internal temperature that can reach up to 10,000 K.[111]

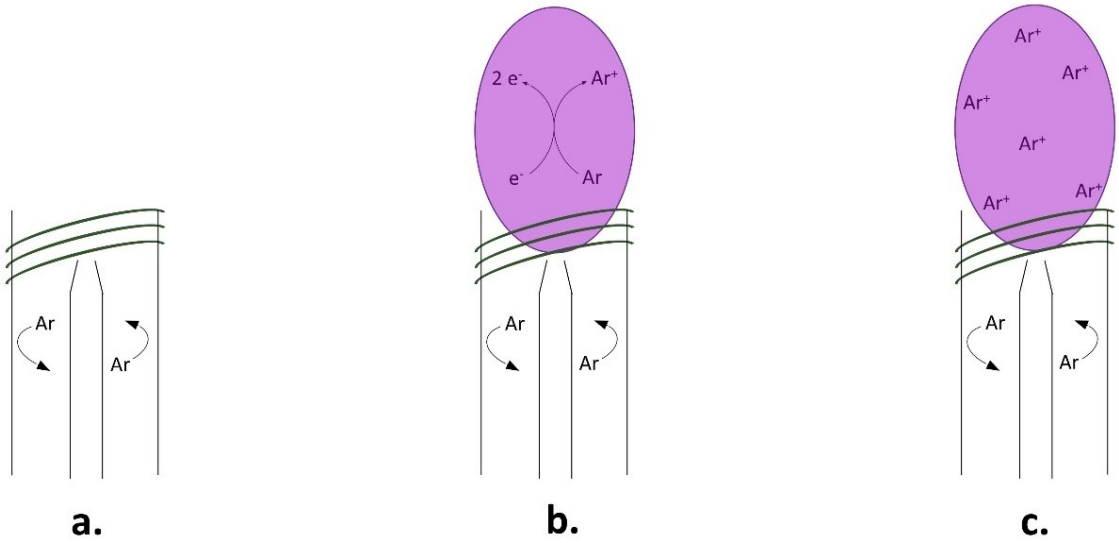


Figure 2.15: Step wise sequence of plasma formation in/for a plasma torch. A) Ar is circulated around the torch chamber, B) seed $e^-$ initiate plasma formation and, C) plasma is sustained via the continual formation of $Ar^+$ (and $e^-$). The RF coil (field) maintains the shape, temperature and formation of the plasma.

Once the plasma is formed, analyte is sent through the inner tube of the plasma torch using a carrier gas (usually Ar; Figure 2.16A). Liquid-based samples must be transformed into an aerosol in order to be carried into the plasma chamber. De-solvation, or the removal of remnant solvent, occurs immediately upon sample entry into the plasma plume.[111] The sample then fragments into smaller and smaller pieces until individual molecules/complexes are formed, thereby transforming the sample into a vapour. The vapourized sample undergoes further fragmentation to form individual atoms, which are then ionized and/or excited (Figure 2.16B and C).[111] Either the ionized elements or the excited state(s) emissions can be utilized to characterize the sample composition depending on the technology coupled to the ICP torch.

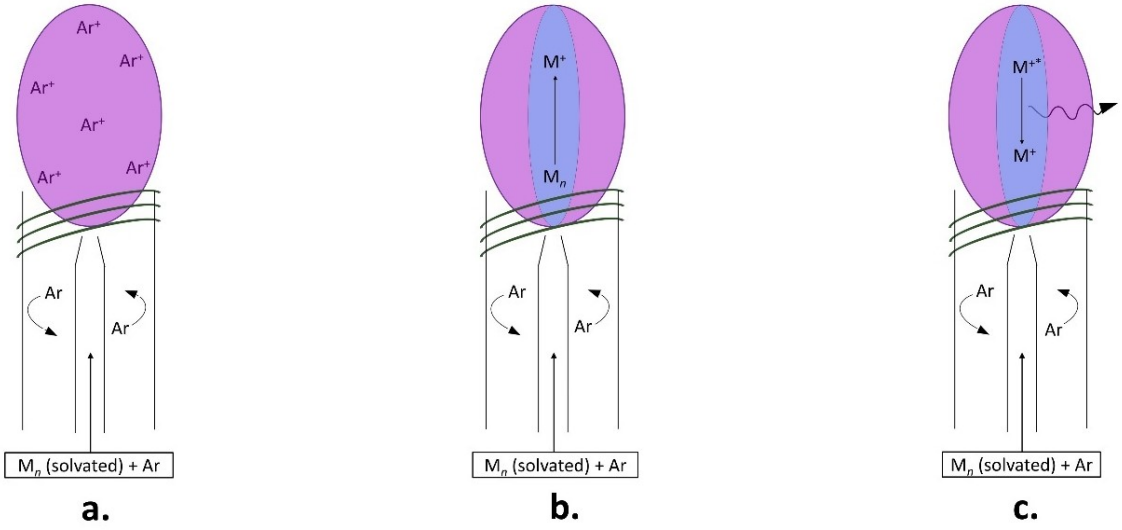


Figure 2.16: Sequence of ICP sample A) introduction, B) excitation and, C) emission from an excited ionized species.

*2.8.2 Inductively coupled plasma- optical emission spectroscopy (ICP-OES)*

ICP-OES allows for the investigation of sample elemental composition through generation of emission spectra from constituent atoms and ions excited within a plasma. Samples are introduced into an ICP torch where they are broken down into their constituent atoms (or ions). The atoms (ions) become excited and emit photons as they return to their ground state (Figure 2.17A). A spectrometer placed perpendicular to the ICP torch collects the photons with focusing optics (Figure 2.17B). Focused emissions then travel through a mono- or polychromator and reach the detector, which processes the signal and generates an emission spectrum (Figure 2.17C, D). Spectral lines characteristic to the elements can then be used to identify which are present and elemental standards can be used to quantify the amounts.

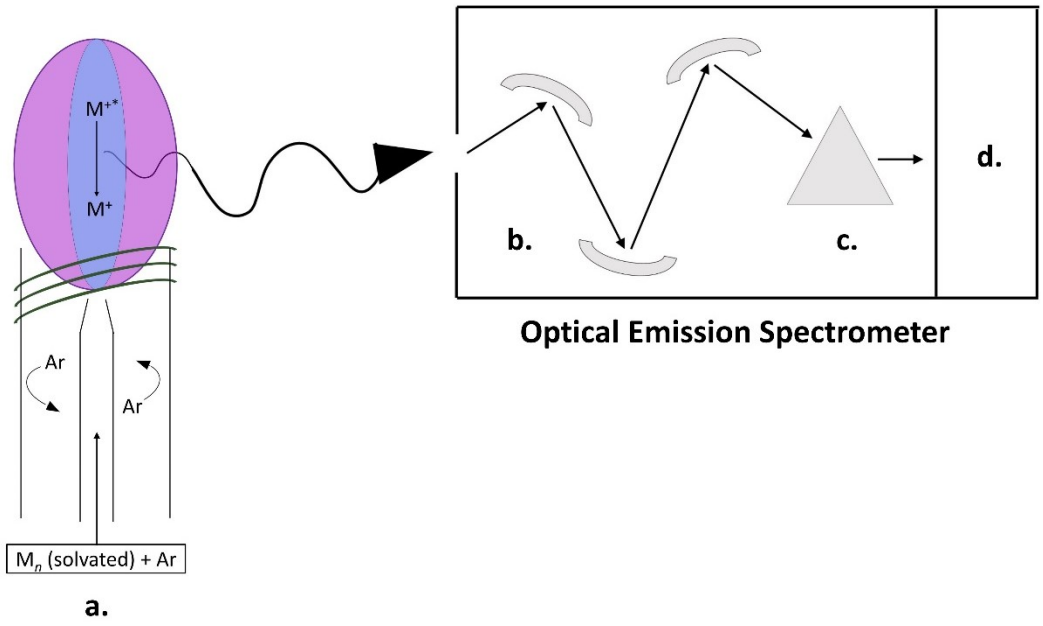


Figure 2.17: Set-up of an ICP-OES system: A) ICP-torch, B) focusing optics, C) mono/polychromator and, D) detector.

ICP-OES is a destructive characterization technique in that the analyzed material is destroyed in the process of characterization. However, the technique requires relatively little sample compared to characterization techniques like XPS and XRD. If an ICP-OES is equipped with a polychromator, then the emission spectrum for a sample can be generated ~ instantaneously because the emission times of elements are comparable.[111]

ICP-OES was performed for $IrO_x$ and $TiB_2$-electrolysis electrolyte solutions discussed in Ch. 3 and 4, respectively, of this thesis using a PerkinElmer Optima 8000 instrument.

## 2.9 Sputter Deposition

Sputter deposition is a high-energy technique used to coat substrates with a smooth, compact film of material. A plasma, often composed of Ar, is used to knock material off the target and onto the substrate(s). The plasma is initially formed by high-energy collisions between accelerated $e^-$ and Ar atoms (Figure 2.18A).[104] The plasma sustains itself through chain-reactions between Ar atoms and $e^-$ knocked off $Ar^+$ atoms.[104] The target is surrounded by a negative environment, which attracts $Ar^+$ to its surface (Figure 2.18B). The ensuing collisions eject atoms off the target and onto the substrate (Figure 2.18C). As time proceeds, the substrate continues to be coated by scattered target atoms (Figure 2.18D).

The thickness of a film formed through sputter deposition is time-dependent.[112] By increasing the sputtering time, the coating thickness will also increase. The relationship between sputtering time and film thickness depends on many conditions including the power, target, and sputtering mode used. The positioning of the substrate relative to the substrate affects the uniformity of the deposited film. Substrates placed across from the target typically have more consistent film thickness.[112] Rotation of the substrate holder during the deposition process also results in more uniform film formation across the surface of a substrate.[112] As illustrated in Figure 2.19, sputter-deposition tends to be inefficient in terms of target material consumption versus substrate coating so it is considered to be a wasteful technique.

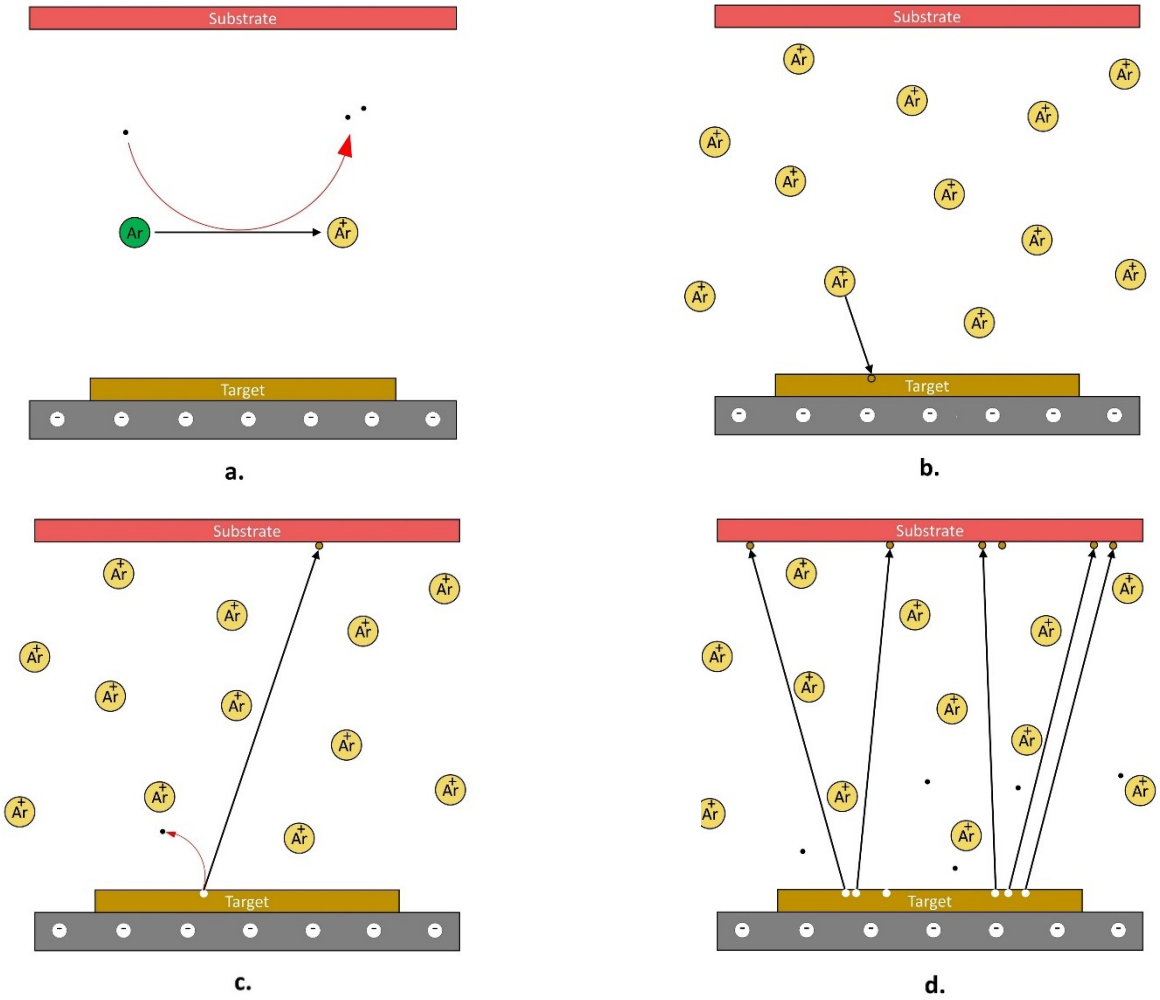


Figure 2.18: Sputtering process: A) initiation of plasma formation, B) collision of plasma ion with target, C) ejection of particles from target surface and, D) growth of sputter-coating on substrate surface.

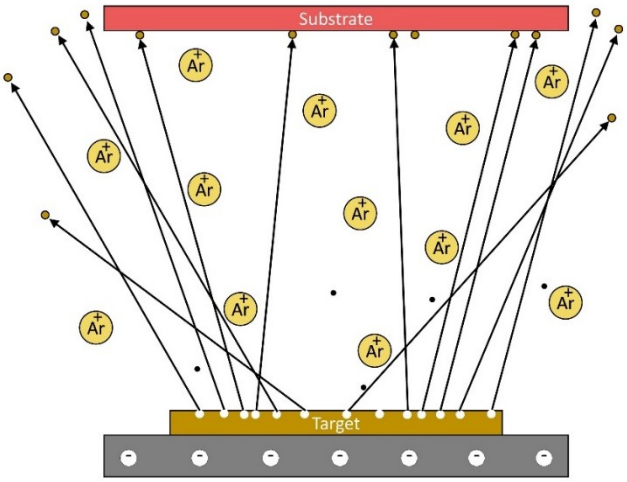


Figure 2.19: Illustration of sputter deposition process showing ejected target atom trajectories.

A sputter coating was performed to all SEM and EDS samples detailed in this thesis using a Leica ACE200 Sputter Coating System in diffuse mode. Substrates were coated with a 12 nm film of Au/Pd under Ar atmosphere. Combinatorial sputtering was used to form SIROF films (~300 nm) on FTO-glass and Si substrates at at 2.6 sccm $Ar/O_2$ (4.89 mT), 480W · min (30 W) for ~ 20 min. Sputtered films of $TiB_2$ were prepared from a $TiB_2$ target and deposited onto FTO-glass substrates at 1.7 sccm Ar (1.97 mT), 1470 and 3920 $W \cdot min^{-1}$ (40 W) for 37 and 98 min, respectively. Samples were sputtered using a Corona Vacuum Coater V3T Sputter instrument.

# CHAPTER 3. PREPARATION OF IRIDIUM OXIDE FILMS USING DIFFERENT FABRICATION TECHNIQUES AND INVESTIGATION OF THEIR PROPERTIES IN DIFFERENT ACIDIC ENVIRONMENTS[1,2]

## 3.1 Introduction

$IrO_x$ is the only material system that has been shown to possess the necessary mix of activity, stability and selectivity for acid mediated OER.[41,47,61,113] The scarcity and expense of Ir metal prevents $IrO_x$ from being a long-term, cost-effective anode material. However, we still need to rely on Ir due to the lack of other materials with acceptable OER performances. $IrO_x$ also serves as a model system for studying the performance characteristics of OER materials in acidic media.

$IrO_x$ is a family of materials and exists in many forms. As a result, there is substantial variation in the literature in terms of the systems being used for benchmarking purposes.[41,96,99,114–118] Countless parameters contribute to the observed physical characteristics and electrochemical performance of $IrO_x$ materials. The method in which a film is fabricated largely determines the type of $IrO_x$ formed.[49,56,57,60,62,91] The support substrate can have large implications on the performance and longevity of the deposited film.[37,51,61,119–121] The range of current densities used to evaluate material activity and the

[1] ICP and F.E. experiments were performed by M. Richter. SEM, XRD and electrochemical experiments were performed by M. J. Kirshenbaum.

[2] The in-situ TD films reported in this chapter are referred to as TDPS films to differentiate them from alternative means in-situ TD film production, such as the Pechini synthesis method.

electrolyte conditions also influence the observed material properties.[49,51,74,80,87] Table 3.1 lists some of the experimental conditions reported in the literature for $IrO_x$ studies. Difference in key experimental parameters makes it difficult to draw comparisons between films fabricated in a similar manner, let alone between film type.

Table 3.1: $IrO_x$ film fabrication and electrochemical conditions reported in the literature.

| **$IrO_x$ (support)** | **$\eta_{@j}$ ($mV_{@mA \cdot cm^{-2}}$)** | **Tafel slope (mV/dec)** | **Electrolyte** | **Deposition** | **Stability*** |
|---|---|---|---|---|---|
| $IrO_x$ (Si)[41] | $340_{@10}$ | - | 1.0 M $H_2SO_4$ | T-SIROF | CP (24 h) |
| $IrO_x/SrIrO_3$[45] | $270_{@10}$ | | 0.5 M $H_2SO_4$ | PLD/etching | CP (30 h) XPS (30 min) |
| $IrO_2$[96] | $290_{@10}$ | - | 0.5 M $H_2SO_4$ | Pelletization | - |
| $IrO_x$ [74] (carbon paper) | - | 39 (low) 116 (high) | Nafion (PEM) | SIROF (500 nm) | CV CP (24 h) |
| $IrO_x$ (Ti)[87] | $45_{@0.1}$ | 58 | 1.0 M $H_2SO_4$ | in-situ TD (450 °C) | - |
| $IrO_x$ (Ti)[87] | $54_{@0.1}$ | 57 | 0.5 M $H_2SO_4$ | in-situ TD (450 °C) | - |
| $IrO_x$ (Ti)[87] | $84_{@0.1}$ | 60 | 0.1 M $H_2SO_4$ | in-situ TD (450 °C) | - |
| $IrO_x$ (Si)[57] | - | | 1.0 M $HClO_4$ | T-Ir (SP) | - |
| $IrO_x$ (Si)[57] | - | 40 | 1.0 M $HClO_4$ | ex-situ TD (500 °C) | - |
| $IrO_2$/CNT (GC)[122] | $250_{@10}$ | 60 | 0.1 M $H_2SO_4$ | DC (80-120 °C) | CP (3 h) CV |
| Ir[49] | $280_{@10}$ # | 60 | 0.5 M $H_2SO_4$ | Ir (wire) | CA (5h) CV |
| $IrO_x$ (Ir)[49] | $100_{@10}$ # | 40 | 0.5 M $H_2SO_4$ | AIROF (- SQW) | CA (5h) CV |
| $IrO_x$ (Ir)[49] | $260_{@10}$ # | 60 | 0.5 M $H_2SO_4$ | T-AIROF (400 °C) | CA (5h) CV |
| $IrO_x$ (Si)[62] | $330_{@5}$ # | - | 0.1 M $H_2SO_4$ | AIROF (300 SQW) | CV, ICP |
| $IrO_x$ (Si)[62] | $400\text{-}440_{@5}$ # | - | 0.1 M $H_2SO_4$ | T-AIROF (100-600 °C) | CV, ICP |

| $IrO_x$ (support) | $\eta_{@j}$ ($mV_{@mA\cdot cm^{-2}}$) | Tafel slope (mV/dec) | Electrolyte | Deposition | Stability* |
|---|---|---|---|---|---|
| Ir (Si)[62] | $440_{@5}$ # | - | 0.1 M $H_2SO_4$ | Ir (EBPVD) | CV, ICP |
| $IrO_x$ (Si) | $400\text{-}490_{@5}$ # | - | 0.1 M $H_2SO_4$ | T-Ir (100-600 °C) | CV, ICP |
| N- $IrO_2$/C-Pt[115] | $610_{@10}$ # ($470_{@5}$) # | 120 | 0.1 M $HClO_4$ | DC | - |
| N- Ir/C-Pt[115] | $620_{@5}$ # | 150 | 0.1 M $HClO_4$ | DC | - |
| Ir[50] | $320_{@0.1}$ # $330_{@0.2}$ # $340_{@0.5,\ 1}$ # | 66 | 0.1 M $H_2SO_4$ | Ir (disk) | SFC-ICP, CV |
| $rO_x$ (Ir)[50] | $320_{@1}$ # $350_{@5}$ # | 40 | 0.1 M $H_2SO_4$ | AIROF (500 CV) | SFC-ICP, CV |
| $IrO_2$ (CP)[99] | $480_{@10}$ | 66 | 1.0 M $H_2SO_4$ | CPE (30% $IrO_2$) | CP (30 min) |
| Ir[47] | $430_{@5}$ # | - | 0.1 M $H_2SO_4$ | Ir (SP, PVD) | SFC-ICP |
| $IrO_2$[47] | $540_{@5}$ # | - | 0.1 M $H_2SO_4$ | T-Ir (600 °C) | SFC-ICP |
| $IrO_2/TiO_2$/(Ti)[51] | $330_{@100}$ | 30 (low) 60 (high) | 1.0 M $H_2SO_4$ | in-situ TD (550 °C) | CP (3 h) |
| $IrO_x$ (Ti)[37] | $325\text{-}415_{@0.5}$ # | 40-72 | 0.1 M $HClO_4$ | in-situ TD (250-550 °C) | - |
| $IrO_x$[44] (Ta, quartz) | $300_{@20}$ # | - | 0.5 M $H_2SO4$ | SIROF | CA (18 h) |
| $IrO_x$[117] (FTO-glass) | $600_{@10}$ $540_{@10}$ $520_{@10}$ | 136 130 111 | 1.0 M $H_2SO_4$ | T-SIROF (300 °C) | - |
| $IrO_x$[60] (FTO-glass) | $270\text{-}320_{@1}$ # | - | 1.0 M $H_2SO_4$ | SIROF | CA (12 h) |
| $IrO_x$[60] (FTO-glass) | $250_{@1}$ # | - | 1.0 M $H_2SO_4$ | T-SIROF (400 °C) | - |
| $IrO_x$[60] (FTO-glass) | $320_{@1}$ # | - | 1.0 M $H_2SO_4$ | ED (300 $\mu A/cm^2$) | - |
| $IrO_x$[60] (FTO-glass) | $370_{@1}$ # | - | 1.0 M $H_2SO_4$ | T-ED (400 °C) | - |
| $IrO_x$[60] (FTO-glass) | $390_{@1}$ # | - | 1.0 M $H_2SO_4$ | ED (2.5 C) | - |
| $IrO_x$[60] | $270_{@1}$ # | - | 1.0 M $H_2SO_4$ | in-situ TD (400 °C) | - |
| $IrO_x$[123] | $470_{@3}$ # | - | 0.5 M $H_2SO_4$ | ex-situ TD (400 °C) | - |

| $IrO_x$ (support) | $\eta_{@j}$ ($mV_{@mA\cdot cm^{-2}}$) | Tafel slope (mV/dec) | Electrolyte | Deposition | Stability* |
|---|---|---|---|---|---|
| $IrO_x$ (Ti)[53] | 470-490$_{@100}$ # | 58-62 | 0.5 M $H_2SO_4$ | in-situ TD (400-600 ° C) | CP |
| $IrO_x$ (Ti)[53] | 430-470$_{@100}$ # | 59-64 | 0.5 M $H_2SO_4$ | in-situ TD (400-600 ° C) | CP |
| $IrO_x$ (Ti)[53] | 500-480$_{@100}$ # | 61-67 | 0.5 M $H_2SO_4$ | in-situ TD (400-600 ° C) | CP |
| N- $IrO_2$ (GC)[124] | 317$_{@10}$ | 57 | 0.5 M $H_2SO_4$ | DC | CP (3 h) CV ICP |
| $IrO_x$ (GC)[77] | 440$_{@10}$ # | - | 0.1 M $H_2SO_4$ | ED | - |
| $IrO_x$ (Au)[78] | 200$_{@1.5}$ # | 40 | 0.1 M $H_2SO_4$ | ED (CA) | - |
| Ir (Si)[56] | - | 120 | 1.0 M $H_2SO_4$ | Ir (SP) | - |
| $IrO_x$ (Si)[56] | 288$_{@3}$ # | 40 (low) 120 (high) | 1.0 M $H_2SO_4$ | AIROF (350 CV) | - |
| $IrO_x$ (Si)[56] | 255$_{@3}$ # | 40 | 1.0 M $HClO_4$ | in-situ TD (500 °C) | - |
| N- $IrO_2$ (GC)[83] | 282-300$_{@10}$ | 62-67 | 0.5 M $H_2SO_4$ | DC | ALT |
| N- $IrO_2$ (GC)[83] | 312$_{@10}$ | 68 | 0.5 M $H_2SO_4$ | DC | ALT |
| $IrO_2$ (GC)[83] | 312$_{@10}$ | - | 0.5 M $H_2SO_4$ | DC | ALT |
| N- $IrO_x$-Ir[116] (GC) | 310$_{@10}$ # | 44 | 0.5 M $H_2SO_4$ | DC | CA (100 h) |
| Ir (GC)[116] | 350$_{@10}$ # | 44 | 0.5 M $H_2SO_4$ | DC | CA (100 h) |
| $IrO_2$/rGO[84] (GC) | 350$_{@1}$ # | - | 0.5 M $H_2SO_4$ | DC | ALT |
| $IrO_2$ (GC)[84] | 380$_{@1}$ # | - | 0.5 M $H_2SO_4$ | DC | ALT |
| $IrO_2$-$Ta_2O_5$[88] /(Ti) | 170-210$_{@10}$ # | - | 1.0 M $H_2SO_4$ | in-situ TD (500 °C) | ALT |
| 3-DOM $IrO_2$[85] (GC) | 220-240$_{@0.5}$ | - | 0.5 M $H_2SO_4$ | DC | CA (200 min) |
| $IrO_2$ (GC)[85] | 250-270$_{@0.5}$ | - | 0.5 M $H_2SO_4$ | DC | CA (200 min) |
| r-$IrO_2$[118] | 440$_{@10}$ # | - | 0.1 M $HClO_4$ | DC | - |

| $IrO_x$ (support) | $\eta_{@j}$ ($mV_{@mA \cdot cm^{-2}}$) | Tafel slope (mV/dec) | Electrolyte | Deposition | Stability* |
|---|---|---|---|---|---|
| NP-$IrO_x$[81] | 270-330$_{@10}$# | 40-45 | 0.1 M $HClO_4$ | ex-situ TD (150-600°C) | CV |
| $IrO_x$ ($SiO_2$)[55] | 490$_{@150}$# | 48 (low) 130 (high) | 0.5 M $H_2SO_4$ | SIROF | CP (18 h) |

#$\eta_{@j}$ extracted from LSV, CP or CA data (not explicitly stated by authors).

*CP/CA (time) = characterization of catalyst η at $j \geq 10$ mAcm$^{-2}$/E > 1.4 V vs. RHE (OER time); CV = CV stability characterization; ICP = characterization of catalyst chemical stability using ICP-MS or OES; XPS (time) = catalyst composition comparison pre/post OER (OER time).

**SP = sputter, SQW = square wave cycle, EBPVD = electron beam PVD, SFC = scanning flow cell, CP = carbon paste, CPE = carbon paste electrode (w/w% catalyst loading, N-IrOx = nanostructured-IrOx, ALT = accelerated life time test, 3-DOM = 3-dimensional ordered microporous, r-$IrO_2$ = rutile-$IrO_2$.

The current literature requires researchers to try and draw comparisons between various film systems evaluated under a range of operational conditions. However, the validity of such comparisons is questionable because even films of the same family exhibit different electrochemical properties when prepared or operated under different conditions.[37,49,91,125] McCrory et al.[41] proposed a set of benchmark conditions for screening the electrochemical properties of water-splitting materials. The conditions include the use of 1.0 M electrolyte solutions and reporting activities at $j$ = 10 mA $\cdot$ cm$^{-2}$. These are standard conditions for SHC technology operated under 1 sun illumination.[43,126] However, as is evident from Table 3.1, few studies have characterized $IrO_x$ systems in the outlined molarity and $j$ regime. The OER characteristics of the benchmark material ($IrO_x$) need to be understood at benchmark OER conditions. The studies that have investigated $IrO_x$ under these conditions have explored the activity of a single $IrO_x$ system and provided limited stability data.[41,45,83,117,122,124] While $IrO_x$ shows

superior stability to $RuO_x$, it is not indefinitely stable and certain forms of $IrO_x$ show rapid corrosion at moderate current densities ("high Tafel" region). Cherevko et al.[50,62,66,127,128] and Geiger et al.[62] performed thorough stability studies on the potentiodynamic dissolution behaviour for many of the $IrO_x$ films types listed in Table 3.1 under weak acid conditions, as well as short term steady-state profiling for $j < 10$ $mA \cdot cm^{-2}$.[50,66,127,128] The accelerated lifetime tests (ALT) uses CV to screen catalyst electrochemical stability and has primarily been used for PEM application.[74,83,84,88] CV has been used to diagnose the electrochemical instability of AIROFs.[50,65] All the aforementioned studies provide invaluable insight on the general dissolution characteristics of $IrO_x$, however some films exhibit enhanced dissolution from potential cycling,[63] performance discontinuities between regions of low, moderate and high $j$,[39,61] and faster corrosion under strong acid conditions.[67] Further, many of these studies are limited to evaluating the electrochemical stability of a material(s), which is not necessarily reflective of chemical stability. Given the limitations in the data available for $IrO_x$ under conditions relevant to SHC technology, the electrochemical performance of different $IrO_x$ systems should not be assumed to carry over across the different operational regimes.

$H_2SO_4$ and $HClO_4$ are both used to study the electrochemical properties of materials for acid mediated OER. The anion species of an acid can specifically adsorb to electrode surfaces and influence the electrochemical performance of catalyst materials.[129,130] Pt displays acid-specific ORR activities in $H_2SO_4$ and $HClO_4$,[82] and OER onset potentials are reported to show acid anion dependency.[131] This is often overlooked in OER studies and the performance of a material recorded in $HClO_4$ is extrapolated to

the equivalent molarity of $H_2SO_4$. The influence of acid species on the OER characteristics of $IrO_x$ does not appear to be explicitly outlined in the literature. Accordingly, the influence of acid species on the activity, selectivity and stability of $IrO_x$ materials under benchmark OER conditions is not understood.

OER studies are typically performed in 0.10 M, 0.50 M or 1.0 M acid concentrations, with the majority performed in lower acid concentrations (Table 3.1). The stability and activity profiles of $IrO_x$ materials should show pH dependent characteristics since $IrO_x$ surfaces are terminated by hydroxyl groups in aqueous solution.[82,87,89,91,132,133] Hydroxyl surface groups participate in acid-base chemistry with the electrolyte, so the dynamics at/on the surface of the electrode change with pH.[63,67,87,134–137] $IrO_x$ films are known to show markedly different electrochemical performances across broader pH ranges,[47,87,117,133] with electrodes showing reduced activity in near-neutral and basic electrolytes.[47] pH dependent performances have been reported for AIROF, ED and TD films across the acidic pH range.[87,135,137,138] These studies used inert salts to control for conductive differences, which is typically not done when screening catalyst OER performance.[82] The combined effect of pH and solution resistance on the OER performance of $IrO_x$ films is not well defined for the acid molarities most often cited in the literature. Comparison of catalyst performance between electrolyte molarities requires assumption of Nernstian behaviour and negligible resistive contributions.

$IrO_x$ films show preparation-dependent surface features (Table 3.1).[37,49,56,57,62,91] The influence of electrolyte conditions on $IrO_x$ OER performance should vary across the $IrO_x$ film types. This chapter summarizes efforts made to systematically characterize the influence of molarity and acid type on the observed OER characteristics of different $IrO_x$

films. The morphology, composition, activity, stability and selectivity of five $IrO_x$ film types were assessed using electrochemical and physical characterization techniques. The studied films were prepared on FTO-glass supports via drop-cast (DC), sputter (SIROF), thermally annealed sputter (T-SIROF), thermal decomposition of a precursor salt (TDPS) and anodic deposition (T-ED) techniques. Not all existing $IrO_x$ fabrication methods were explored in this work. However, the chosen fabrication methods represent a substantial portion of those historically employed in the characterization of $IrO_x$ OER activity[44,80,91,139] and those used as benchmark OER systems.[41,85,114,117,124] The electrochemical properties of the $IrO_x$ films were evaluated in 0.10 M, 0.50 M and 1.0 M $HClO_4$ and 1.0 M $H_2SO_4$. Film stability was assessed over a 24 h period using CP and complementary ICP-OES analysis of electrolyte solution. The electrochemical selectivity was probed using Faradaic efficiency measurements conducted over an ~2 h period. ICP-OES, SEM and XRD analysis were performed to provide compositional, morphological and structural information on the different film types. The results of these studies allowed for direct comparisons to be made regarding the performance and stability of different film types and their relative susceptibility to electrolyte environment. In the process, the influence of fabrication conditions on the observed properties of the $IrO_x$ were considered.

## 3.2 Experimental Section

### *3.2.1 Materials.*

Sodium hexachloroiridate(III) hydrate ($Na_3IrCl_6 \cdot xH_2O$, 99.8%), iridium(IV) oxide ($IrO_2$, 99.9%), perchloric acid ($HClO_4$, 70%), Nafion 117 solution (5% w/w) and fluorine-doped tin oxide glass substrates (FTO-glass, 100 x 100 x 2.3, 7 Ω/sq) were purchased from Sigma Aldrich. NaOH (NaOH, pellets, 98%) was purchased from ACP Chemicals Inc. Sulfuric acid ($H_2SO_4$, 98%) and nitric acid ($HNO_3$, 70%) were purchased from Caledon Laboratories Ltd. Hydrochloric acid (HCl, 37%) was purchased from Thermo Fisher Scientific Chemicals. Si wafers (0.3-0.4 Ω/cm, B-doped) were purchased from Addison Engineering Inc. Ag paste (Ag in isobutyl methyl ketone, #16040-30) was purchased from Ted Pella Inc. Cu wires used in electrode fabrication were Elenco® model WK106 (#22 gauge). The epoxy used to seal electrodes was Loctite® EA9460 manufactured by Henkel. Millipore water (Sartorius Arium Mini, 18 Ω/cm) was used for all electrochemical experiments. Silver/silver chloride (Ag/AgCl, 1 M KCl, $E_{vs.\ RHE} = 0.222$ V) and mercury/mercury chloride (Hg/HgO, 0.1 M NaOH, $E_{vs.\ RHE} = 0.098$ V) RE and platinum wire CE were purchased from CH Instruments Inc.

### *3.2.2 $IrO_x$ film fabrication*

Prior to all film fabrication, FTO-glass substrates were cleaned by ultrasonication in deionized (DI) water, acetone and isopropanol/ethanol for 15 min, respectively. The cleaned substrates were then dried with air prior to deposition procedures. All electrochemical cells and stir bars were cleaned with aqua regia and DI water prior to use

in electrodeposition experiments. Films were prepared such that each had a mass loading of ~0.75 $mg \cdot cm^{-2}$ Ir. A high precision scale (0.0001 g) was used to record the mass of film materials. All reported experiments were (at least) triplicated.

*Drop-cast (DC).* 5 mg/mL of $IrO_2$ powder in 3:1 isopropanol-DI water was ultrasonicated for ~ 30 min. FTO-glass substrates were dried under a stream of $O_2$ prior to catalyst deposition. The suspension was drop-cast onto clean FTO-glass substrates and allowed to dry under ambient conditions. This sequence of drop-cast and ambient drying was repeated until the desired mass loading was attained. After the final coat of $IrO_2$ dried, the films were annealed at 400 °C for 30 min (ramp rate 10 °C/min, hold 30 min, cool to RT) in air using a muffle furnace. DC samples prepared using a suspension matrix containing Nafion-117 were prepared in an analogous manner using a solution ratio of 0.2:3:1 Nafion-isopropanol-DI water. Films prepared with Nafion were annealed at 100 °C (30 min). Nafion-containing films exhibited poorer film-support contact relative to Nafion-free films, which adversely affected the film stability. Nafion-free DC films were used for all the reported experiments and characterizations.

*Thermal Decomposition of Precursor Ir Salt (TDPS)*. Solutions of 3.36 mg/mL of $Na_3IrCl_6 \cdot xH_2O$ in 1.2:1 isopropanol-DI water were prepared and ultrasonicated for ~1 h prior to initial use. The solutions were drop-cast onto clean FTO-glass substrates and allowed to dry for ~30 min under ambient conditions. The dried films were annealed at 400 °C for 30 min (ramp rate 10 °C/min, hold 30 min, cool to RT) in air using a muffle furnace. The sequence of drop-cast, ambient drying and annealing was repeated until the desired mass loading was attained. The solvent system used to deposit the salt precursor

onto FTO-glass was selected based on the solubility of $Na_3IrCl_6 \cdot xH_2O$. The deposited "wet" film must be fully dry before annealing to prevent film cracking.

*Sputter (SIROF).* Thin films of Ir were sputter-deposited onto clean FTO-glass substrates using a combinatorial sputtering system. Deposition was performed at 30 W (480 $W \cdot min$) under 2.6 sccm $Ar/O_2$ (4.89 mT) at room temperature for 20 min to give a film thickness of ~300 nm. Assuming formation of a smooth film, this thickness corresponds to a mass loading of ~0.75 $mg \cdot cm^{-2}$ for Ir. As-deposited films had mirror-like appearances. SIROF films were prone to delamination at the onset of OER if residual solvent tracks were present on the surface of the FTO-glass support at the time of film deposition.

*Sputter-Thermally Annealed (T-SIROF).* Sputtered films prepared following SP conditions outlined above were thermally annealed at 400 °C for 30 min (ramp rate 10 °C/min, hold 30 min, cool to RT) in air using a muffle furnace. Annealed films had muted and darkened features compared to SIROFs. T-SIROFs were less susceptible to delamination compared to SIROFs but had similar mechanical stability when supports were dried with a stream of gas prior to film deposition.

*Electrodeposition (T-ED).* A modified literature procedure was followed.[60,140] 50 mL of 0.01 M NaOH (aq) was stirred and heated to 70 °C. Once the solution was refluxing, $Na_3IrCl_6 \cdot xH_2O$ (0.0189 g) dissolved in 10 mL DI water was added. The mixture was refluxed for ~ 45 min and then cooled (and stirred) in an ice bath for ~15 min. After initial cooling, the (chilled) solution pH was measured using a pH probe (pH ~11.9). The cooled solution was then tuned to pH ~10 using dilute $HClO_4$ and had a clear, pale

yellow appearance. The electrodeposition solution (pH ~10) was added to a clean and dry electrochemical cell with a stir bar. An Hg/HgO (0.1 M NaOH) electrode and Pt wire were used as the RE and CE, respectively. The WE clamp was attached to a clean FTO-glass substrate and the connection was sealed off using non-conducting tape. The geometric surface area ($A_{geo}$) of the exposed FTO-glass was measured and then inserted into solution. Electrodeposition was performed using chronocoulometry and the working electrode was held at E = 0.95 V vs. RE until 0.3765 C/cm$^2$ (wrt $A_{geo}$) of charge was passed. Following deposition, the coated substrates were removed from solution and allowed to dry under ambient conditions for ~30 min before annealing at 400 $^{\circ}$C for 30 min (ramp rate 10 $^{\circ}$C/min, hold 30 min, cool to RT) using a muffle furnace. Electrodeposition solutions were used within 12 h of being prepared. Solutions began to form a blue precipitate over time that impacted film stability.

*3.2.3 Electrochemical Characterization*.

All electrochemical experiments were performed in glass cells cleaned with aqua regia and DI water. 0.1 M, 0.50 M and 1.0 M $HClO_4$ and $H_2SO_4$ electrolyte solutions were prepared using DI water. A Pt wire CE and Ag/AgCl (1.0 M KCl) RE were used for acid-mediated electrochemical experiments. $O_2$ gas was bubbled into the electrolyte for ~30 min prior to experimentation. LSV experiments were performed on electrodes using a sweep rate of $v$ = 10 mV/s and a starting potential ($E_i$) of 1.0 V vs. RE. The cell potential was swept to a final potential ($E_f$) of 1.8-2.2 V vs. RE. The WE was held at a resting potential ($E_{oc}$) for 2 min prior to applying the potential sweep. CP experiments

were performed at $j$ = 10 mA·cm$^{-2}$ (wrt $A_{geo}$) for all electrode systems. The experiments were performed for 24 h periods or until film/electrode failure. The uncompensated resistance ($R_u$) was measured for all film types using electrochemical impedance spectroscopy (EIS). The electrodes were held at open circuit potential ($E_{oc}$) and a frequency of 100 kHz with a voltage amplitude ($V_a$) of ± 10 mV was applied. $R_u$ was sampled 6 time per sample ($N_d$) to give an average value. *i*R correction were performed assuming 85% compensation.

The charge transfer resistance ($R_{CT}$) of SIROF, T-SIROF and TDPS films was measured using galvanostatic EIS at $j$ = 10 mA·cm$^{-2}$ with a current amplitude of ± 10 mA over a frequency range of 100 kHz-100 mHz.

An inverted burette set-up was used to measure the F.E. of the $IrO_x$ films. A constant current (density) was applied to the electrode for ~2 h and the evolved $O_2$ gas was collected. The amount of $O_2$ gas collected ($n_{experimental}$) was compared to the theoretical maximum for $O_2$ gas evolution ($n_{theoretical}$) at a given time.

Electrochemically Active Surface Area (ECSA) evaluation was performed by assuming the double-layer charging capacitance represented the reactive surface area. CV experiments were performed at various $v$ in 1.0 M $HClO_4$ and $H_2SO_4$. Working electrodes were held at $E_i = E_{oc}$ and then cycled between $E_1$ = 0.05 V vs. $E_i$ and $E_2$ = -0.05 V vs. $E_i$ at $v$ = 10, 25, 50, 75, 100, 150 and 200 mV/s. The anodic current measured at $E_{oc}$ + 20 mV was plotted against $v$ and linear regression analysis was performed on the resulting data set. The slope of the trendline was used as an estimate of the $C_{DL}$. $C_{DL}$ values are typically divided by a reference specific capacitance ($C_s$) to yield ECSA. Dividing the

ECSA by $A_{geo}$ provides an electrodes roughness factor. In the present chapter, $C_{DL}$ values were not divided by $C_s$ because a reliable reference value for $IrO_2$ (or $IrO_x$) was not found. Instead, the $C_{DL}$ values were divided by $A_{geo}$ in an effort to obtain a metric representative of the $A_{geo}$-normalized ECSA. Fresh (vs. aged) electrodes were used for ECSA experiments, thus the measurements represent the surface pre-catalysis.

*3.2.4 Physical characterization methods.*

ICP-OES experiments were performed using a PerkinElmer Optima 8000 instrument. The dissolved Ir content of 1.0 M $HClO_4$ and $H_2SO_4$ electrolyte samples was analyzed for 24 h CP experiments. The dissolved content was related to the initial (loaded) mass of Ir (~0.75 mg/cm$^2$). g-XRD patterns were collected using a Siemens D5000 operated at 45 kV, 40 mA and fitted with a scintillation detector. Samples of SIROF, T-SIROF, DC and TDPS films were prepared on Si wafers following the procedures detailed above. Samples were irradiated with incident X-rays at an angle (α) of 1° using Cu $K_{\alpha 1}$ radiation (λ = 1.5418 Å), a step width of 0.05 and a dwell time of 3 counts/s. SEM images of films were collected using a Hitachi S-4700 Field Emission Gun instrument in secondary electron (SE) mode. Samples were attached to SEM stubs using double-sided Cu tape and Ag paste was used to establish a connection between the conductive substrate face and sample stub. All samples were sputter coated with a 12 nm Au/Pd film to minimize sample charging. Sputter coating for SEM samples was performed using a model ACE200 Leica Sputter Coating System in diffuse mode for 156

s. Images were collected at sample heights of ~8-9 mm using an accelerating voltage of 3 kV and operating current of 7 kA.

## 3.3 Results and Discussion

### *3.3.1 $IrO_x$ film preparation and physical characterization*

Five $IrO_x$ film systems were prepared using different thin-film fabrication techniques. DC films were prepared using suspensions of commercial $IrO_2$ powder. Samples annealed at 400 °C showed improved support adherence relative to films annealed at lower temperatures. The DC method produced rough films with heterogenous surfaces (Figure 3.1B). The $IrO_2$ particles were polydisperse with sizes ranging from ~ 0.5-1 μm. The DC method yielded crystalline $IrO_2$ films (Figure 3.2A), as expected from the crystalline precursor.

SIROFs formed smooth surfaces (Figure 3.1C). Thermal treatment of SIROFs caused a structural change at the surface, as evidenced by the appearance of clustered structures in the SEM images of T-SIROFs (Figure 3.1D). Sanjines et al.[73] reported a similar transformation for SIROFs heated at 400 °C under UHV, whereby $IrO_2$ clusters formed in a matrix of lower-valence Ir. SIROFs undergo a phase transition to a more crystalline structure when they are heated. The temperature required for such structural rearrangement is preparation dependent, however reports have placed the amorphous-crystalline transition between 300-400 °C.[72,73,75] Crystallization of SIROF likely leads to structural damage as a result of lattice contraction. XRD analysis revealed similar structures for the T-SIROFs and SIROFs, suggesting surface-limited crystallization in the

T-SIROFs (Figure 3.2B and C). Both films showed broad peaks corresponding to $IrO_2$, suggesting their bulk structure to be composed of small crystallites.[141]

$IrO_x$ films were electrodeposited onto FTO-glass substrates using CC. Different ED conditions were trialed, including deposition using acidic, basic, fresh and/or aged $Ir(OH)_n^{x-}$ solutions. Acidic solutions formed blue, globular films and the solution composition visibly changed over the course of CC deposition from a clear amber solution to a grey-blue solution containing larger particulate species. Aged solutions (>1 day old) also formed a blue precipitate and the resulting films showed globular features. The blue precipitate is likely an agglomeration of $Ir(OH)_n^{x-}$ complexes.[77,78] Films deposited in the presence of these larger particulate species exhibited poor mechanical stability, possibly due to the lower density of surface bonding interactions at the FTO-film interface and/or great amounts of electrolyte being trapped between particles relative to smaller $Ir(OH)_n^{x-}$ species.

Fresh, basic electrodeposition solution formed smooth and uniform blue films with improved mechanical stability relative to the other tested conditions. The remaining films studied in this chapter were fabricated from fresh basic solution. T-ED films showed improved mechanical stability relative to the "wet" films. The T-ED films were composed of smooth sheets of material arranged into layers (Figure 3.1E). Thin AIROFs show similar morphological features to those observed for the T-ED films.[142] The g-XRD pattern of T-ED $IrO_x$ could not be collected as the films couldn't be grown on Si substrate (required for g-XRD experiments). We are currently exploring alternative substrates and attempting to grow thicker films to acquire the XRD data.

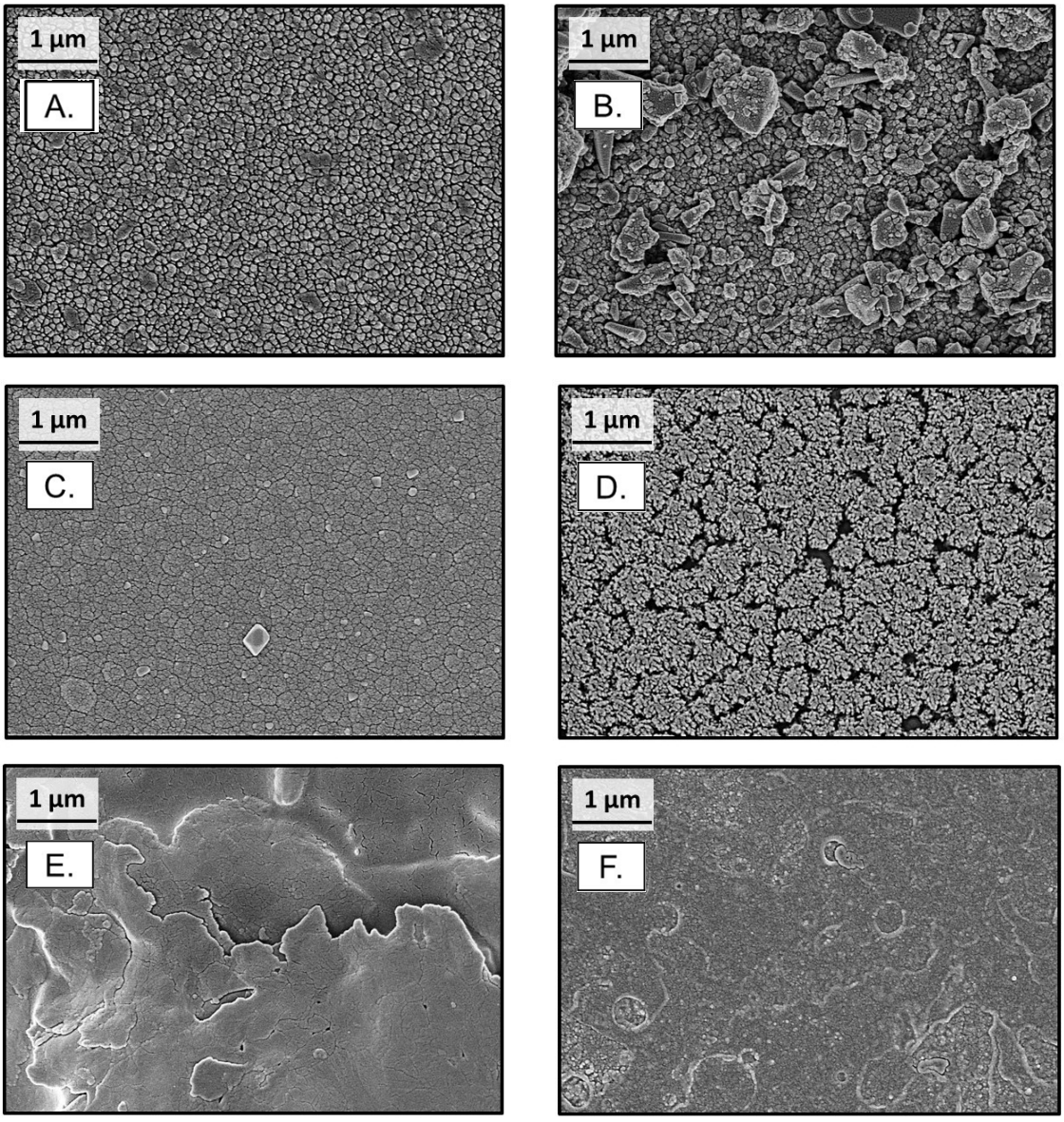


Figure 3.1: SEM images of the $IrO_x$ films: A) FTO-glass support, B) DC, C) SIROF, D) T-SIROF, E) T-ED and, F) TDPS.

TDPS films were prepared in-situ with the FTO-glass support. The films formed course surfaces composed of tightly packed small crystallites (Figure 3.1F, 3.2D). TDPS films showed reflections pertaining to $IrO_2$ (Figure 3.2D). TDPS films showed a strong

and comparatively sharp reflection at ~ 40°, which could be evidence of preferential orientation in the (200) direction of $IrO_2$.

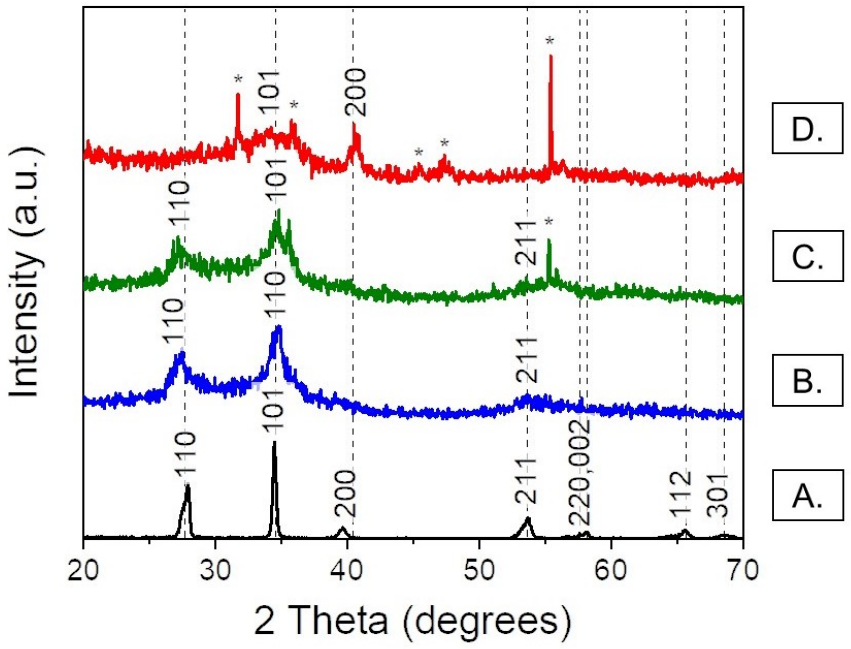


Figure 3.2: g-XRD patterns of $IrO_x$ films. A) DC, B) T-SIROF, C) SIROF), D) TDPS.[84,141] Peaks labeled * = Si.

Varying degrees of peak broadening are seen in the XRD patterns of the $IrO_x$ films, with DC films exhibiting the narrowest peaks. This is likely reflective of film crystallinity and suggests the DC films to have larger crystallites than the other $IrO_x$ films. TDPS films exhibited the most peak broadening, indicating the formation of smaller crystallites. Both SIROFs and T-SIROFs had intermediate-sized crystallites.

Powder XRD data can only be used to detect the presence of crystalline species. To analyze the complete elemental composition of the films, ICP-OES measurements were performed and the results are summarized in Table 3.2. DC, SIROF, and T-SIROF films were primarily composed of Ir and O with metal impurities <1 %. Both TDPS and T-ED films had significant amounts of Na and Cl impurities which likely results from the

precursor salt ($Na_3IrCl_6$) and NaOH solution (T-ED). All films had some amount of Sn which likely comes from the FTO substrate. Ti impurities in SIROF and T-SIROFs are likely due to contamination from the sputter chamber.

Table 3.2: Atomic percent composition of various $IrO_x$ films determined using ICP-OES.

| | Elemental composition (%) | | | | |
|---|---|---|---|---|---|
| **Film Type** | **Ir** | **Na** | **Cl** | **Other** | **O*** |
| **TDPS** | 25 % | 3 % | 5 % | 0.3 % Sn | 67 % |
| **SIROF** | 31 % | - | - | 1 % Ti, 0.3 % Sn | 68 % |
| **T-SIROF** | 32 % | - | - | 0.7 % Ti, 0.5 % Sn | 67 % |
| **T-ED** | 18 % | 7 % | 8 % | 0.7 % Sn, 0.1 % K | 66% |
| **DC** | 32 % | - | - | 0.8 % Sn, 0.1 % Ni, 0.1% Co | 67 % |

* ICP-OES cannot detect oxygen and its amount was estimated by subtracting the sum total of other elements from 100.

### *3.3.2 Electrochemical characterization of films in 1.0 M acids*

Both $H_2SO_4$ and $HClO_4$ are used as the electrolyte species in the characterization of acidic OER materials (Table 3.1). The performance observed in one acid is typically assumed to carry over to the other. However, anions can directly interact with electrode materials,[129,131] thereby altering the observed behaviour of the working electrode. $HSO_4^-$ has been demonstrated to have lower anodic stability relative to $ClO_4^-$ under oxidative conditions for $WO_3$,[130] which is one reason why $HClO_4$ is sometimes used in place of $H_2SO_4$. The lower stability is likely a consequence of $HSO_4^-$ tendency to specifically

adsorb on the electrode surface, where it can be oxidized. While the associated parasitic consumption of *j* may be negligible at low *j*, it should become more pronounced under more anodic conditions. To better understand the influence of acid anions on the electrochemical performance of $IrO_x$ films, the OER characteristics of the five $IrO_x$ films were investigated in 1.0 M $HClO_4$ and $H_2SO_4$. LSV was used to screen the film activities and the $\eta_{@j=10\ mA\cdot cm^{-2}}$ were extracted from the resulting curves following *i*R correction. Tafel analysis was performed on the *j*-*V* data for the log(*j*) range 0.5 to 1.2-1.5 to ensure the behaviour at/around $j = 10\ mA \cdot cm^{-2}$ was being modeled. Table 3.3 lists the $\eta_{@j=10\ mA\cdot cm^{-2}}$ and Tafel slopes for the $IrO_x$ films recorded in 1.0 M $HClO_4$ and $H_2SO_4$. All Tafel slopes had $R^2$ values of ≥ 0.99.

Table 3.3: Summary of $\eta_{@j=10\ mA\cdot cm\text{-}2}$ and Tafel slopes for $IrO_x$ films in 1.0 M $HClO_4$ and $H_2SO_4$.

| Film Type | $\eta_{@j=10\ mA\cdot cm^{-2}}$ (mV) | | Tafel slope (mV/dec) | |
|---|---|---|---|---|
| | **$HClO_4$** | **$H_2SO_4$** | **$HClO_4$** | **$H_2SO_4$** |
| **TDPS** | 270 ± 10 | 260 ± 6 | 58 ± 5 | 41 ± 6 |
| **SIROF** | 276 ± 7 | 270 ± 10 | 70 ± 6 | 65 ± 3 |
| **T-SIROF** | 300 ± 10 | 300 ± 4 | 70 ± 2 | 65 ± 9 |
| **ED** | 400 ± 10 | 420 ± 10 | 150 ± 10 | 162 ± 9 |
| **DC** | 330 ± 10 | 330 ± 10 | 90 ± 20 | 70 ± 10 |

Figures 3.3 shows representative *j*-*V* curves and Tafel plots for $IrO_x$ films in 1.0 M $HClO_4$ and $H_2SO_4$ following *i*R correction. The OER onset potential of a film was similar in both acids, with differences mainly being seen between the film types. The

$\eta_{@j=10\ mA\cdot cm^{-2}}$ were also similar under both conditions (Table 3.3). SIROF and TDPS films had the lowest $\eta_{@j=10\ mA\cdot cm^{-2}}$ values by ~30 mV, followed by T-SIROF, DC and T-ED films, respectively.

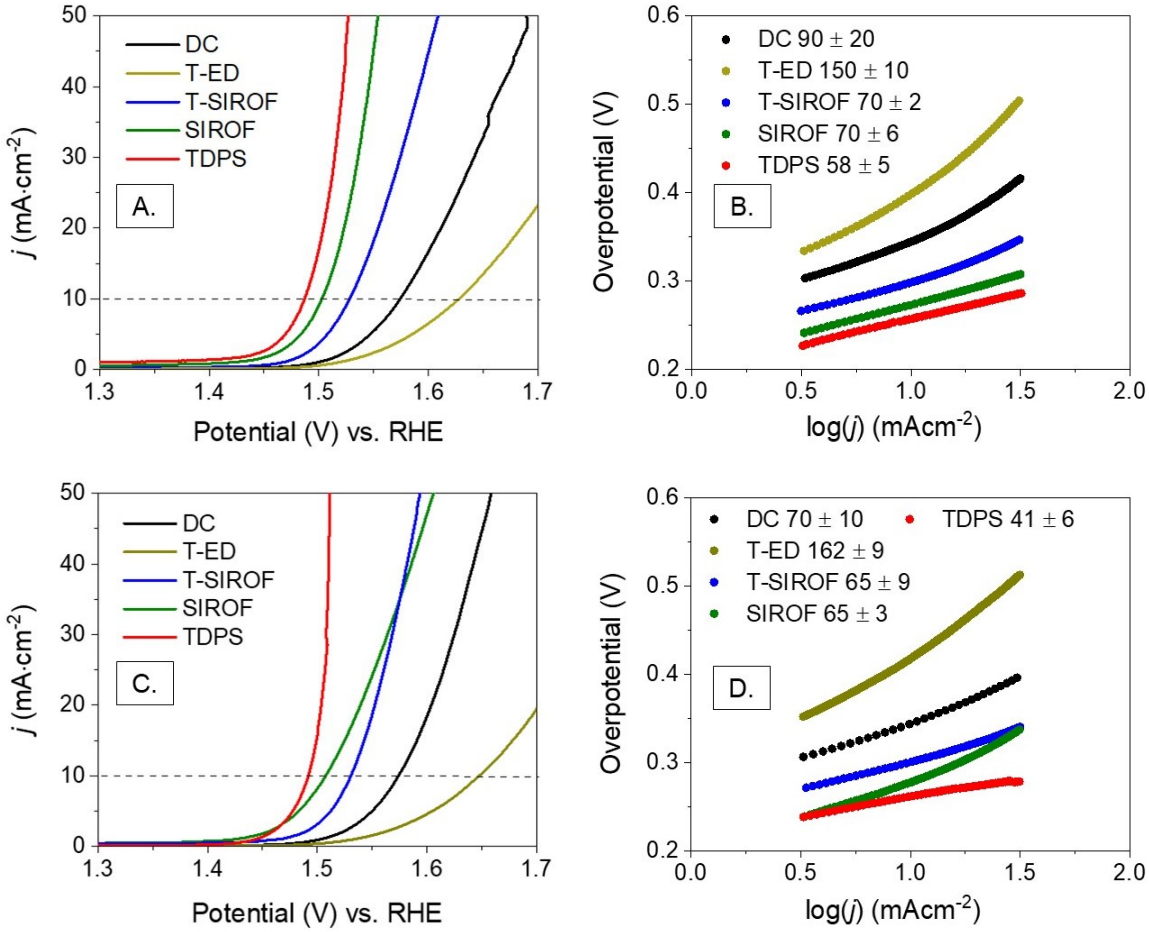


Figure 3.3: A) LSVs (*i*R-corrected) and B) Tafel plots of the $IrO_x$ film systems in 1.0 M HClO4. C) LSVs (*i*R-corrected) and D) Tafel plots of the $IrO_x$ film systems in 1.0 M - $H_2SO_4$.

As was mentioned in Ch. 1, many OER mechanisms have been proposed in the literature. Both solution- and lattice-phase mechanisms have been observed for OER on $IrO_x$ surfaces,[61,128] the former forming $O_2$ through a Volmer-Heyrovsky adsorbate

mechanism and the latter through a Volmer-Tafel oxygen exchange mechanism. A simplified lattice-based OER mechanism can be written as[31,50,56,87]

$$IrO_2 + H_2O \rightarrow IrO_2(OH) + H^+ + e^- \quad \text{Tafel slope} \sim 120 \text{ mV/dec} \quad (3.1)$$

$$IrO_2(OH) \rightarrow IrO_2(O)^- + H^+ \quad \text{Tafel slope} \sim 60 \text{ mV/dec} \quad (3.2)$$

$$IrO_2(O)^- + H^+ \rightarrow IrO_3 + e^- \quad \text{Tafel slope} \sim 40 \text{ mV/dec} \quad (3.3)$$

$$2\ IrO_3 \rightarrow 2\ IrO_2 + O_2 \quad \text{Tafel slope} \sim 30 \text{ mV/dec} \quad (3.4)$$

The RLS of a reaction mechanism influences the Tafel slope obtained for a catalyst. The Tafel slope predicted for each step in the lattice phase OER mechanism are shown above. From Table 3.3, the only films with values corresponding to the predicted Tafel values are TDPS films. In 1.0 M $H_2SO_4$, TDPS films were found to have a slope of ~40 mV/dec, which may suggest the RLS to be the second electron transfer reaction (equation 3.3). A different Tafel slope value (60 mV/dec) was observed for TDPS in 1.0 M $HClO_4$, which may suggest the RLS to be the second proton transfer (equation 3.2). The other $IrO_x$ films did not show Tafel slopes reflective of the predicted values. This could be due to multiple reaction mechanisms and/or RLS occurring simultaneously on the film surface. As well, while the Tafel slopes extracted for TDPS films align with predicted values, the OER mechanism may be different than the one outlined in equations 3.1-3.4. In-situ studies are required to elucidate the surface dynamics for the $IrO_x$ films.

There is limited OER mechanistic information available through the Tafel slopes, however the values can still be used to gauge the catalytic efficiency of the $IrO_x$ films.

Recall that smaller Tafel slopes are indicative of a more efficient catalyst (Ch. 1.3). TDPS films were found to have smaller Tafel slopes relative to the other films studied, followed by the two sputtered systems, DC and T-ED films, respectively. The catalytic efficiency therefore appears to decrease in the order TDPS, SIROF/T-SIROF, DC and T-ED in both 1.0 M $HClO_4$ and $H_2SO_4$.

TDPS films had slightly different Tafel slopes in 1.0 M $HClO_4$ and $H_2SO_4$, which could be reflective of different RLSs, as mentioned above. Both SIROF and T-SIROF films showed Tafel slopes of 65 mV/dec and 70 mV/dec in $HClO_4$ and $H_2SO_4$, respectively. The similar values observed between the films suggests ~equivalent catalytic efficiency for the two $IrO_x$ systems. As well, the η and Tafel slopes for SIROF and T-SIROF were comparable in both acids, suggesting acid type to have little influence on film activity under the conditions studied. DC and T-ED film activity also appeared to be ~independent of acid type. DC films showed smaller Tafel slopes compared to T-ED films, which showed values >120 mV/dec. The large Tafel slope observed for T-ED films could be due to film dissolution or poor conductivity at the film-support interface.

CP was used to assess the η stability of the $IrO_x$ films in 1.0 M $HClO_4$ and 1.0 M $H_2SO_4$. $IrO_x$ films were operated at $j = 10\ mA \cdot cm^{-2}$ over a 24 h period and the evolution of their η was observed, as depicted in Figure 3.4. Similar activity trends were observed at the initial stages of the CP experiment as was seen for LSV. TDPS and SIROFs showed the lowest η, followed by T-SIROF, DC and T-ED, respectively. Deviations arose after extended operation, with films showing varying degrees of activity losses.

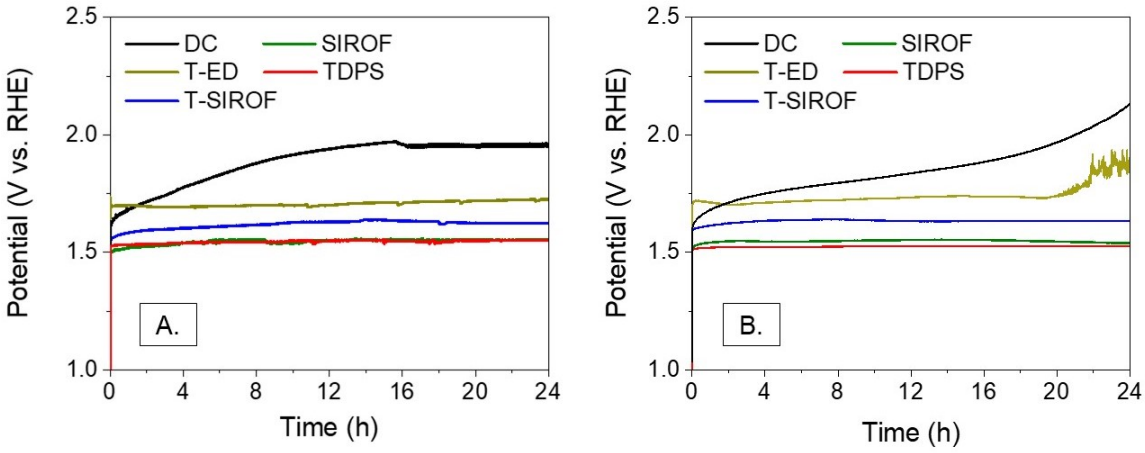


Figure 3.4: Representative CP plots of $IrO_x$ films in A)1.0 M $HClO_4$ and, B) 1.0 M $H_2SO_4$.

The activity-stability plots shown in Figure 3.5 (1.0 M $HClO_4$) and 3.6 (1.0 M $H_2SO_4$) afford better resolution of the η vs. time dependence exhibited by the $IrO_x$ films. In activity-stability plots, stable and active materials are represented by datapoints that start close to 0 mV and remain close to the bisecting line. TDPS, SIROF, T-SIROF and DC films showed increases in η (average) at early experimental time for 1.0 M $HClO_4$ and $H_2SO_4$ (Figure 3.5 and 3.6A, B). The η of SIROFs, T-SIROFs and TDPS films showed the greatest η increase within 20 min electrolysis, after which the increase was more gradual. Individual T-ED films showed decreasing η for the first ~2 h of OER in both acids, suggesting the in-situ formation of a more active catalytic species. Averaging across film replicates caused this behavior to be masked in the average η trend for T-ED films in 1.0 M $HClO_4$. T-ED films started to show increasing η after ~2 h electrolysis. The η of DC films surpassed that of T-ED films by 2 h OER (Figure 3.5 and 3.6B).

T-ED films showed variable stability in 1.0 M $HClO_4$, with some samples failing within 10-12 h of electrolysis (Figure 3.5C). Stable T-ED films showed η increases

similar to that observed for SIROFs in 1.0 M $HClO_4$. T-ED films did not show the same susceptibility for failure in 1.0 M $H_2SO_4$, however the η tended to increase more than that of stable T-ED electrodes in 1.0 M $HClO_4$. The average η of SIROFs, T-SIROFs and TDPS films stabilized after 12 h OER, however small η increases were observed for individual electrodes over the remainder of the experiment. By 24 h OER, DC films reached the highest η, with final values >300 mV than $\eta_{t=0}$ in both acids (Figure 3.5 and 3.6D).

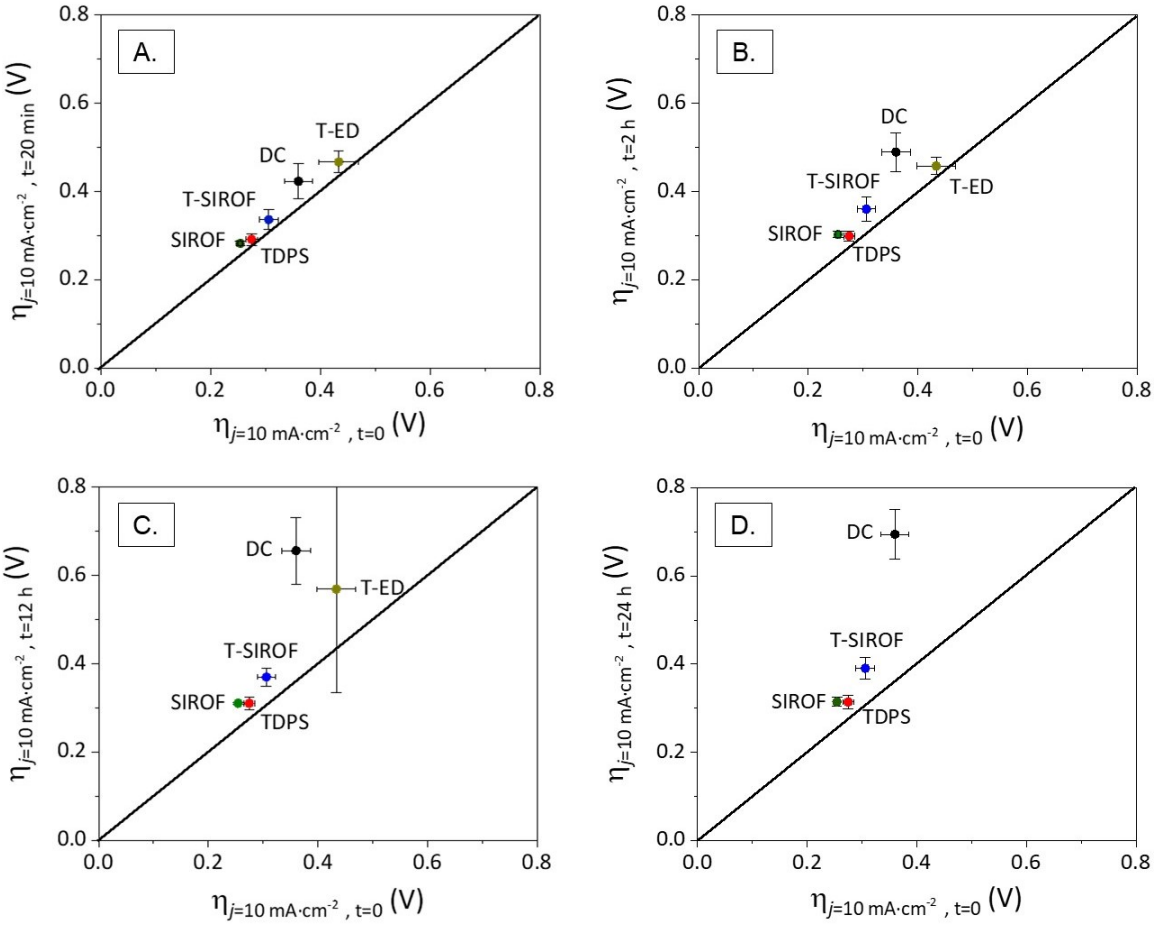


Figure 3.5: Activity-stability plots for the $IrO_x$ films in 1.0 M $HClO_4$. A) $\eta_{t=0}$ vs. $\eta_{t=20\ min}$, B) $\eta_{t=0}$ vs. $\eta_{t=2\ h}$, C) $\eta_{t=0}$ vs. $\eta_{t=12\ h}$ and, D) A) $\eta_{t=0}$ vs. $\eta_{t=24\ h}$.

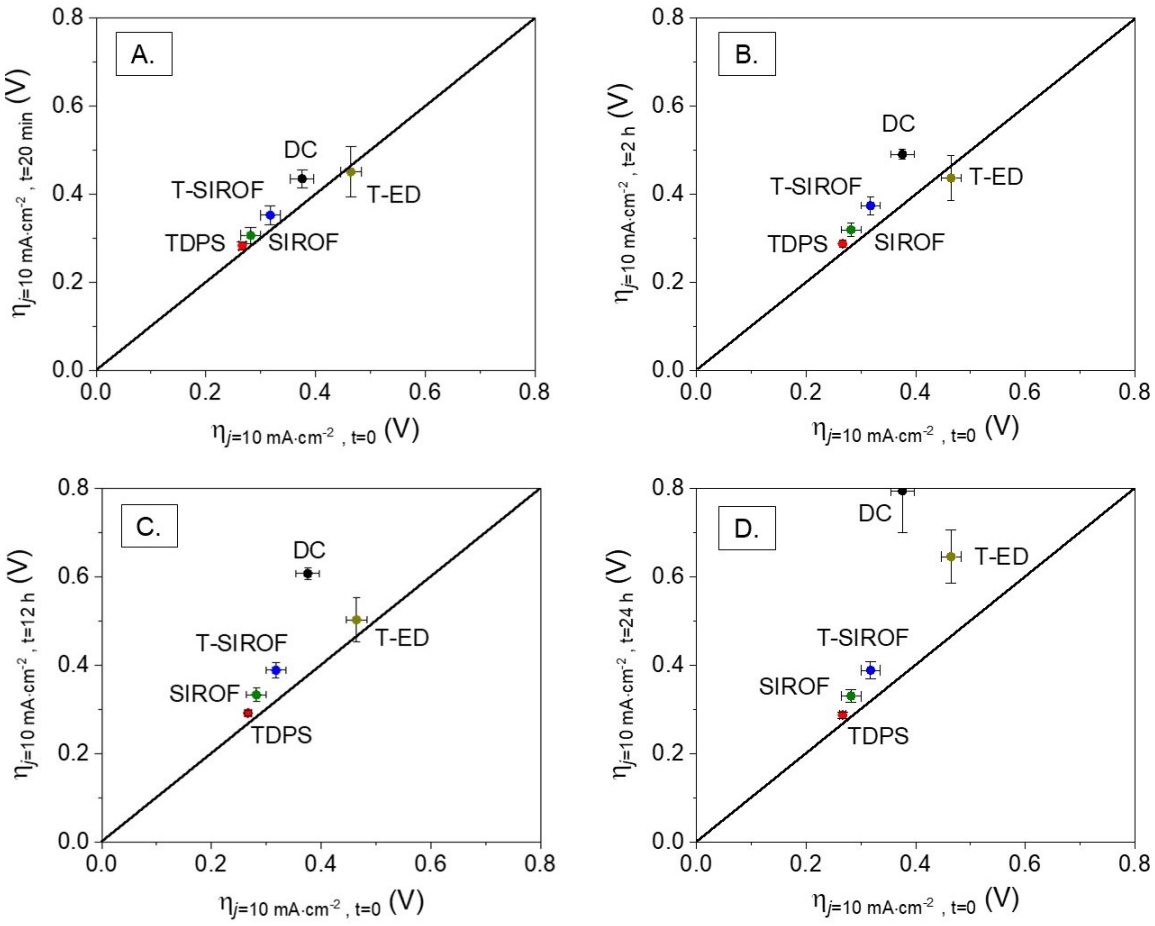


Figure 3.6: Activity-stability plots for the $IrO_x$ films in 1.0 M $H_2SO_4$. A) $\eta_{t=0}$ vs. $\eta_{t=20\ min}$, B) $\eta_{t=0}$ vs. $\eta_{t=2\ h}$, C) $\eta_{t=0}$ vs. $\eta_{t=12\ h}$ and, D) A) $\eta_{t=0}$ vs. $\eta_{t=24\ h}$.

Both DC and T-ED films showed limited stability in both acids and two different deactivation characteristics were observed. In the case of DC films, gradual deactivation was observed in both acids and a higher overpotential was observed in $H_2SO_4$. T-ED films showed abrupt failure in 1.0 M $HClO_4$ and a more gradual deactivation in 1.0 M $H_2SO4$. The abrupt deactivation is suggestive of full film delamination, which likely occurs due to the flaky morphology of T-ED films (Figure 3.1E). The gradual deactivations could be due to film surface oxidation, dissolution or exfoliation. Further

studies involving ICP-OES analysis of electrolyte over the 24 h experimental period are required to understand the activity loss observed.

Changes in the measured potential response can be understood as changes to the electrode surface. An increase in potential over operational time is indicative of some form of surface deactivation. Film dissolution and delamination are common causes of deactivation and can be probed through electrolyte analysis. ICP-OES was used to probe the extent of Ir mass loss experienced by the $IrO_x$ films in 1.0 M $H_2SO_4$ and $HClO_4$. Figure 3.7 shows the percent amount of dissolved Ir across the acid types for SIROF, T-SIROF, TDPS, DC and T-ED films after 24 h CP experiments. In general, a higher amount of Ir was observed in $H_2SO_4$ electrolyte compared to $HClO_4$ in all film types indicating higher dissolution in $H_2SO_4$. T-SIROFs and TDPS films had the lowest dissolution (< 2%) in both acids, followed by SIROFs. Both DC and T-ED films showed high levels of dissolved Ir after 24 h as predicted by the CP measurements. T-SIROFs showed better chemical stability compared to SIROFs despite having lower η-stability.

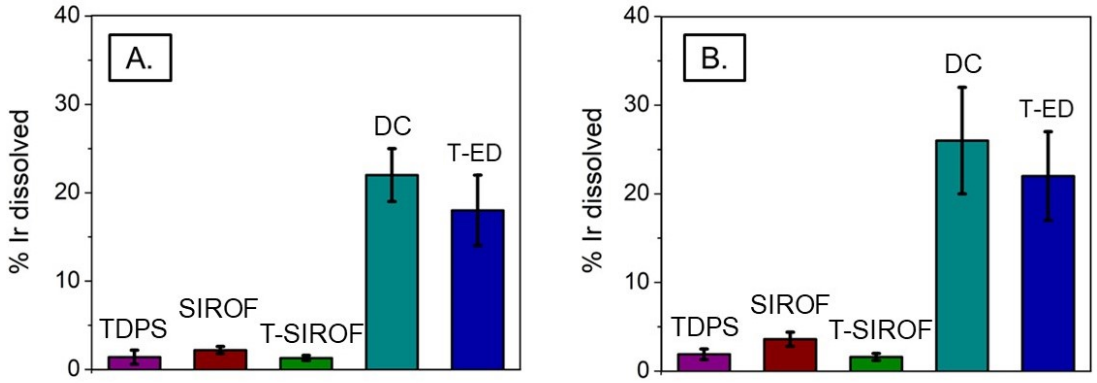


Figure 3.7: Amount of Ir determined using ICP-OES in, A) 1.0 M $HClO_4$ and B) 1.0 M $H_2SO_4$ for various films after 24 hours of CP measurements at $j$ = 10 mA · $cm^{-2}$.

Figure 3.8 compares the chemical stability and η-stability of the $IrO_x$ films. The η-stability of a film was represented using the change in η between t = 0 and t = 24 h for individual CP experiments. The high Ir content found in the electrolyte of DC and T-ED films after 24 h is consistent with film deactivation through catalyst dissolution/delamination.

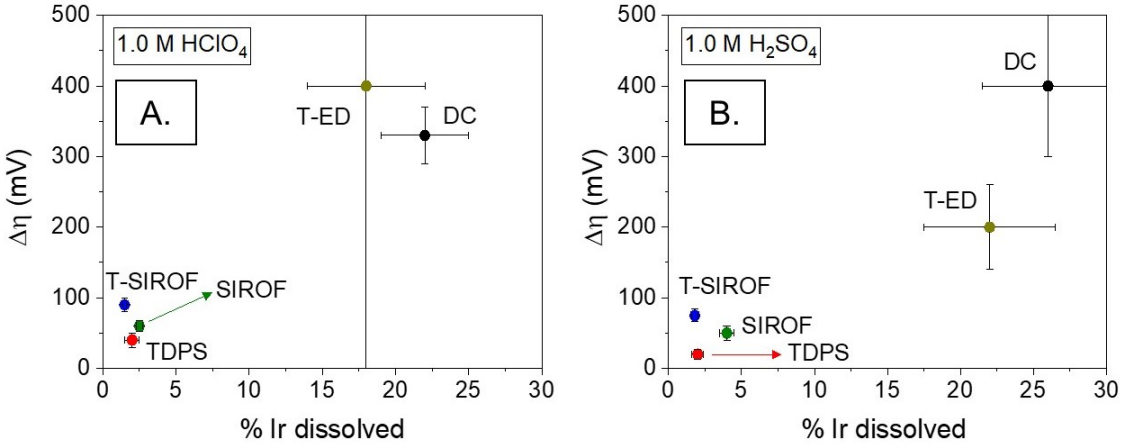


Figure 3.8: Influence of film dissolution on η-stability in A) 1.0 M $HClO_4$ and, B) 1.0 M $H_2SO_4$.

While LSV measurements help determine the catalytic activity and CP and ICP measurements establish film stability, F.E. measurements are performed to evaluate the catalyst selectivity for $O_2$ formation. The F.E. of the $IrO_x$ films were probed using an inverted burette set-up and are summarized in Table 3.4. All films showed lower F.E. in $H_2SO_4$ compared to $HClO_4$. In 1.0 M $HClO_4$, T-SIROF and TDPS films were found to have F.E. > 99 % whereas SIROF, T-ED and DC $IrO_x$ films showed F.E. < 99 %. In 1.0 M $H_2SO_4$, T-SIROFs and TDPS films had F.E. > 96% while SIROF, T-ED and DC films had F.E. < 95%. T-SIROFs and TDPS films showed the highest OER selectivity in both acids. However, it is currently unclear why these films show higher selectivity. The lower F.E. of the SIROF, DC and T-ED films suggests them to be more susceptible to parasitic

reactions. Oxidation of the $IrO_x$ films or FTO-film interface could contribute to the lower F.E.s. It is interesting to note that despite the presence of Cl impurities in TDPS films, $O_2$ evolution is favored over $Cl_2$ formation. This indicates the kinetics for the $Cl_2$ formation is either slower on these films or Cl atoms are well-encapsulated within the TDPS catalyst and not accessible for the reaction. The chlorine evolution reaction could contribute to the lower F.E. of T-ED films.

Table 3.4: Summary of the Faradaic efficiencies of various Ir films in 1.0 M $HClO_4$ and $H_2SO_4$ electrolytes.

| Film Type | 1.0 M $HClO_4$ | 1.0 M $H_2SO_4$ |
|---|---|---|
| **TDPS** | 99.7 % | 96.3 % |
| **SIROF** | 98.3 % | 94.1 % |
| **T-SIROF** | 99.8 % | 97.1 % |
| **T-ED** | 98.0 % | 93.0 % |
| **DC** | 98.2 % | 94.1 % |

The $A_{geo}$ of an electrode typically underestimates the real surface area participating in electrochemical reactions.[143] Films with higher active surface areas are expected to show higher activity due to the greater number of accessible reaction sites. The electrochemical active surface area (ECSA) of a film can serve as a metric of the accessible surface area of an electrode.[25,36,41] The double layer capacitance ($C_{DL}$), which is proportional to surface area accessible to electrolyte, can be used as a metric for electrode ECSA.[41] The ECSA of $IrO_x$ films was assessed in 1.0 M $HClO_4$ and $H_2SO_4$ (Figure 3.9). TDPS films were found to have the largest ECSA of the studied films while

DC and T-ED films showed the lowest ECSA in both acids. SIROF and T-SIROF films showed intermediate values.

Figure 3.9 shows the film η relative to its ECSA. It is possible that the activity trends observed for various $IrO_x$ films is due to the increasing surface area. However, the Tafel analyses indicate TDPS films to be intrinsically good catalysts so the high catalytic activity does not arise just from high surface area of the film. Further, surface area alone cannot explain the activity of SIROFs, which show smaller ECSA values relative to TDPS films despite having similar η in both acids. ECSA also does not address the difference in activity observed between SIROFs and T-SIROFs, since SIROFs show lower η relative to T-SIROFs in both acids but only have larger ECSA in 1.0 M $HClO_4$.

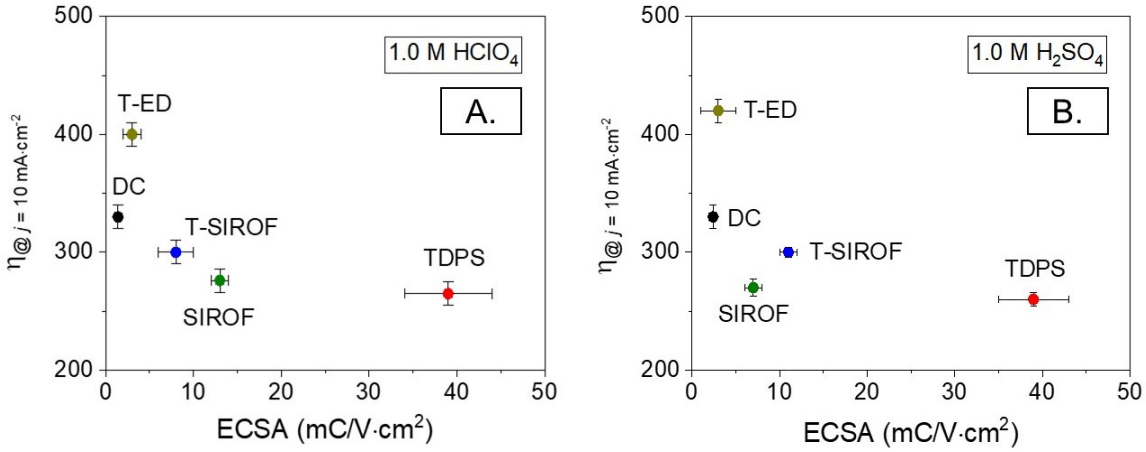


Figure 3.9: Relationship between ECSA (at $E_{OC}$) and η (LSV) for $IrO_x$ films in A) 1.0 M $HClO_4$ and B) 1.0 M $H_2SO_4$.

### *3.3.3 Electrochemical behaviour of $IrO_x$ films in different molarities of $HClO_4$*

$IrO_x$ surfaces are primarily -OH terminated in aqueous environments, with -OH and -OOH groups serving as the active sites for electrochemical processes under acidic conditions.[87,144–146] These surface groups participate in acid-base reactions and $IrO_x$

exhibits pH-dependent electrochemical properties as a result.[63,133,134,137,147] $IrO_x$ films are known to exhibit drastically different OER characteristics across acidic, neutral and basic solutions.[41,47,117,133] The trend within the acidic pH range is less defined and most existing studies are for AIROF and ED films.[63,77,87,134,135,137] These studies also use inert salts or buffered solutions to control for resistive differences, which is seldom done when screening OER electrocatalysts (Table 1). The extent to which the OER characteristics of $IrO_x$ films are influenced by pH-dependent interactions is not well understood, especially in the face of solution resistive differences. The OER characteristics of TDPS, SIROF, T-SIROF, T-ED and DC $IrO_x$ films were studied in 0.10 M, 0.50 M and 1.0 M $HClO_4$ (pH 1.0, 0.3 and 0, respectively) to determine how the activity and stability compared at different pH. $HClO_4$ electrolyte was chosen given the lower (average) catalyst dissolution and higher F.E. observed (Figure 3.8, Table 3.5). LSV was used to screen the film activities and the $\eta_{@j=10\ mA\cdot cm^{-2}}$ were extracted from the resulting curves following *i*R correction. Tafel analysis was performed on the *j*-*V* data for the log(*j*) range 0.5 to 1.2-1.5 $mA \cdot cm^{-2}$ to ensure the behaviour at/around $j = 10\ mA \cdot cm^{-2}$ was being modeled. Table 3.5 lists the $\eta_{@j=10\ mA\cdot cm^{-2}}$ and Tafel slopes for the $IrO_x$ films recorded in 1.0 M $HClO_4$.

Table 3.5: Summary of $\eta_{@j=10\ mA\cdot cm\text{-}2}$ and Tafel slopes for $IrO_x$ films in 0.50 M and 0.10 M $HClO_4$.

| Film Type | $\eta_{@j=10\ mA\cdot cm^{-2}}$ (mV) | | | Tafel slope (mV/dec) | | |
|---|---|---|---|---|---|---|
| | 1.0 M | 0.50 M | 0.10 M | 1.0 M | 0.50 M | 0.10 M |
| **TDPS** | 270 ± 10 | 283 ± 4 | 330 ± 10 | 58 ± 5 | 52 ± 4 | 51 ± 7 |
| **SIROF** | 276 ± 7 | 320 ± 10 | 353 ± 9 | 70 ± 6 | 83 ± 2 | 76 ± 6 |
| **T-SIROF** | 300 ± 10 | 350 ± 10 | 400 ± 20 | 70 ± 2 | 76 ± 9 | 95 ± 3 |
| **T-ED** | 400 ± 10 | 430 ± 20 | 420 ± 30 | 150 ± 10 | 150 ± 10 | 130 ± 20 |
| **DC** | 330 ± 10 | 370 ± 4 | 470 ± 30 | 90 ± 20 | 74 ± 3 | 90 ± 10 |

Figure 3.10 shows the *i*R corrected LSV and Tafel plots for the $IrO_x$ films in 1.0 M, 0.50 M and 0.10 M $HClO_4$. The same trend for $\eta_{@j=10\ mA\cdot cm^{-2}}$ was seen in 1.0 M and 0.50 M $HClO_4$, with films following the order TDPS > SIROF > T-SIROF > DC > T-ED. In 0.10 M $HClO_4$, T-ED films showed lower $\eta_{@j=10\ mA\cdot cm^{-2}}$ than DC films but the trend was otherwise comparable to the other acid molarities. Across the molarities, the $\eta_{@j=10\ mA\cdot cm^{-2}}$ increased for all films, with the largest change occurring between 0.50 M and 0.10 M $HClO_4$, except for T-ED films. T-ED films had similar η in 0.50 M and 0.10 M $HClO_4$, which could be reflective of slower surface corrosion in weaker acid.

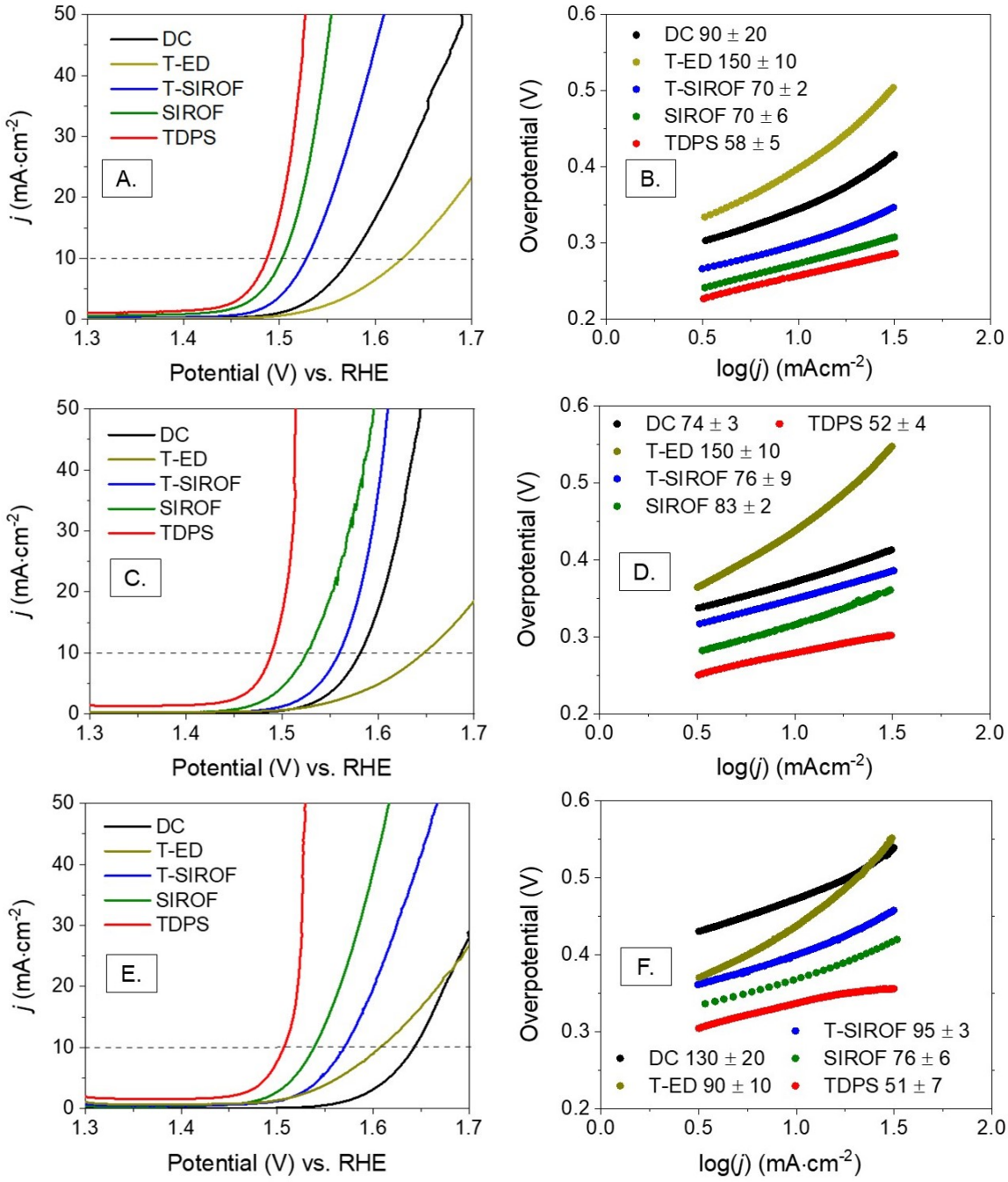


Figure 3.10: LSVs and Tafel plots, respectively, of $IrO_x$ films in A-B) 1.0 M $HClO_4$, C-D) 0.50 M $HClO_4$ and, E-F) 0.10 M $HClO_4$.

The trend in Tafel slope differed across the pH conditions. In 1.0 M $HClO_4$, the catalytic efficiency followed the order TDPS > SIROF ~ T-SIROF > DC > T-ED. The

order switched to TDPS > DC ~ T-SIROF ≥ SIROF > T-ED in 0.5 M $HClO_4$ and TDPS > SIROF > T-SIROF ~ DC > T-ED in 0.10 M $HClO_4$. The same general trend was observed for all molarities, with TDPS films having the lowest and T-ED films the highest slopes under all concentrations while T-SIROF, SIROF, and DC films exhibited intermediate values.

The activity-stability of the $IrO_x$ films was evaluated over a 24 h period for each of the electrolyte concentrations. Representative CP plots are shown in Figure 3.4A and 3.11 for the $IrO_x$ films in 1.0 M, 0.50 M, 0.10 M $HClO_4$, respectively. For all acid molarities, the early η trend followed the order TDPS > SIROF > T-SIROF > DC > T-ED. This contrasts with what was observed by LSV the $IrO_x$ films in 0.10 M $HClO_4$, where DC films showed higher η compared to T-ED films (Figure 3.10E).

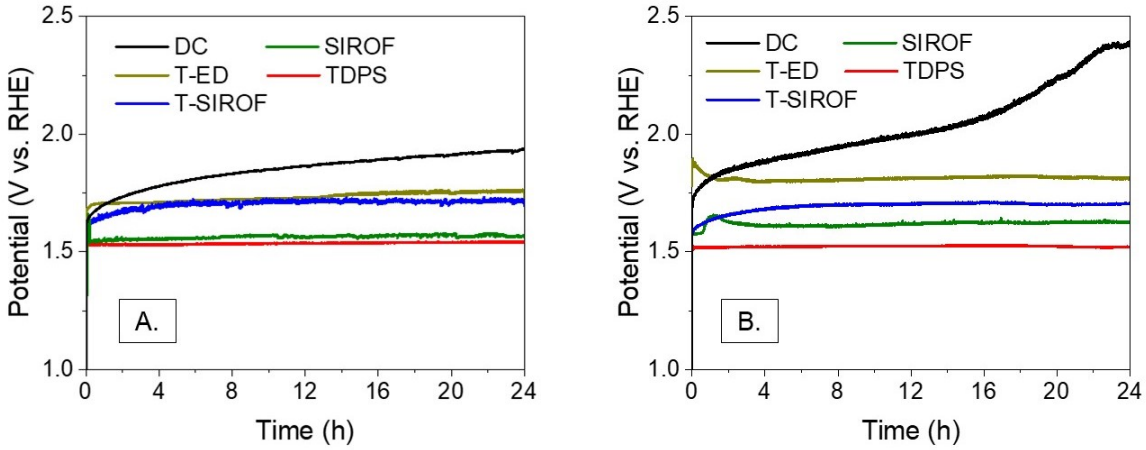


Figure 3.11: Representative CP plots for $IrO_x$ films in A) 0.50 M $HClO_4$ and, B) 0.10 M $HClO_4$.

The activity stability plots of the films in 0.50 M and 0.10 M $HClO_4$ are shown in Figures 3.12 and 3.13, respectively. TDPS, SIROF, T-SIROF and DC films had η that increased over the entire 24 h period, with the greatest increase observed within 2 h of

electrolysis for SIROF, T-SIROF and TDPS films. Individual T-ED films showed decreases in η at early experimental times, with η values typically increasing after 2 h OER for all molarities. As mentioned previously, the decrease observed for T-ED films is suggestive of an activation step. DC films started at η lower than T-ED films and exceeded T-ED films by 2 h OER for all molarities (Figure 3.5, 3.12 and 3.13B). The average η trend observed for TDPS films and SIROFs tended to show stabilization after a few hours of electrolysis in all molarities, however individual films never showed complete η stabilization.

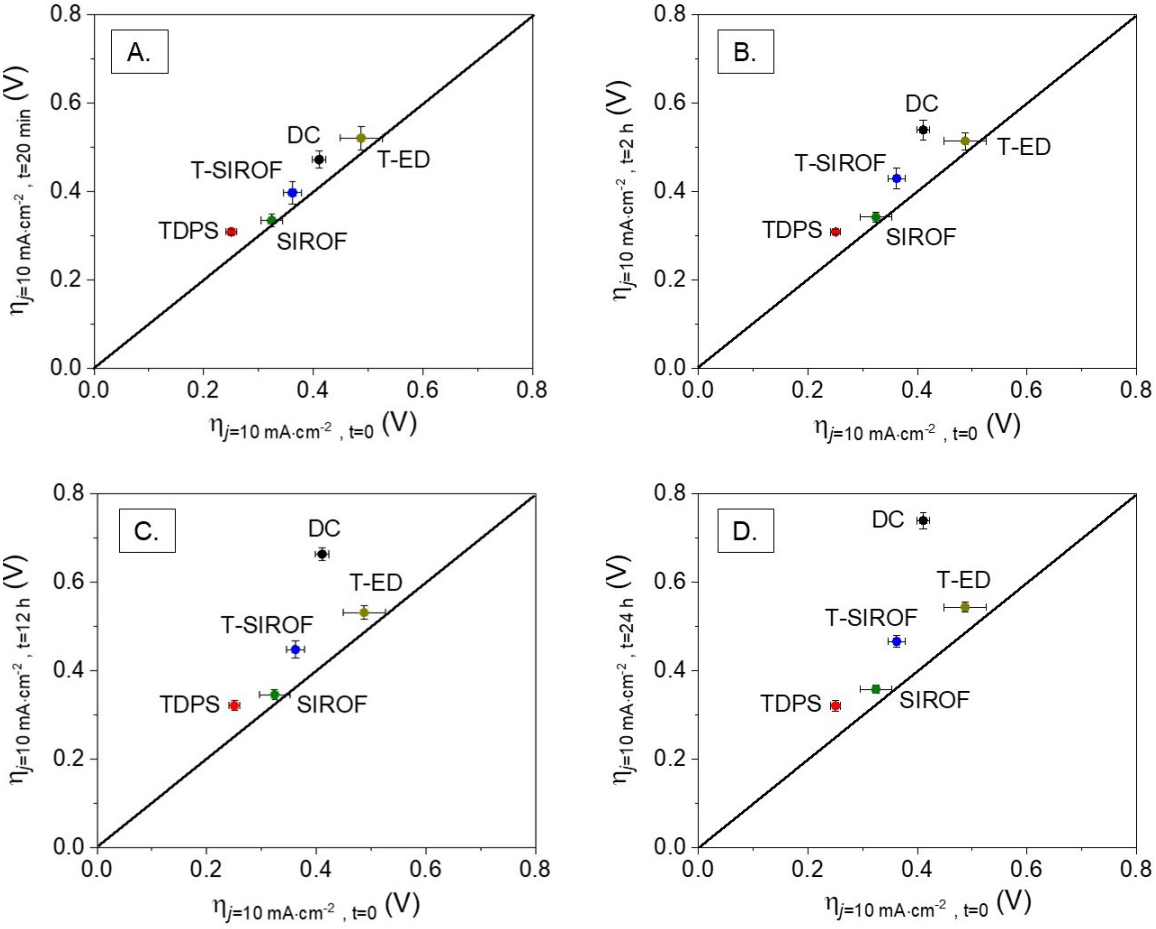


Figure 3.12: Activity-stability plots for $IrO_x$ films in 0.50 M $HClO_4$. A) $\eta_{t=0}$ vs. $\eta_{t=20\ min}$, B) $\eta_{t=0}$ vs. $\eta_{t=2\ h}$, C) $\eta_{t=0}$ vs. $\eta_{t=12\ h}$ and, D) A) $\eta_{t=0}$ vs. $\eta_{t=24\ h}$.

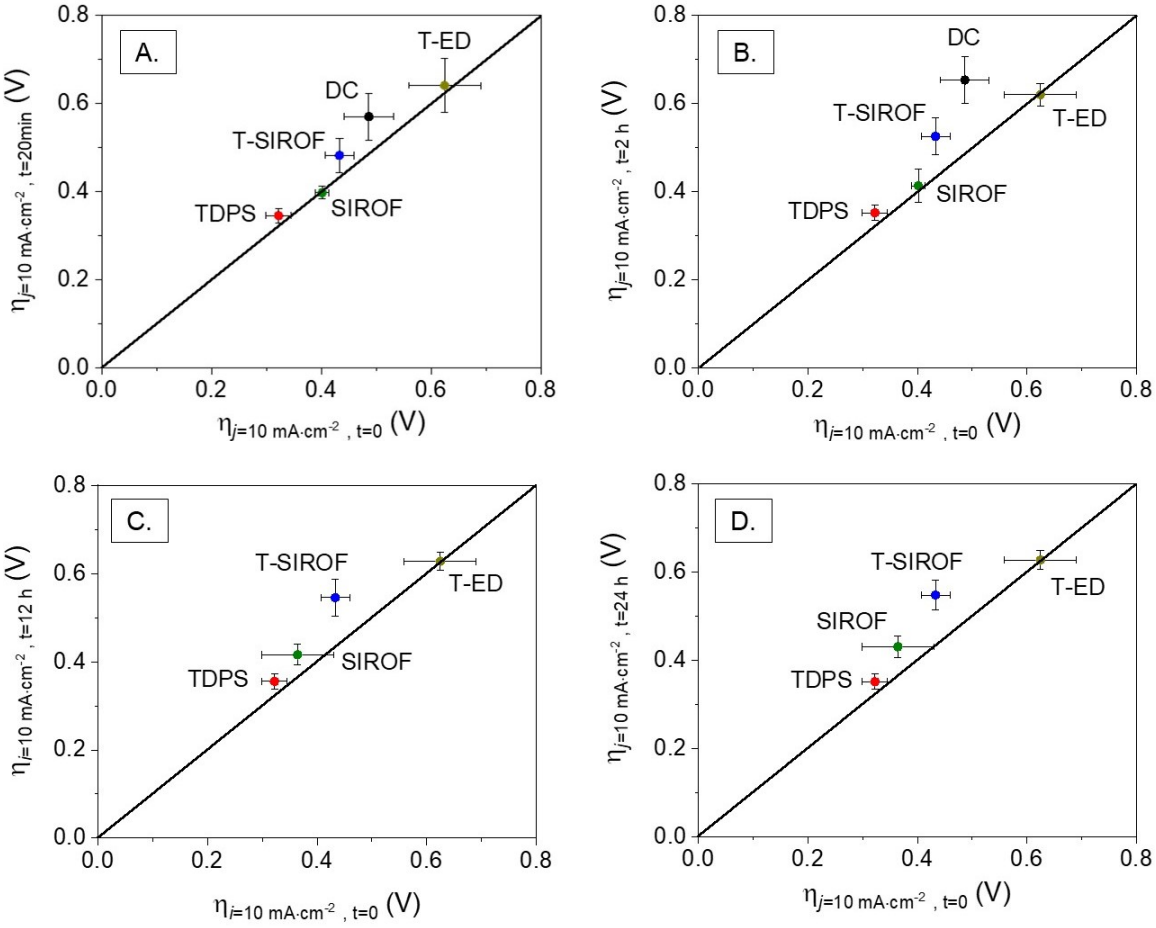


Figure 3.13: Activity-stability plots for $IrO_x$ films in 0.10 M $HClO_4$. A) $\eta_{t=0}$ vs. $\eta_{t=20\ min}$, B) $\eta_{t=0}$ vs. $\eta_{t=2\ h}$, C) $\eta_{t=0}$ vs. $\eta_{t=12\ h}$ and, D) A) $\eta_{t=0}$ vs. $\eta_{t=24\ h}$.

T-ED films showed large discrepancies between the η recorded by LSV and CP in 0.10 M $HClO_4$, with $\eta_{t=0}$ ~200 mV larger than $\eta_{LSV}$. There was less deviation between the η recorded by potentiodynamic vs. potentiostatic technique at lower pH. Ir films have been reported to show technique-dependent potentials and dissolution rates.[50,66] The rapid onset of ~large *j* in CP experiments leads to a rapid potential increase. Cherevko et al.[48] postulated that the rapid onset may lead to non-equilibrium conditions at the electrode surface if the potential increases at a rate higher than the surface-mediated response. Such conditions can result in film deactivation via passivation or dissolution,[50] causing the

surface to shift to more positive potentials. The authors[48] further suggested that since the potential increase occurs over a longer timescale for LSV experiments compared to CP, this may allow the electrode surface to stay in pseudo-equilibrium.

The η-stability of $IrO_x$ films in 1.0 M, 0.50 M and 0.10 M $HClO_4$ is depicted in Figure 3.14. The observed trends can be summarized as TDPS > SIROF > T-SIROF > DC > T-ED in 1.0 M, TDPS ~ SIROF ~ T-ED > T-SIROF > DC in 0.50 M and 0.10 M $HClO_4$. However, when activity is taken into consideration, the trend follows TDPS ~ SIROFs > T-SIROF > T-ED ~ DC in 1.0 M and 0.50 M $HClO_4$ and TDPS > SIROFs > T-SIROFs > DC ~ T-ED in 0.10 M $HClO_4$. SIROFs and TDPS films showed high activity and η-stability across the acid molarities, DC and T-ED films showed low activity and η-stability, and T-SIROFs showed moderate activity and η-stability.

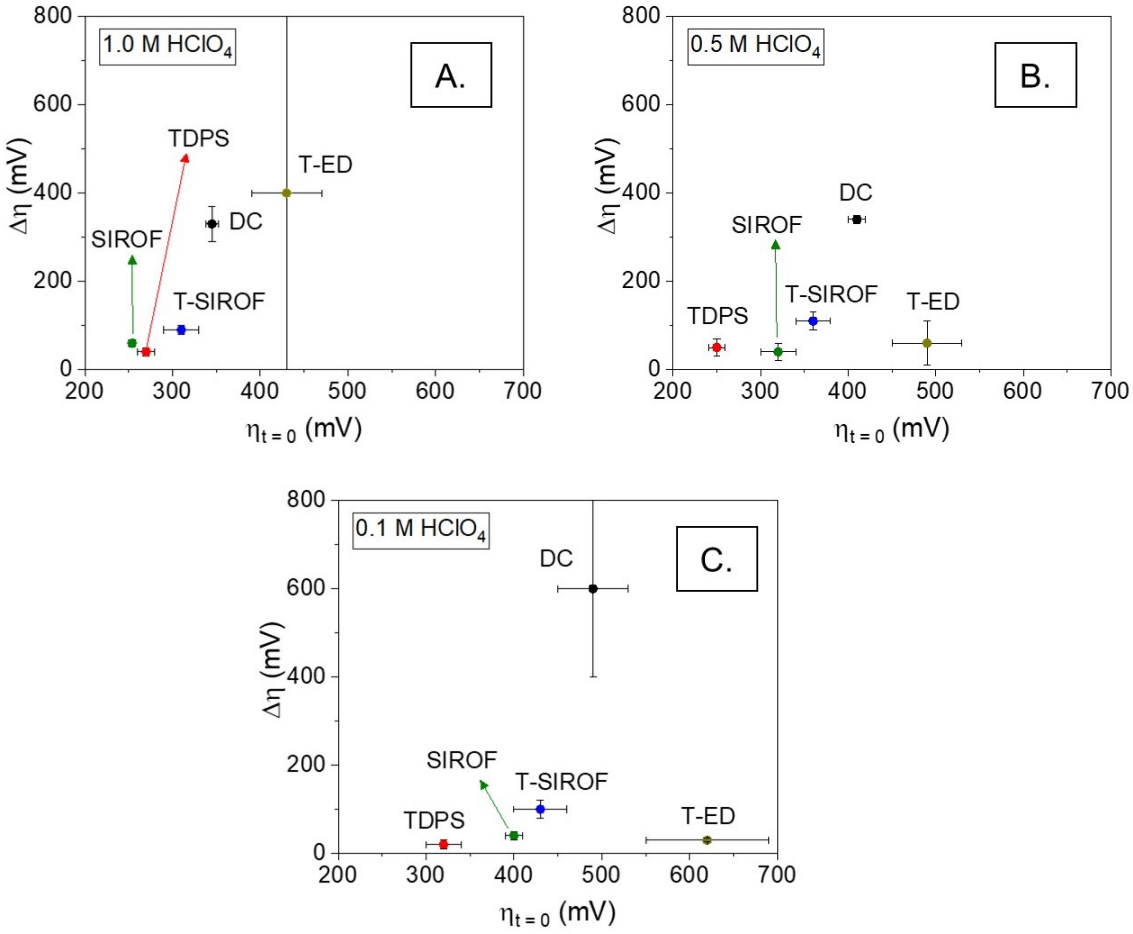


Figure 3.14: η-stability of $IrO_x$ films in A) 1.0 M, B) 0.50 M and B) 0.10 M $HClO_4$.

DC films showed the lowest η-stability across all acid molarities, reaching $\Delta\eta >$ 300 mV in each case and showed the highest $\Delta\eta$ in 0.10 M $HClO_4$ (~500 mV). The reduced η stability in lower electrolyte concentrations might be due to increased solution resistance, which increases the energy required to maintain $j = 10\ mA \cdot cm^{-2}$ and can cause film aggregation.[82] While DC films showed the lowest stability compared to other films, they were found to be more active than T-ED films over short experimental times. The moderate activity initially observed for DC films across all electrolytes is likely due to the mass loading and crystallinity of the film. The crystallinity can help with charge

transport through the films, making them effective catalysts at adequate loadings despite having low surface area and fewer defect sites relative to the more amorphous films.

T-ED films, which showed variable stability in 1.0 M $HClO_4$, exhibited improved η-stability at lower pH, with no tendency to fail within the 24 h operational period. The higher η-stability of T-ED films at higher pH might be due to slower surface dissolution or film passivation. The increasing resistance of the solution at higher pH and the large film-support resistance will make the surface kinetics of the T-ED films sluggish and more susceptible to non-equilibrium conditions as the electrode rapidly ramps to $j$ = 10 $mA \cdot cm^{-2}$. Film passivation during this potential onset period could reduce the Δη observed since most of the surface would already be in a deactivated state, as indicated by the large $\eta_{t=0}$.

T-SIROFs showed poor η-stability and high η relative to SIROFs across all electrolyte conditions. SIROFs showed η and η-stability similar to TDPS films, and both showed the highest η-stability and lowest η across all pH. TDPS films outperformed the SIROFs at lower molarities, with η ~ 60-80 mV lower than SIROFs at all times in 0.10 M $HClO_4$. SIROFs and T-SIROFs showed comparable Tafel characteristics under all electrolyte conditions except 0.10 M $HClO_4$, suggesting similar innate activity and surface dynamics. TDPS films, SIROFs and T-SIROFs showed similar $R_u$ under all electrolyte conditions, suggesting comparable charge transport efficiencies within the films and at the film-electrolyte interface. SIROFs and TDPS films had ~equivalent $R_{CT}$ values in 1.0 M $HClO_4$ and 0.50 M $HClO_4$, however SIROFs showed slight larger $R_{CT}$ in 0.10 M $HClO_4$ (Table 3.7). This is in line with LSV and CP data, which showed the films

to have similar activity (η) in 1.0 M and 0.50 M $HClO_4$ but TDPS films to outperform SIROFs in 0.10 M $HClO_4$ (Table 3.6). T-SIROFs had larger $R_{CT}$ than SIROFs and TDPS film under all pH conditions, also in line with the observed η trends.

Table 3.7: Charge transfer resistance for SIROF, T-SIROF and TDPS $IrO_x$ films in 1.0 M, 0.50 M and 0.10 M $HClO_4$ at $j$ = 10 $mA \cdot cm^{-2}$.

| Film Type | $R_{CT}$ ($\Omega \cdot cm^{=2}$) | | |
|---|---|---|---|
| | **1.0 M** | **0.50 M** | **0.10 M** |
| **TDPS** | 20 ± 2 | 22 ± 2 | 21 ± 2 |
| **SIROF** | 19 ± 4 | 20 ± 3 | 25 ± 1 |
| **T-SIROF** | 28 ± 6 | 28 ± 6 | 33 ± 5 |

SIROFs are reported to be microporous.[70,74] There does not appear to be reports that discuss the porosity, or lack thereof, for T-SIROFs. The g-XRD patterns and Tafel slopes presented in the current report suggest the two films to have similar intrinsic and sub-surface properties, including comparable catalytic efficiencies and bulk film structure. SEM imaging revealed the films to have different surface features, with the surface of T-SIROFs appearing to be terminated by $IrO_2$ clusters (Figure 3.1C).[73] This may indicate the two sputtered films have different surface energetics. $R_u$ can serve a measure of the conductivity of the overall electrode assembly, including the inter-film and film-support interfacial conductivity. More resistive films show higher $R_u$ under equivalent electrolyte conditions. $R_{CT}$ values provide insight on charge mobility at an electrode surface. Because SIROFs and T-SIROFs showed similar catalytic efficiencies (Tafel slopes) and appear to have similar bulk film structures, the higher $R_{CT}$ value observed for T-SIROFs may be

reflective of a less conductive surface that in turn requires more energy to complete Faradaic processes. SIROFs and T-SIROFs had similar $R_u$ but different $R_{CT}$ values under all the probed electrolyte conditions. This suggests that the movement of charge throughout the films mainly differs for the outermost surface. The later onset of OER in T-SIROFs suggests a more energetic surface charge-transfer process relative to SIROF films. If T-SIROFs have the same porous form as SIROFs at the film-support interface, then the major difference in the charge-transfer process between the two films should be charge moving across the film-electrolyte interface. Generally, more crystalline structures show improved electron mobility but reduced ion mobility relative to less ordered structures. Hackwood et al.[72] previously proposed ionic conductivity to be the major factor contributing to the reduced OER performance observed for T-SIROFs relative to SIROFs. The authors found the electronic conductivity of the two film types to be similar.[72]

A lower ion conductivity at the surface of T-SIROFs relative to SIROFs could result in a higher η requirement because more energy is required to transport an equivalent amount of charge across the electrode surface. Once enough energy has been provided to T-SIROFs to overcome the energy barrier associated with surface ion hopping, charge transfer across the SIROF and T-SIROF surfaces should proceed at similar rates. Thus, the efficiencies of the films after OER onset should be similar, as was observed by the similarity of the T-SIROF and SIROF Tafel slopes across most of the electrolyte conditions. The one exception is in 0.10 M $HClO_4$, where T-SIROFs had larger Tafel slopes compared to SIROFs. One explanation for why T-SIROFs showed different catalytic efficiencies than SIROFs at 0.10 M $HClO_4$ is that the low surface ion concentration is more debilitating for charge transport when combined with lower surface

ion mobility (T-SIROFs) relative to higher ion mobility (SIROFs). Recalling the definition of *j* outlined in Chapter 1,

$$j = nFk[X]_{surface} \quad (3.5)$$

$$j = nFk[H^+]_{surface} \quad (3.6)$$

Assuming $k \propto R_{CT}$, then the mix of lower acid concentration and slower surface reaction rate (T-SIROF) will result in a smaller *j* relative to lower acid concentration and a moderate surface reaction rate (SIROF). The structures proposed for the two sputtered films (Figure 3.15) are based on top-down SEM analysis, select electrochemical studies and literature findings. A combination of HI-RES cross-sectional SEM analysis, porosity studies and in-situ characterization of the sputtered films is necessary to more thoroughly investigate the films structures.

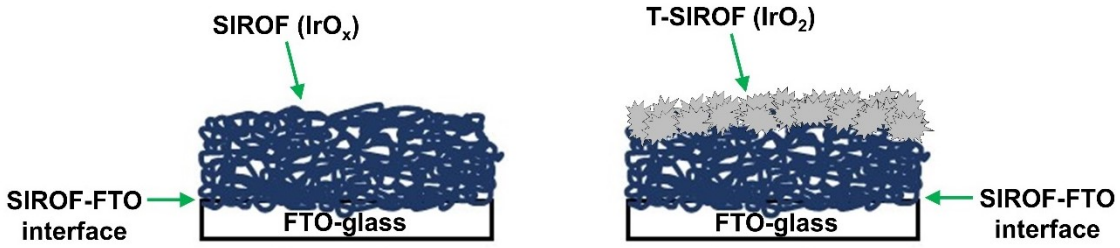


Figure 3.15: Proposed models for SIROF and T-SIROF structures.

### 3.4 Conclusion

$IrO_x$ films were prepared using five different common fabrication techniques typically reported in the literature. From the results, it is evident that the fabrication techniques greatly influence the activity and stability of the films. When evaluated in 1.0

M $HClO_4$ and $H_2SO_4$ at $j$ = 10 mA·cm$^{-2}$, TDPS films had low η, high catalytic efficiency and a high F.E. These films were also electrochemically and chemically stable over 24 h CP measurements. SIROFs showed similar activity as TDPS in terms of η, however SIROFs showed lower selectivity, catalytic efficiency and chemical stability in comparison. T-SIROF were found to have the next best combination of activity and stability, showing similar catalytic efficiency to SIROFs but higher η and reduced electrochemical stability. T-SIROFs showed selectivity (F.E.) and chemical stability comparable to that of TDPS films. T-ED and DC films performed inferiorly in comparison to the two sputtered films and TDPS films, exhibiting lower activity, lower stability (Δη and %Ir dissolved) and lower selectivity (F.E.). The poor performance of DC and T-ED films likely results due to unfavorable adhesion of the films to the substrate and between film particles/layers, resulting in more catalyst loss. In the case of T-ED films, film deposition was found to etch the conductive surface of the support substrate (FTO). T-ED films also appeared to exhibit an activation period, with the η decreasing in the first 2 h of OER. The other $IrO_x$ catalysts did not appear to require significant activation time.

The electrolyte species was found to influence the stability and selectivity of $IrO_x$ films more than the activity. Both the Tafel slope and η of films were comparable between the two acids. All films, with the exception of TDPS films, showed an average increase in film dissolution/delamination in 1.0 M $H_2SO_4$ compared to 1.0 M $HClO_4$. The electrochemical stability of the films appeared to be influenced by the acid type, specifically in the case of DC and T-ED films. Both films showed different η-stability behaviour in the two acids, with DC films showing greater deactivation in $H_2SO_4$ relative

to $HClO_4$. T-ED films showed a greater tendency to rapidly delaminate in $HClO_4$ compared to $H_2SO_4$. The OER selectivity of films appeared to be higher in $HClO_4$ relative to $H_2SO_4$ for all film types, potentially due to parasitic oxidation of $HSO_4^-$ in the latter electrolyte.

Electrolyte concentration was found to impact the OER properties of $IrO_x$ films. All films except T-ED films showed larger positive potential shifts than that predicted by the Nernst equation (i.e., >59 mV·pH) between 1.0 M $HClO_4$ and 0.10 M $HClO_4$. The exception of T-ED films could be reflective of a deactivated film state, since CP experiments suggest the films to undergo an activation process in the first 2 h at $j$ = 10 $mA \cdot cm^{-2}$. The η-stability of DC films decreased with molarity, while T-SIROFs, SIROFs, T-ED and TDPS films showed slight or no improvements with decreasing pH. These results highlight the importance of using a benchmark molarity for screening electrocatalyst OER performance.

This study shows that $IrO_x$ films are not necessarily stable, as is commonly claimed in the literature, and that film stability cannot be generalized across all $IrO_x$ systems. TDPS films, SIROFs, and T-SIROFs are better film fabrication techniques for yielding active and ~stable films. TDPS technique does not require a sputterer and is less infrastructure intensive though it can be time intensive. Sputtering, which can be fast, typically wastes a lot of material as it coats the entire chamber, which is undesirable when using expensive elements such as Ir. We currently do not understand all the trends observed in this study and further in-situ investigations are required to establish the

relationship between film composition and morphology, local Ir coordination environment, OER activity and stability.

# CHAPTER 4. ELECTROCHEMICAL WATER OXIDATION IN ACIDIC SOLUTION USING GROUP IV DIBORIDE CATALYSTS [3]

## 4.1 Introduction

As discussed in previous chapters, electrochemical fuel-forming processes, including hydrogen production from $H_2O$,[40,148–151] formation of hydrocarbons from $CO_2$,[152,153] and ammonia production from $N_2$[22,154] have the potential to disrupt the current energy landscape. These processes are all cathodic reactions and are typically coupled with the oxidation of water to produce oxygen at the anode to maintain charge balance and a sustainable electron supply.[155] Thus, active, stable, and Earth-abundant electrocatalysts for this OER must be simultaneously developed. Such catalysts have been demonstrated in alkaline[40,41,156–159] and neutral solutions,[160–162] but few examples have been reported in acidic media.[24] Acidic electrolytes are attractive as they are compatible with existing fuel-cell technologies, and with proton-exchange membrane-based electrolyzer systems that operate under high current densities and pressures.[32]

Oxides of noble metals, such as $IrO_x$ and $RuO_x$, have been commonly used as electrocatalysts for the OER in acidic solutions. These materials have been shown to generate the benchmark current density of $j = 10\ mA \cdot cm^{-2}$ towards the OER with

[3] Chapter 4 was adapted from the paper Electrochemical Water Oxidation in Acidic Solution Using Titanium Diboride ($TiB_2$) Catalyst, *ChemCatChem*, **2019**, *11*, 1-6 with permission from the authors Kirshenbaum, M. J., Richter, M. H., and Dasog, M. Copyright Wiley-VCH Verlag GmbH & Co., 2019. The author M. J. Kirshenbaum's contributions include performing XRD and SEM experiments, processing the electrochemistry data, as well as assisting with manuscript preparation. A. Nielander and M. Richter performed the electrochemistry and XPS experiments, respectively.

overpotentials <500 mV.[41,46,116,119] However, the scarcity and cost of these materials may preclude global-scale transformation of energy storage. Ta-based intermetallic alloys,[96] polyoxometalates,[99] and metal-oxides[97,163,164] have been explored as alternatives to noble-metal based materials, but do not exhibit substantial electrochemical stability. Materials that exhibit appreciable stability such as the $Ni_{0.5}Mn_{0.5}Sb_{1.7}O_y$ have poor conductivity and require overpotentials of >700 mV to overcome the resistance.[95,100] In industrial electrochemical processes, boride coatings have been used to reduce corrosion in acidic electrolytes.[165–167] Recently, Earth-abundant metal borides have emerged as efficient OER electrocatalysts owing to their good electronic conductivity and chemical robustness.[168] Furthermore, the presence of boron has been proposed to lower the thermodynamic and kinetic barrier of the hydroxylation step involved in the water oxidation process.[169] Co, Fe, and Ni borides have been shown to exhibit OER performance that exceed Ir- and Ru-based catalysts in basic solutions.[169,170] While metal borides have been investigated as OER electrocatalysts in alkaline solutions, such materials remain unexplored in acidic media. In this study, the OER performance of commercially available $TiB_2$, $HfB_2$ and $ZrB_2$ powders on FTO substrates in 1.0 M $HClO_4$ and $H_2SO_4$ is reported.

## 4.2 Experimental Section

### *4.2.1 Materials*

Titanium diboride ($TiB_2$, ~10 μm powder), perchloric acid ($HClO_4$, 99.999%), sulfuric acid ($H_2SO_4$, %), fluorine doped tin oxide (FTO) coated glass (surface resistivity

of ~7 $\Omega/m^2$ ), Nafion-117 solution, hydrochloric acid (HCl, ≥ 99%), and nitric acid ($HNO_3$, ≥ 99%) were purchased from Sigma-Aldrich. Zirconium diboride ($ZrB_2$, hexagonal, 5 μm powder) and Hafnium diboride ($HfB_2$, 1.5 μm powder) were purchased from USnano. A $TiB_2$ sputtering target (1.0'' dia. x 0.250'' thick) was purchased from Kurt J. Lesker Company. Millipore water (≥18.2 MΩ/cm resistivity) was obtained from a Barnstead E-Pure system. An Ag/AgCl (1.0 M KCl) reference electrode and a Pt wire counter electrode were purchased from CH instruments.

*4.2.2 Electrode preparation*

The working electrodes were prepared by drop-casting boride dispersions or by sputtering ($TiB_2$) onto an FTO-glass substrate. Prior to deposition, the FTO-glass substrates were cleaned by ultrasonication in ethanol for 2 min and rinsing sequentially with acetone and deionized water. For drop-casting, catalyst solutions were prepared by dispersing 10 mg of a metal boride powder in 1 mL of 4:1 v/v isoproponal/5% Nafion via sonication. The resulting suspensions were then drop-cast onto an FTO-glass substrate until a catalyst loading of 2.0 $mg \cdot cm^{-2}$ was reached and dried at 40 °C in an oven for 2 h. Thin films of $TiB_2$ were sputtered onto cleaned FTO substrates using conventional RF sputtering at 40 W with an Ar flow of 1.7 sccm and chamber pressure of 1.97 mT. The film thickness was controlled by varying the deposition time.

*4.2.3 Electrochemical experiments*

All the electrochemical experiments were conducted using a Biologic SP-150 potentiostat in a single-compartment, three-electrode cell in 1.0 M $HClO_4$ or $H_2SO_4$. The electrochemical cells were washed with aqua regia and Millipore water prior to the electrochemical measurements. Pt wire and Ag/AgCl (1.0 M KCl) were used as the counter and reference electrodes, respectively. The electrolyte was circulated using an external pump. LSVs were collected in a $O_2$-purged cell at a scan rate of 5 $mV \cdot s^{-1}$. The stability of the catalyst was examined using CP at a current density of 10 $mA \cdot cm^{-2}$. Electrochemical impedance measurements were carried out from 100 kHz to 100 mHz with an amplitude of 10 mV at 0 V vs SCE. All the electrochemical measurements were corrected for uncompensated resistance using the $R_u$ values obtained from the impedance measurements. Experimental F.E. of DC $TiB_2$ was determined by collecting the evolved gas using an inverted burette at a current density of 10 $mA \cdot cm^{-2}$.

*4.2.4 Physical characterization*

Powder XRD patterns were collected using a Rigaku Ultima IV X-Ray diffractometer with Cu Kα radiation (λ = 1.5418 Å). The samples were placed onto a zero-background Si wafer and the diffractograms were collected at 3 counts/s. SEM images were obtained using a Hitachi S-4700 electron microscope. ICP-OES measurements were performed using a PerkinElmer Optima 8000 instrument. XPS data were collected using a Kratos Axis Ultra system with a base pressure of $1 \times 10^{-9}$ Torr. The X-ray source was a monochromatic Al Kα line at 1486.6 eV. Photoelectrons were

collected at 0° from the surface normal with a retarding pass energy of 160 eV for survey XPS scans, 20 eV for high-resolution core levels scans. CasaXPS software (VAMAS) was used to interpret and fit high-resolution (HR) XP spectra. All spectra were internally calibrated to the C 1s emission (284.8 eV).

### 4.3 Results and Discussion

The electrochemical activity and stability of drop-cast $TiB_2$, $HfB_2$ and $ZrB_2$ films were assessed in 1.0 M $HClO_4$. $ZrB_2$ and $HfB_2$ films were found to have onset overpotentials ≥ 1 V and were unstable when the films were operated at $j = 10\ mA \cdot cm^{-2}$ beyond 5 min. The reduced catalytic activity may have been a result of rapid oxidation of $ZrB_2$ and $HfB_2$ films under anodic conditions. In contrast, DC $TiB_2$ films showed favourable electrochemical activity and stability in 1.0 M $HClO_4$. These films were therefore investigated more thoroughly.

Figure 4.1A presents a powder XRD pattern of the $TiB_2$ powder, which shows characteristic peaks at 27.6°, 34.2°, 44.5°, 57.0°, 61.2°, 68.1°, 68.4°, 72.1°, and 78.7° that can be indexed to the (001), (100), (101), (002), (110), (102), (111), (200), and (201) crystal planes, respectively, of the layered $TiB_2$ structure.[171] The reflections at 38.4° and 65.1° likely correspond to the (020) and (130) crystal planes of the α″-martensite phase of Ti metal.[172] SEM analysis of $TiB_2$ powder showed particles ranging between 5-15 μm (Figure 4.1B). ICP-OES measurements did not indicate the presence of noble metal contaminants such as Ir, Ru, and Pt in detectable amounts (>10 ppb).

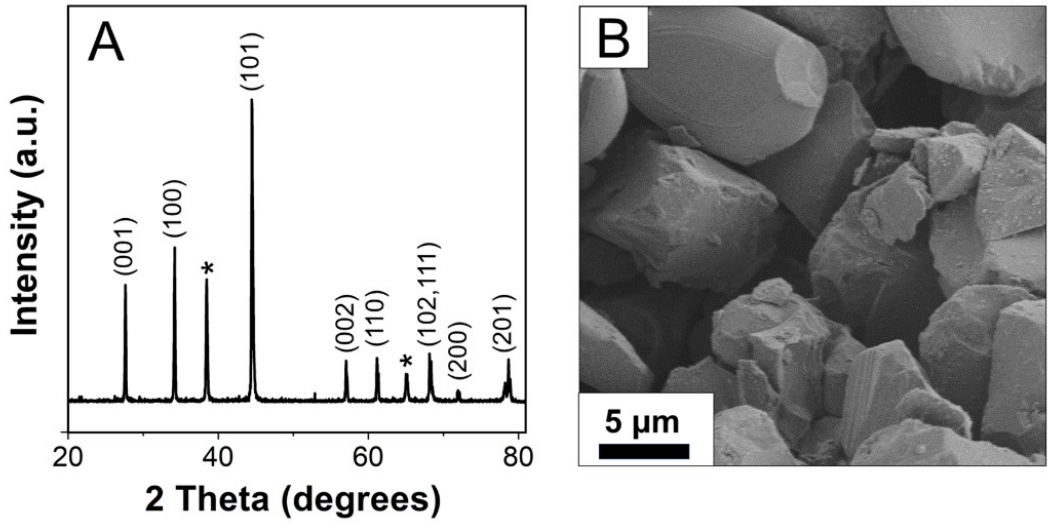


Figure 4.1: (A) Powder XRD pattern and (B) SEM image of $TiB_2$ particles. The * in (A) denotes reflections corresponding to α″-martensite phase of Ti metal.

$TiB_2$ microparticles were suspended in Nafion solution and coated onto an FTO-glass substrate to achieve a geometric concentration of 2.0 $mg \cdot cm^{-2}$. Figure 2A shows a cross-section SEM image of the drop-cast $TiB_2$ film with a thickness of ~10 µm (Figure 4.2A). The electrocatalytic activity of $TiB_2$/FTO for OER was assessed in 1.0 M $HClO_4$ and $H_2SO_4$ (pH = 0) solutions. The solution resistance was determined to be 7.6 Ω and 7.9 Ω by electrochemical impedance (Figure 4.2B) in $HClO_4$ and $H_2SO_4$ solutions, respectively, and all electrochemical measurements were corrected for uncompensated resistance accordingly. This suggests good film-support contact, as well as inter-particle conductivity, since the $R_u$ of bare FTO-glass is ~ 3x the $R_u$ of $TiB_2$ and DC films of other electrocatalysts were found to have $R_u$ ~equivalent to that of FTO-glass.

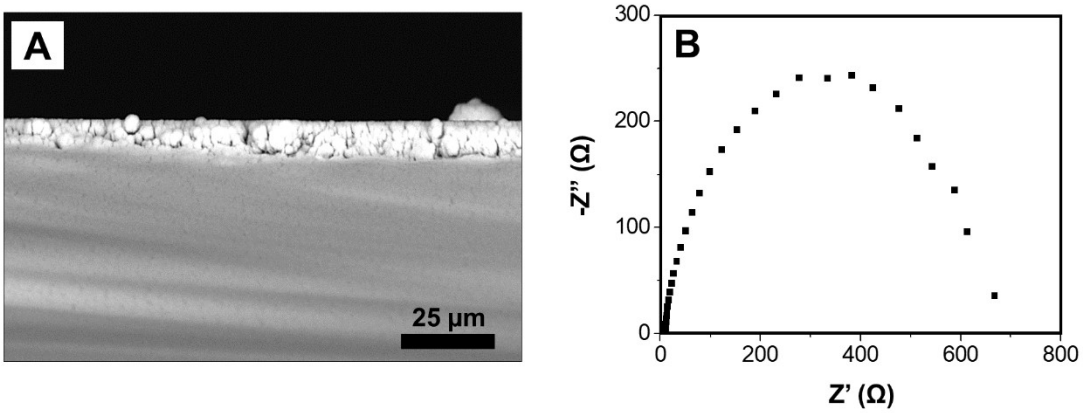


Figure 4.2: (A) Cross-section SEM image of $TiB_2$ drop-coated FTO substrate and (B) Nyquist plot (Ru = 7.6 Ω) for $TiB_2$ electrocatalyst in 1.0 M $HClO_4$.

Figure 4.3 shows a LSV for the catalyst in 1.0 M $HClO_4$, which demonstrates that an η of 560 ± 20 mV (1.79 V vs RHE) is required to achieve a current density of $j$ = 10 $mA \cdot cm^{-2}$. CP experiments in 1.0 M $HClO_4$ demonstrate that the $TiB_2$ catalyst is capable of sustained oxygen production for at least 10 h at $j$ = 10 $mA \cdot cm^{-2}$ (Figure 4.4) with negligible changes in overpotential. Many of the reported EA OER catalysts tested in acidic solutions have not been investigated at pH values as low as 0, nor reach current densities as high as 10 $mA \cdot cm^{-2}$, which is the target benchmark for application in a variety of technologies including the storage of solar energy.[40,149]

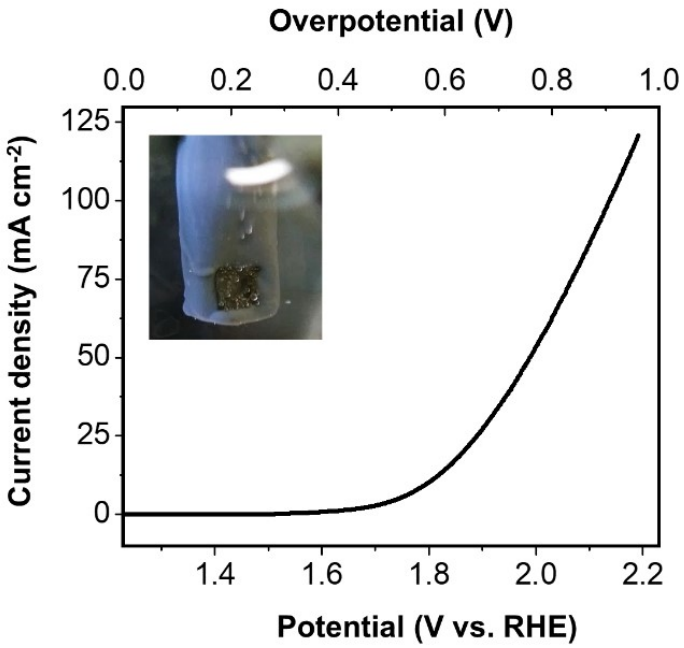


Figure 4.3: LSV of DC $TiB_2$ electrocatalyst in 1.0 M $HClO_4$. Inset of $TiB_2$/FTO electrode operated at $j$ = 10 mA·cm$^{-2}$.

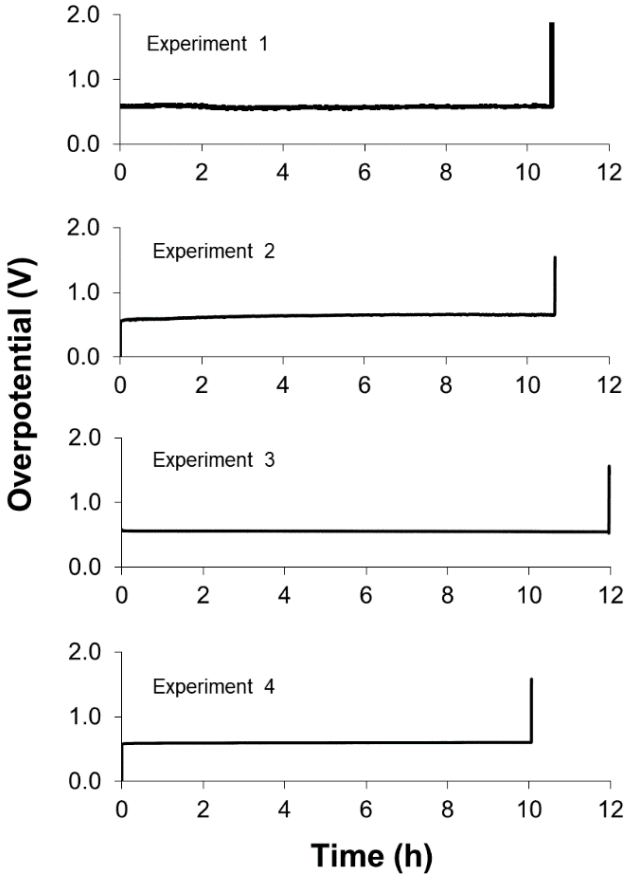


Figure 4.4: CP experiments for DC $TiB_2$ electrodes operated at $j$ = 10 mA·cm$^{-2}$ in 1.0 M $HClO_4$.

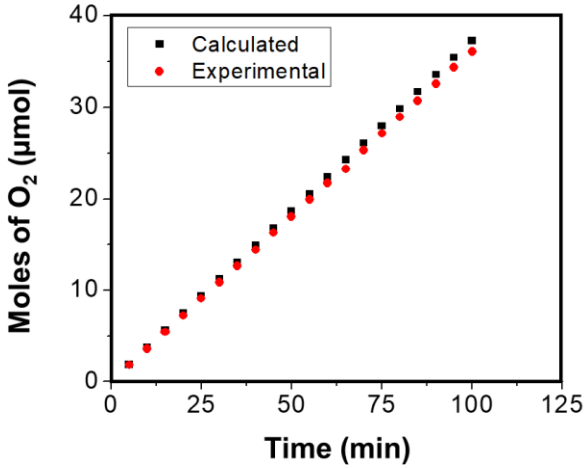


Figure 4.5: F.E. measurements of DC $TiB_2$ electrocatalyst for OER in 1.0 M $HClO_4$ at $j$ = 10 mA·cm$^{-2}$.

The catalyst films on FTO substrates were found to delaminate after 10-12 h of catalysis, as evidenced by the sudden rise in η (Figure 4.4) during CP measurements. The cause for the delamination is currently unclear, but it is hypothesized to be due to mechanical instability caused by poor adhesion of the $TiB_2$ onto the FTO substrate, which is further aggravated by bubble accumulation at the interface of drop-cast $TiB_2$/FTO substrate. Similar behaviour was observed by T-ED $IrO_x$ films in 1.0 M $HClO_4$, which also exhibit a layered structure (Figure 3.1, Figure 3.5). In the absence of Nafion, the catalyst adhesion was poor, and delamination occurred within the first hour of the chronopotentiometry experiments.

$TiB_2$ films were generated by sputtering onto the FTO substrates in an attempt to produce a film with superior adhesion than that generated by drop casting a powder suspension. However, the sputtered films were observed to be more susceptible to faster delamination than the drop cast films and exhibited inferior electrocatalytic performance. It is possible that the absence of Nafion in the sputtered films further deteriorates the connectivity between $TiB_2$ and FTO substrate, thereby masking film activity. Annealing sputtered $TiB_2$ films under inert atmosphere prior to electrolysis could potentially improve film adherence, however Nafion-free DC films were observed to delaminate faster than non-annealed films. An inverted burette setup was used to collect and quantify the amount of evolved oxygen during water oxidation. Prior to catalyst delamination, F.E. was determined to be >96% towards the OER (Figure 4.5). The rest of the current (< 4%) results from the partial oxidation of $TiB_2$, as determined using XPS technique (vide infra).

$HClO_4$ solution was initially used as the electrolyte, as previous studies have demonstrated it to have better oxidative stability compared to $H_2SO_4$.[130,173] However, many published OER materials are studied in $H_2SO_4$, so the OER performance of $TiB_2$ electrodes was also explored in 1.0 M $H_2SO_4$ for comparisons sake. The η appears to increase gradually with time until ~8 h operation after which a more rapid loss of activity is observed (Figure 4.6A). A decreased F.E. of ~84% was observed in 1.0 M $H_2SO_4$ solution (Figure 4.6B) compared to 1.0 M $HClO_4$. This is likely due to higher degradation of the catalyst and lower oxidative stability of $H_2SO_4$ electrolyte. The gradual increase in η compared to the abrupt deactivation observed in $HClO_4$ suggests a more gradual film exfoliation. Comparable behaviour was observed for DC and T-ED $IrO_x$ films in 1.0 M $H_2SO_4$ (Figure 3.4B, 3.6). The adsorption of $HSO_4^-$ appears to reduce the tendency for rapid film delamination, the likely source of abrupt deactivation in $HClO_4$. It could be that the adsorbed $HSO_4^-$ anions act like an ionic adhesive, whereby interactions between oxidized surface groups (e.g., oxidized anions and/or OER intermediates), internal Ti/B sites and/or the support surface helps “glue” the film together and to the support. In-situ studies are required to understand the stability behaviour of films in the two acid types.

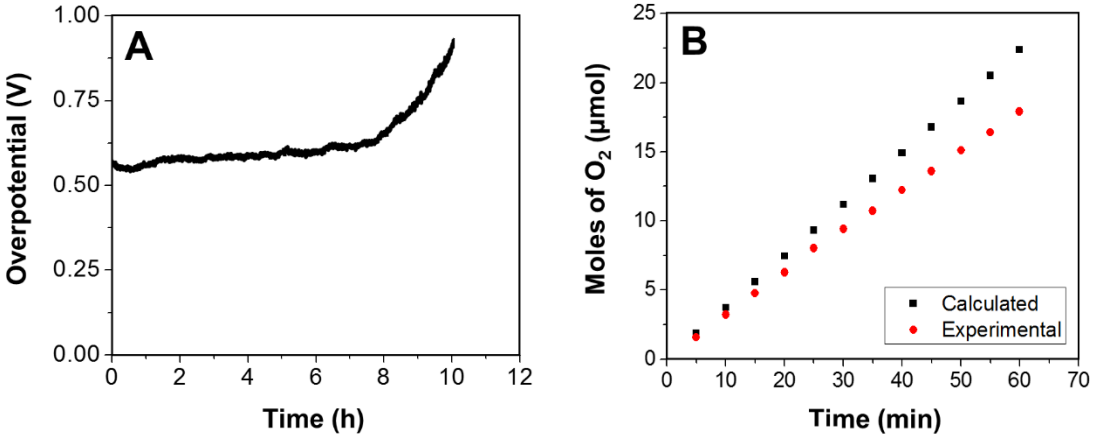


Figure 4.6: (A) CP measurement at $j$ = 10 mA·cm$^{-2}$ and, (B) F.E. measurement for OER for DC $TiB_2$ electrocatalyst in 1.0 M $H_2SO_4$.

To quantify the catalyst stability and dissolution process, ICP-OES measurements were performed on 1.0 M $HClO_4$ electrolyte solution every hour of catalysis. When operated at $j$ = 10 mA · cm$^{-2}$, a dissolution rate of 0.24 µg · cm$^{-2}$ · h$^{-1}$ was observed for Ti (Figure 4.7). After 10 h only ~1.2 % of the catalyst was dissolved, which is the lowest corrosion rate reported to date for an Earth-abundant OER catalyst at pH 0.[96,99,100] This suggests that performance loss is due to mechanical adhesion and not rapid catalyst dissolution.

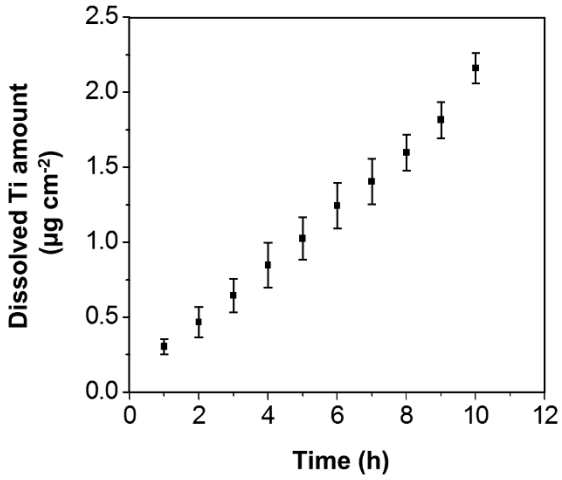


Figure 4.7: Dissolution rate of $TiB_2$ in 1.0 M $HClO_4$ during OER using $j$ = 10 mA · cm$^{-2}$.

XPS measurements were performed at various time intervals on $TiB_2$ electrodes operated at $j$ = 10 $mA \cdot cm^{-2}$ to investigate the chemical evolution of the catalyst surface over time. The high-resolution XP spectrum of the B 1s region (Figure 4.8) prior to OER shows peaks at 187.6 and 192.9 eV, corresponding to $TiB_2$ and $B_2O_3$ respectively.[174] With increasing reaction times the peak intensity at 189.5 eV increases, which can be assigned to growing amounts of $TiBO_x$.[175] An increase in the amount of $B_2O_3$ is also observed over time, which correlates with the area under the purple curve rising in B 1s spectra. High resolution XP spectra of the Ti 2p region (Figure 4.8) prior to the OER shows the presence of $2p_{3/2}$ peaks at 454.6 and 459.0 eV, corresponding to $TiB_2$ and $TiO_2$ respectively.[176] With increasing reaction times, a new peak evolves ca. ~458.2 eV which can be assigned to $2p_{3/2}$ of $TiBO_x$.

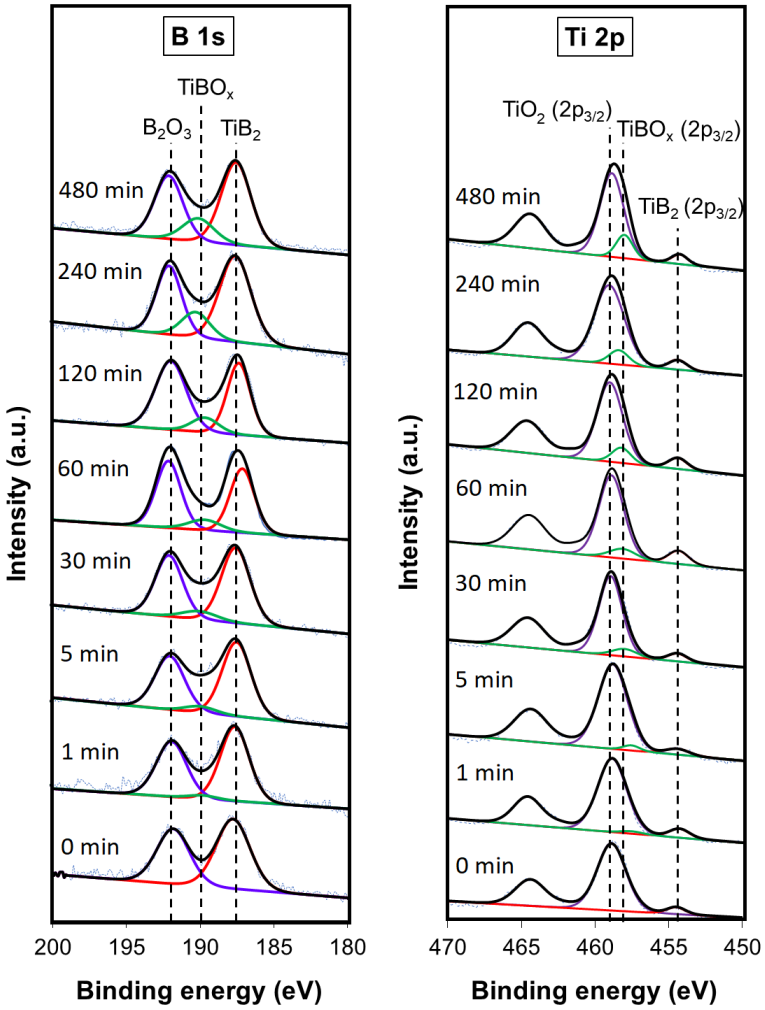


Figure 4.8: Fitted high resolution XP spectra of $TiB_2$ electrodes in the B 1s and Ti 2p regions after various durations of performing OER in 1.0 M $HClO_4$ at $j$ = 10 mA·cm$^{-2}$. For clarity, only $2p_{3/2}$ fitted peaks are shown in Ti 2p spectra (---- : collected data; ━ : fitted data).

The XPS analysis indicates partial oxidation of $TiB_2$ under the operating conditions specified; however, underlying $TiB_2$ can still be observed in both the B 1s and Ti 2p regions after 8 h of catalysis, which indicates a slow rate of oxidation. The survey XP spectrum (Figure 4.9) showed identical elemental composition before and after 8 h of OER. SEM analysis of $TiB_2$ electrodes (Figure 4.10) at various time intervals showed the gradual exfoliation of the catalyst surface. The surface of the film became roughened

within 5 min of OER onset, however there were still visible layers of film that exhibited little-to-no signs of exfoliation. Only smaller film particles are observed after 30 min OER, potentially due to strain from formation and escape of $O_2$ from deeper within the lattice. When the surface of constituent film particles gets exfoliated, previously inaccessible layers become exposed to electrolyte. This contributes to the continual roughening of the film surface and formation of smaller structural features. While the film shows persistent roughening over the course of the experiment, the most damage, or largest morphological change appears to have occurred with 5-30 min of OER.

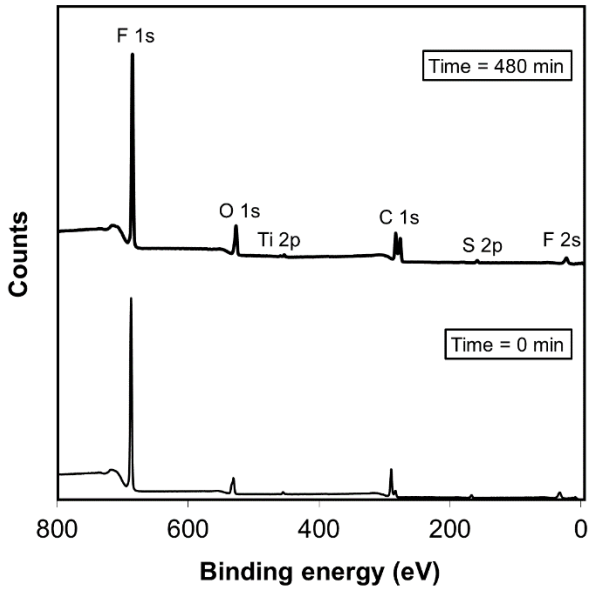


Figure 4.9: Survey XP spectra of DC $TiB_2$ on FTO electrodes before and after 8 h OER at $j$ = 10 mA·cm$^{-2}$ in 1.0 M $HClO_4$.

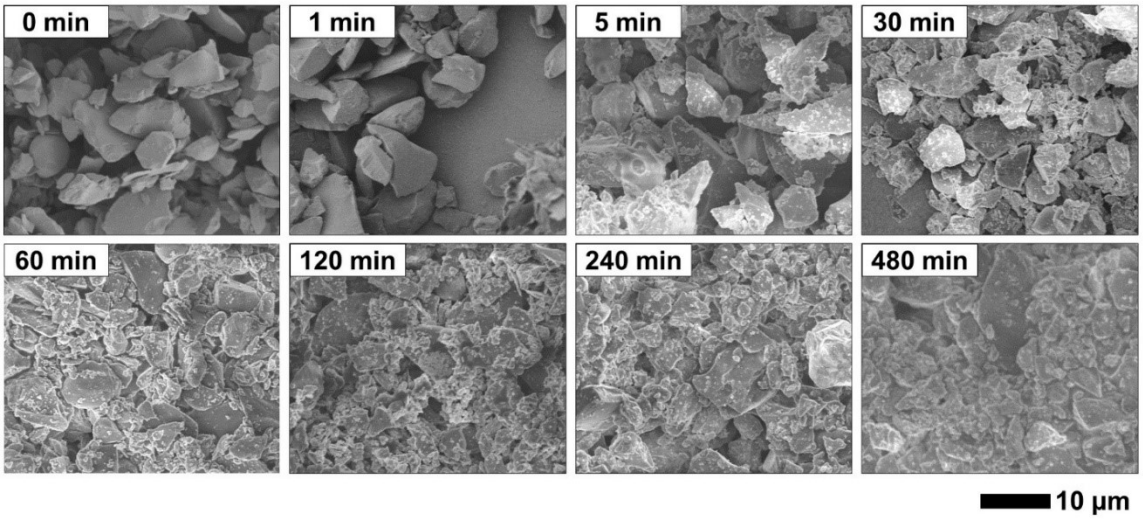


Figure 4.10: SEM images of the $TiB_2$/FTO electrodes after various durations of performing OER in 1.0 M $HClO_4$ at $j$ = 10 mA·cm$^{-2}$.

The electrocatalytic performance and robustness of the $TiB_2$ material reported in this work compare well to other Earth-abundant materials explored as OER electrocatalysts in acidic media. Previously, polycrystalline $Ni_2Ta$ tested in 0.50 M $H_2SO_4$ required an overpotential of 570 mV to generate $j$ = 10 mA · cm$^{-2}$, with a Ni corrosion rate of 0.393 µg · min$^{-1}$.[96] A Ba-based polyoxometalate material required only 361 mV overpotential to generate $j$ = 10 mA · cm$^{-2}$ in 1.0 M $H_2SO_4$, but was unstable over an extended period of time.[99] Ti-stabilized $MnO_2$ was explored in 0.05 M $H_2SO_4$ but was not demonstrated to reach $j$ = 10 mA · cm$^{-2}$.[164] F-doped $Cu_{1.5}Mn_{1.5}O_4$ tested in 0.50 M $H_2SO_4$ was shown to require ~355 mV to generate $j$ = 10 mA · cm$^{-2}$; however long-term stability at that current density was not explored.[163] $Co_3O_4$ films on FTO required 570 mV overpotential to generate $j$ = 10 mA · cm$^{-2}$ in 0.50 M $H_2SO_4$, and a corrosion rate of 100 ng · min$^{-1}$ was observed for Co metal.[97] In-situ deposited $CoFePbO_x$ films operated in 1.0 M $H_2SO_4$ required ~700 mV η to generate $j$ = 10 mA · cm but complimentary

electrolyte analysis was not performed.[95] Mixed-metal oxide $Ni_{0.5}Mn_{0.5}Sb_{1.7}O_y$ was explored in 1.0 M $H_2SO_4$ and required 735 mV overpotential to generate $j$ = 10 $mA \cdot cm^{-2}$.[100] 56% of the initial Mn was found to have leached after 144 h while operating at $j$ = 10 $mA \cdot cm^{-2}$. Acid-stable nanostructured $TiB_2$ coatings and nanopowders with pseudo-spherical shape morphology and particle size of ~500 nm have been reported previously,[177,178] however such materials have not previously been investigated under OER conditions. This study shows the promise of $TiB_2$ as a potential electrocatalyst for OER in acid upon improvement of its mechanical stability.

## 4.4 Conclusions

In summary, $TiB_2$ on FTO was demonstrated to be an effective EA electrocatalyst for OER in 1.0 M $HClO_4$. An η of 560 ± 20 mV was required to drive a current density of 10 $mA \cdot cm^{-2}$ and OER was achieved with a F.E. of > 96%. The catalyst suffered reduced activity, stability and F.E. in 1.0 M $H_2SO_4$. The $TiB_2$ on FTO system failed after > 10 h due to poor mechanical adhesion of the $TiB_2$ film to the FTO. Drop-cast $TiB_2$ films exhibited remarkable chemical stability with a dissolution rate of 0.24 $\mu g \cdot cm^{-2} \cdot h^{-1}$, which is the lowest rate observed to date for an inexpensive catalyst in 1.0 M acid solution. Given the infancy of the field there are very few examples of OER electrocatalysts that do not contain precious metals, and of those known Earth-abundant materials none demonstrate a similar combination of overpotential and dissolution rate.

# Chapter 5. Conclusions and Future Work

## 5.1 Conclusions

The results included in this thesis emphasize the complexities of characterizing and comparing electrocatalyst performances. Both film fabrication and electrolyte conditions can have major implications on the observed physical characteristics and electrochemical behaviour of a material. In the case of $IrO_x$, sweeping statements about the material activity and stability undermine the true variation in performance exhibited by the material. Further, while many reports mention the variability of $IrO_x$ systems and performances, and comment on fabrication-dependent properties of $IrO_x$ films, few studies have attempted to compare different systems under equivalent conditions. Further, there appear to be no studies that compare the effects of electrolyte species and molarity on the measured OER performance of $IrO_x$ films. Thus, the findings presented in Chapter 3 provide a catalogue of responses exhibited by common $IrO_x$ film types under various electrolyte conditions. This will hopefully aid in the comparison and appreciation of literature electrocatalyst systems and provide a point of reference for both $IrO_x$ benchmarks, as well as novel catalyst systems.

Until recently, all known EA materials for acidic OER were found to possess high levels of dissolution and/or prohibitive energy requirements. In this report, $TiB_2$ was found to exhibit moderate activity but high chemical stability relative to other EA OER catalysts. Optimization of film fabrication conditions may allow for improved

mechanically stability and overall applicability in OER research and hydrogen technology.

Interestingly, similar electrochemical stability behaviour was observed for $TiB_2$ and $IrO_x$, particularly DC and T-ED films. T-ED $IrO_x$ films showed a tendency to fail abruptly in 1.0 M $HClO_4$ and more gradually in 1.0 M $H_2SO_4$, with an equivalent trend being observed for DC $TiB_2$ films. Both systems had layered morphologies which likely made them susceptible to delamination and exfoliation mechanisms. The abrupt versus gradual deactivation mechanism observed between electrolyte species is indicative of the tendency of the acid anion to interact directly with the film surface. It also highlights the applicability of the $IrO_x$ performance catalogue built in Chapter 3.

Finally, the outcomes of the research presented in this report emphasize the importance of the film-support interface. Fabrication methods that result in strong film contact generally showed improve mechanical stability. These also tended to be films formed in-situ with the support substrate, which is not a novel observation. DC films showed poor performance unless high mass loadings were used and showed variable performance due to mass loss and support exposure. The stability limitations inherent to a fabrication technique should be kept in mind when developing and screening OER catalyst materials.

### 5.2 Future Work

Immediate future work includes the completion of compositional analysis for the $IrO_x$ films. XPS analysis of the $IrO_x$ films is currently in progress. Alternative means of

preparing T-ED samples for XRD analysis are being pursued. Cross-sectional SEM images of $IrO_x$ films will be collected, as well as $R_{CT}$ values for SIROF, T-SIROF and TDPS films in 1.0 M $H_2SO_4$. Further ICP-OES studies are being conducted for electrolyte samples to establish dissolution rates for all the film and electrolyte conditions probed. ECSA experiments will be completed for films in 0.10 M, 0.50 M and 1.0 M $HClO_4$.

pH-potential studies should be repeated using inert salts to deconvolute the influence of pH and solution resistance. Such studies would likely reveal fabrication-dependent pH-potential relationships. For T-ED film, the pH-potential shift should be assessed for activated films.

Porosity experiments should be conducted for SIROF, T-SIROF and TDPS films. The porosity of thin films can be assessed through BET analysis or using a quartz crystal microbalance,[179] although the experiments are difficult to perform. Porosity can also be approximated using atomic force microscopy (AFM)[55] or Rutherford backscattering spectroscopy.[70]

A more thorough investigation into the origin of film activity for TDPS and SIROFs should be completed. In addition to in-situ X-ray or AFM studies, the influence of the precursor Ir salt on the performance of TDPS is being investigated. TD films have been shown to be insensitive to the Ir chloride precursor used.[53] Ir acetate (Ir(acac)) precursors are used to prepared TD films that are Cl-free and the resulting films still show high OER activity.[81,127] There does not appear to be studies directly comparing TD films prepared from Cl-containing vs. Cl-free Ir precursors, thus the influence of Cl vs.

Cl-free Ir precursors on the OER performance of TDPS films is being investigated. Physical characterization of the interface formed through the in-situ decomposition of Ir-salt on FTO-glass should be conducted. When TD films prepared on Ti or Si substrates are decomposed at high temperatures (>500 °C), passivating oxide layers form at the film-support interface and hinder OER performance.[37,180] $SnO_2$-based films are oxidatively-stable due to their (IV) oxidation state so the characteristics of the film-support interface for TDPS film decomposed on FTO should be unique.

The transition of SIROF to T-SIROF could be better explored to see if an optimal mix of activity, stability and selectivity can be achieved. Other optimization studies could be performed on SIROFs, including the influence of CV activation and film thickness on OER performance.

Figure 5.1 summarizes a protocol for the thorough investigation of electrocatalytic materials for a single electrolyte condition. The table builds off literature benchmarking procedures for screening the activity and/or stability of HER and OER materials.[41,113,121,181] Exhaustive analysis of materials that exhibit OER activity and/or stability under operational conditions can help guide catalyst design and allow realistic targets to be set for stability, activity and scalability.

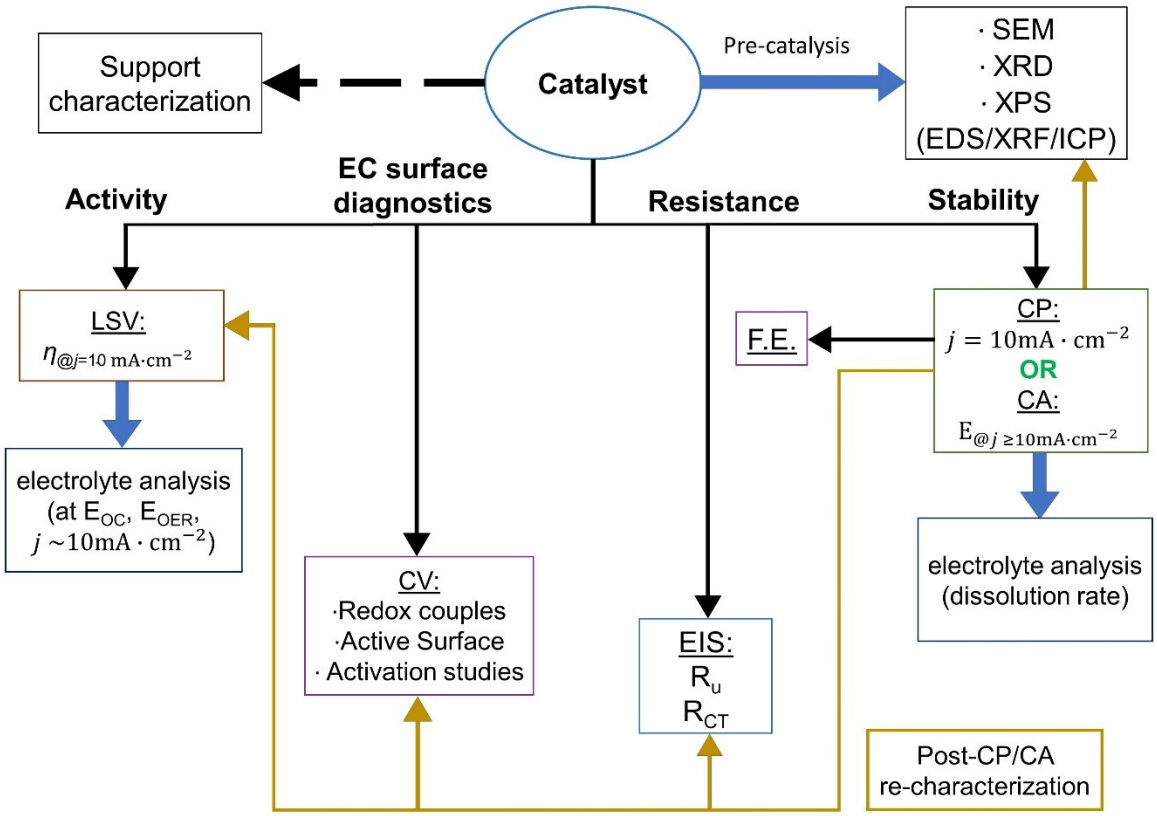


Figure 5.1: Protocol for the comprehensive characterization of OER electrocatalyst activity, stability and deactivation mechanisms.

The corrosion behaviour of films may vary depending on the technique used to study their performance. In the current study, Ir dissolution was probed for $IrO_x$ films following 24 h CP experiments. Cherevko et al. investigated the dissolution profiles of AIROFs and Ir-metal electrodes under potentiodynamic conditions and found rapid corrosion at OER onset but diminished rates at higher potentials.[50,66] Characterizing the electrolyte composition at different potentials for LSV experiments could provide a more complete understanding of the mass loss and deactivation mechanisms acting on films.

ECSA experiment were performed for $IrO_x$ films assuming $C_{DL}$ provided a metric for the active surface area. However, the active surface at OER potentials will be

different than at rest ($E_{OC}$). Further, support substrates can interfere with the measurements and lead to incorrect ECSA values, as can poor film-support contact. Alternative means of active surface area assessment should be explored. ECSA can be measured using EIS rather than CV.[36] There are also techniques for performing BET on thin film samples,[36,179] which would could be used to supplement ECSA studies.

CV characterization of $IrO_x$ films before and after catalysis might reveal changes in redox couples, which can be informative of surface changes and cyclability. Post-catalysis LSV can reveal changes in catalytic efficiencies after prolonged operation. Such experiments have already been performed for some of the $IrO_x$ films and should be performed for the remaining films. The results could be informative of degradation mechanisms.

In the current report, physical characterization was limited to films pre-catalysis. Furthermore, electrochemical characterization of films following 24 h OER (CP) was not included. Post-OER studies on electrodes can provide insight on how surface, composition and catalytic efficiency changes as a result of prolonged catalysis. EIS, LSV and surface area measurements could be repeated following 24 h CP experiments to evaluate the influence of extended OER on the active material. Morphological, structural and compositional changes could also be probed using SEM, XRD, XPS and/or EDS. Depending on the electrode assembly, certain characterization techniques may not be feasible post-electrolysis.

The protocol outline in Figure 5.1 can be extended to other OER catalyst materials. In the case of the group 14 boride films reported in Ch. 4, performing post-

OER characterization after 24 h electrolysis is limited by their mechanical instability and associatively shortened operational time. Reducing the steady-state OER period to within the boride film stability window would allow for post-OER analysis. $TiB_2$ shows the lowest dissolution rate and moderate activity relative to other reported EA acidic-OER catalysts, so thorough characterization may prove insightful. DC $TiB_2$ films are limited in their applicability as electrode materials because of the poor film-support adhesion. A pressed flow-cell was necessary to successfully screen their performance. Alternative means of film preparation to could be explored to optimize the mechanical stability of the material, including electrochemical syntheses or coating support particles with the metal borides. Sputtered $TiB_2$ films might adhere better to a Ti substrate than FTO-glass and show improved performances as a result. Troubleshooting the fabrication method would not only allow better characterization of $TiB_2$ OER performance but also other metal borides and nitrides. Both material families are believed to have attractive electrocatalytic properties. Developing a consistent means of screening their electrochemical properties would not only allow novel classes of materials to be explored but could also afford major improvements in available EA systems for acidic OER.

# REFERENCES


(1) Allen, M. R.; Dube, O. P.; Solecki, W.; Aragon-Durand, F.; Cramer, W.; Humphreys, S.; Kainuma, M.; Kala, J.; Mahowald, N.; Mulugetta, Y.; et al. Framing and Context. In *Global Warming of 1.5°C. An IPCC Special Report on the impacts of global warming of 1.5°C above pre-industrial levels and related global greenhouse gas emission pathways, in the context of strengthening the global response to the threat of climate change,*; Masson-Delmotte, V., Zhai, P., Pörtner, H.-O., Roberts, D., Skea, J., Shukla, P. R., Pirani, A., Moufouma-Okia, W., Péan, C., Pidcock, R., et al., Eds.; Intergovernmental Panel on Climate Change, 2018; pp 49–91.

(2) de Coninck, H.; Revi, A.; Babiker, M.; Bertoldi, P.; Buckeridge, M.; Cartwright, A.; Dong, W.; Ford, J.; Fuss, S.; Hourcade, J.-C.; et al. Strengthening and Implementing the Global Response. In *Global Warming of 1.5°C. An IPCC Special Report on the impacts of global warming of 1.5°C above pre-industrial levels and related global greenhouse gas emission pathways, in the context of strengthening the global response to the threat of climate change,*; Masson-Delmotte, V., Zhai, P., Pörtner, H.-O., Roberts, D., Skea, J., Shukla, P. R., Pirani, A., Moufouma-Okia, W., Péan, C., Pidcock, R., et al., Eds.; Intergovernmental Panel on Climate Change, 2018; pp 313–443.

(3) Jacobs, D. J. The Greenhouse Effect. In *Introduction to Atmospheric Chemistry*; Princeton University Press, 2004.

(4) Dessler, A. E. *Introduction to Modern Climate Change*; Cambridge University Press, 2012.

(5) *Perspectives on Climate Change Action in Canada- A Collaborative Report from Auditors General*; 2018.

(6) Rogelj, J.; Shindell, D.; Jiang, K.; Fifita, S.; Forster, P.; Ginzburg, V.; Handa, C.; Kheshgi, H.; Kobayashi, S.; Kriegler, E.; et al. Mitigation Pathways Compatible with 1.5°C in the Context of Sustainable Development. In *Global Warming of 1.5°C. An IPCC Special Report on the impacts of global warming of 1.5°C above pre-industrial levels and related global greenhouse gas emission pathways, in the context of strengthening the global response to the threat of climate change,*; Masson-Delmotte, V., Zhai, P., Pörtner, H.-O., Roberts, D., Skea, J. ., Shukla, P. R., Pirani, A., Moufouma-Okia, W., Péan, C., Pidcock, R., et al., Eds.; Intergovernmental Panel on Climate Change, 2018; pp 93–174.

(7) UNFCCC. ADOPTION OF THE PARIS AGREEMENT. *Adopt. Paris Agreement. Propos. by Pres.* **2015**, 32. https://doi.org/FCCC/CP/2015/L.9/Rev.1.

(8) UNEP. *The Emissions Gap Report 2018*; 2018.

(9) Cook, T. R.; Dogutan, D. K.; Reece, S. Y.; Surendranath, Y.; Teets, T. S.; Nocera, D. G. Solar Energy Supply and Storage for the Legacy and Nonlegacy Worlds. *Chem. Rev.* **2010**, *110* (11), 6474–6502. https://doi.org/10.1021/cr100246c.

(10) Rezaei, N.; Ahmadi, A.; Afifi, S. N.; Zobaa, A. F.; Abdel Aleem, S. H. E. Overview of Energy Storage Technology. In *Energy Storage at Different Voltagr Levels- Technology, Integration and Market Aspects*; Zobaa, A. F., Ribeiro, P. F., Abdel Aleem, S. H. E., Afifi, S. N., Eds.; Institution of Engineering and Technology, 2018; pp 1–29.

(11) Gandia, L. M.; Arzamendi, G.; Dieguez, P. M. Overview. In *Renewable Hydrogen Technology*; Elsevier B.V., 2013; pp 1–17.

(12) Nikolaidis, P.; Poullikkas, A. A Comparative Overview of Hydrogen Production Processes. *Renew. Sustain. Energy Rev.* **2017**, *67*, 597–611. https://doi.org/10.1016/j.rser.2016.09.044.

(13) Abbott, D. Keeping the Energy Debate Clean: How Do We Supply the World's Energy Needs? *Proc. IEEE* **2010**, *98* (1), 42–66. https://doi.org/10.1109/JPROC.2009.2035162.

(14) Hussain, A.; Arif, S. M.; Aslam, M. Emerging Renewable and Sustainable Energy Technologies: State of the Art. *Renew. Sustain. Energy Rev.* **2017**, *71*, 12–28. https://doi.org/10.1016/j.rser.2016.12.033.

(15) Department of Energy. *Renewable Energy : An Overview*; 2001.

(16) McKone, J. R.; Lewis, N. S.; Gray, H. B. Will Solar-Driven Water-Splitting Devices See the Light of Day? *Chem. Mater.* **2014**, *26* (1), 407–414. https://doi.org/10.1021/cm4021518.

(17) Lewis, N. S.; Nocera, D. G. Powering the Plant: Chemica Challenges in Solar Energy Utilization. *PNAS* **2007**, *103* (43), 15729–15735.

(18) Dincer, I.; Zamfirescu, C. Hydrogen and Its Production. In *Sustainable Hydrogen Production*; Elsevier Inc., 2017; pp 65–97.

(19) Guo, X.; Du, H.; Qu, F.; Li, J. Recent Progress in Electrocatalytic Nitrogen Reduction. *J. Mater. Chem. A* **2019**, *7* (8), 3531–3543. https://doi.org/10.1039/c8ta11201k.

(20) Millet, P.; Grigoriev, S. Water Electrolysis Technologies. In *Renewable Hydrogen Technology*; Elsevier B.V., 2013; pp 19–40.

(21) Naimi, Y.; Antar, A. *Hydrogen Generation by Water Electrolysis*; IntechOpen, 2018.

(22) Cui, X.; Tang, C.; Zhang, Q. A Review of Electrocatalytic Reduction of Dinitrogen to Ammonia under Ambient Conditions. *Adv Energy Mater* **2018**, *8*. https://doi.org/10.1002/aenm.201800369.

(23) Lewis, N. S. Research Opportunities to Advance Solar Energy Utilization. *Science (80-. ).* **2016**, *351* (6271), 353. https://doi.org/10.1126/science.aad1920.22.

(24) Hunter, B. M.; Gray, H. B.; Müller, A. M. Earth-Abundant Heterogeneous Water Oxidation Catalysts. *Chem. Rev.* **2016**, *116* (22), 14120–14136. https://doi.org/10.1021/acs.chemrev.6b00398.

(25) Suen, N. T.; Hung, S. F.; Quan, Q.; Zhang, N.; Xu, Y. J.; Chen, H. M. Electrocatalysis for the Oxygen Evolution Reaction: Recent Development and Future Perspectives. *Chem. Soc. Rev.* **2017**, *46* (2), 337–365. https://doi.org/10.1039/c6cs00328a.

(26) Schalenbach, M.; Zeradjanin, A. R.; Kasian, O.; Cherevko, S.; Mayrhofer, K. J. J. A Perspective on Low-Temperature Water Electrolysis - Challenges in Alkaline and Acidic Technology. *Int. J. Electrochem. Sci.* **2018**, *13* (2), 1173–1226. https://doi.org/10.20964/2018.02.26.

(27) Tahir, M.; Pan, L.; Idrees, F.; Zhang, X.; Wang, L.; Zou, J. J.; Wang, Z. L. Electrocatalytic Oxygen Evolution Reaction for Energy Conversion and Storage: A Comprehensive Review. *Nano Energy* **2017**, *37*, 136–157. https://doi.org/10.1016/j.nanoen.2017.05.022.

(28) Pourbaix, M. *Atlas of Electrochemical Equilibria in Aqueous Solutions*; Pergamon Press Ltd, 1974.

(29) Bard, A. J.; Faulkner, L. R. *Electrochemical Methods- Fundamentals and Applications*, 2nd ed.; John Wiley & Sons, Inc., 2001.

(30) Tester, J. W.; Drake, E. M.; Driscoll, M. J.; Golay, M. W.; Peters, W. A. Energy Management. In *Sustainable Energy: Choosing Among Options*; MIT Press, 2012; pp 800–862.

(31) Reier, T.; Nong, H. N.; Teschner, D.; Schlögl, R.; Strasser, P. Electrocatalytic Oxygen Evolution Reaction in Acidic Environments – Reaction Mechanisms and Catalysts. *Adv. Energy Mater.* **2017**, *7* (1). https://doi.org/10.1002/aenm.201601275.

(32) Carmo, M.; Fritz, D. L.; Mergel, J.; Stolten, D. A Comprehensive Review on PEM Water Electrolysis. *Int. J. Hydrogen Energy* **2013**, *38* (12), 4901–4934. https://doi.org/10.1016/j.ijhydene.2013.01.151.

(33) Jiao, Y.; Zheng, Y.; Jaroniec, M.; Qiao, S. Z. Design of Electrocatalysts for Oxygen- and Hydrogen-Involving Energy Conversion Reactions. *Chem. Soc. Rev.* **2015**, *44* (8), 2060–2086. https://doi.org/10.1039/c4cs00470a.

(34) Qi, J.; Zhang, W.; Cao, R. Solar-to-Hydrogen Energy Conversion Based on Water Splitting. *Adv. Energy Mater.* **2018**, *8* (5), 1–16. https://doi.org/10.1002/aenm.201701620.

(35) Saha, S.; Kishor, K.; Sivakumar, S.; Pala, R. G. S. Models and Mechanisms of

Oxygen Evolution Reaction on Electrocatalytic Surface. *J. Indian Inst. Sci.* **2016**, *96*, 325–349.

(36) Anantharaj, S.; Ede, S. R.; Sakthikumar, K.; Karthick, K.; Mishra, S.; Kundu, S. Recent Trends and Perspectives in Electrochemical Water Splitting with an Emphasis on Sulfide, Selenide, and Phosphide Catalysts of Fe, Co, and Ni: A Review. *ACS Catal.* **2016**, *6* (12), 8069–8097. https://doi.org/10.1021/acscatal.6b02479.

(37) Reier, T.; Teschner, D.; Lunkenbein, T.; Bergmann, A.; Selve, S.; Kraehnert, R.; Schlögl, R.; Strasser, P. Electrocatalytic Oxygen Evolution on Iridium Oxide: Uncovering Catalyst-Substrate Interactions and Active Iridium Oxide Species. *J. Electrochem. Soc.* **2014**, *161* (9), F876–F882. https://doi.org/10.1149/2.0411409jes.

(38) Cheng, Y.; Jiang, S. P. Advances in Electrocatalysts for Oxygen Evolution Reaction of Water Electrolysis-from Metal Oxides to Carbon Nanotubes. *Prog. Nat. Sci. Mater. Int.* **2015**, *25* (6), 545–553. https://doi.org/10.1016/j.pnsc.2015.11.008.

(39) Doyle, R. L.; Lyons, M. E. G. The Oxygen Evolution Reaction: Mechanistic Concepts and Catalyst Design. In *Photoelectrochemical solar fuel production*; Springer International Publishing, 2016; pp 41–104.

(40) Roger, I.; Shipman, M. A.; Symes, M. D. Earth-Abundant Catalysts for Electrochemical and Photoelectrochemical Water Splitting. *Nat. Rev. Chem.* **2017**, *1*. https://doi.org/10.1038/s41570-016-0003.

(41) McCrory, C. C. L.; Jung, S.; Ferrer, I. M.; Chatman, S. M.; Peters, J. C.; Jaramillo, T. F. Benchmarking Hydrogen Evolving Reaction and Oxygen Evolving Reaction Electrocatalysts for Solar Water Splitting Devices. *J. Am. Chem. Soc.* **2015**, *137* (13), 4347–4357. https://doi.org/10.1021/ja510442p.

(42) Seh, Z. W.; Kibsgaard, J.; Dickens, C. F.; Chorkendorff, I.; Nørskov, J. K.; Jaramillo, T. F. Combining Theory and Experiment in Electrocatalysis: Insights into Materials Design. *Science (80-. ).* **2017**, *355*. https://doi.org/10.1126/science.aad4998.

(43) McCrory, C. C. L.; Jung, S.; Peters, J. C.; Jaramillo, T. F. Benchmarking Heterogeneous Electrocatalysts for the Oxygen Evolution Reaction. *J. Am. Chem. Soc.* **2013**, *135* (45), 16977–16987. https://doi.org/10.1021/ja407115p.

(44) Hackwood, S.; Schiavone, L. M.; Dautremont-Smith, W. C.; Beni, G. Anodic Evolution of Oxygen on Sputtered Iridium Oxide Films. *J. Electrochem. Soc.* **1981**, *128* (12), 2569–2573. https://doi.org/10.1149/1.2127293.

(45) Seitz, L. C.; Dickens, C. F.; Nishio, K.; Hikita, Y.; Montoya, J.; Doyle, A.; Kirk, C.; Vojvodic, A.; Hwang, H. Y.; Norskov, J. K.; et al. A Highly Active and Stable IrOx/SrIrO3 Catalyst for the Oxygen Evolution Reaction. *Science (80-. ).* **2016**, *353*, 1011–1014. https://doi.org/10.1039/C5TA09322H.

(46) Danilovic, N.; Subbaraman, R.; Chang, K. C.; Chang, S. H.; Kang, Y. J.; Snyder, J.; Paulikas, A. P.; Strmcnik, D.; Kim, Y. T.; Myers, D.; et al. Activity-Stability Trends for the Oxygen Evolution Reaction on Monometallic Oxides in Acidic Environments. *J. Phys. Chem. Lett.* **2014**, *5* (14), 2474–2478. https://doi.org/10.1021/jz501061n.

(47) Savan, A.; Ratna, B.; Merzlikin, S.; Breitbach, B.; Ludwig, A.; Mayrhofer, K. J. J. J.; Cherevko, S.; Geiger, S.; Kasian, O.; Kulyk, N.; et al. Oxygen and Hydrogen Evolution Reactions on Ru, $RuO_2$, Ir, and $IrO_2$ Thin Film Electrodes in Acidic and Alkaline Electrolytes: A Comparative Study on Activity and Stability. *Catal. Today* **2016**, *262*, 170–180. https://doi.org/10.1016/j.cattod.2015.08.014.

(48) Pauporte, T.; Andolfatto, F.; Durand, R. Some Electrocatalytic Properties of Anodic Iridium Oxide Nanoparticles in Acidic Solution. *Electrochim. Acta* **1999**, *45* (3), 431–439. https://doi.org/10.1016/S0013-4686(99)00282-0.

(49) Vukovic, M. Oxygen Evolution Reaction on Thermally Treated Iridium Oxide Films. *J. Appl. Electrochem.* **1987**, *17*, 737–745.

(50) Cherevko, S.; Geiger, S.; Kasian, O.; Mingers, A.; Mayrhofer, K. J. J. Oxygen Evolution Activity and Stability of Iridium in Acidic Media. Part 1. - Metallic Iridium. *J. Electroanal. Chem.* **2016**, *773*, 69–78. https://doi.org/10.1016/j.jelechem.2016.04.033.

(51) Matsumoto, Y.; Tazawa, T.; Muroi, N.; Sato, E. I. New Types of Anodes for the Oxygen Evolution Reaction in Acidic Solution. *J. Electrochem. Soc.* **1986**, *133* (11), 2257–2262. https://doi.org/10.1149/1.2108389.

(52) Audichon, T.; Napporn, T. W.; Canaff, C.; Morais, C.; Comminges, C.; Kokoh, K. B. IrO2 Coated on RuO2 as Efficient and Stable Electroactive Nanocatalysts for Electrochemical Water Splitting. *J. Phys. Chem. C* **2016**, *120* (5), 2562–2573. https://doi.org/10.1021/acs.jpcc.5b11868.

(53) De Oliveira-Sousa, A.; Da Silva, M. A. S.; MacHado, S. A. S.; Avaca, L. A.; De Lima-Neto, P. Influence of the Preparation Method on the Morphological and Electrochemical Properties of Ti/IrO2-Coated Electrodes. *Electrochim. Acta* **2000**, *45* (27), 4467–4473. https://doi.org/10.1016/S0013-4686(00)00508-9.

(54) Reier, T.; Weidinger, I.; Hildebrandt, P.; Kraehnert, R.; Strasser, P. Electrocatalytic Oxygen Evolution Reaction on Iridium Oxide Model Film Catalysts: Influence of Oxide Type and Catalyst Substrate Interactions. *ECS Trans.* **2013**, *58* (2), 39–51. https://doi.org/10.1149/05802.0039ecst.

(55) Slavcheva, E.; Schnakenberg, U.; Mokwa, W. Deposition of Sputtered Iridium Oxide-Influence of Oxygen Flow in the Reactor on the Film Properties. *Appl. Surf. Sci.* **2006**, *253* (4), 1964–1969. https://doi.org/10.1016/j.apsusc.2006.03.073.

(56) Ouattara, L.; Fierro, S.; Frey, O.; Koudelka, M.; Comninellis, C. Electrochemical Comparison of IrO2 Prepared by Anodic Oxidation of Pure Iridium and IrO2 Prepared by Thermal Decomposition of H2IrCl6 Precursor Solution. *J. Appl.*

*Electrochem.* **2009**, *39* (8), 1361–1367. https://doi.org/10.1007/s10800-009-9809-2.

(57) Fierro, S.; Kapałka, A.; Comninellis, C. Electrochemical Comparison between IrO2 Prepared by Thermal Treatment of Iridium Metal and IrO2 Prepared by Thermal Decomposition of H2IrCl6 Solution. *Electrochem. commun.* **2010**, *12* (1), 172–174. https://doi.org/10.1016/j.elecom.2009.11.018.

(58) Huang, C. A.; Yang, S. W.; Lai, P. L. Effect of Precursor Baking on the Electrochemical Properties of IrO2-Ta2O5/Ti Anodes. *Surf. Coatings Technol.* **2018**, *350*, 896–903. https://doi.org/10.1016/j.surfcoat.2018.03.095.

(59) Ortel, E.; Reier, T.; Strasser, P.; Kraehnert, R. Mesoporous IrO 2 Films Templated by PEO-PB-PEO Block-Copolymers : Self-Assembly , Crystallization Behavior , and Electrocatalytic Performance. *Chem. Mater.* **2011**, *23*, 3201–3209. https://doi.org/10.1021/cm200761f.

(60) Spurgeon, J. M.; Velazquez, J. M.; McDowell, M. T. Improving O2 Production of WO3 Photoanodes with IrO2 in Acidic Aqueous Electrolyte. *Phys. Chem. Chem. Phys.* **2014**, *16* (8), 3623–3631. https://doi.org/10.1039/c3cp55527e.

(61) Spöri, C.; Kwan, J. T. H.; Bonakdarpour, A.; Wilkinson, D. P.; Strasser, P. The Stability Challenges of Oxygen Evolving Catalysts: Towards a Common Fundamental Understanding and Mitigation of Catalyst Degradation. *Angew. Chemie - Int. Ed.* **2017**, *56* (22), 5994–6021. https://doi.org/10.1002/anie.201608601.

(62) Geiger, S.; Kasian, O.; Shrestha, B. R.; Mingers, A. M.; Mayrhofer, K. J. J.; Cherevko, S. Activity and Stability of Electrochemically and Thermally Treated Iridium for the Oxygen Evolution Reaction. *J. Electrochem. Soc.* **2016**, *163* (11), F3132–F3138. https://doi.org/10.1149/2.0181611jes.

(63) Gottesfeld, S.; McIntyre, J. D. E. Electrochromism in Anodic Iridium Oxide Films. II. PH Effects on Corrosion Stability and the Mechanism of Coloration and Bleaching. *Appl. Phys. Lett.* **1978**, *33* (2), 208–210. https://doi.org/10.1063/1.90277.

(64) Conway, B. E.; Mozota, J. Surface and Bulk Processes at Oxidized Ir Electrodes-II Conductivity Switched Behaviour of Thick Oxide Films. *Electrochim. Acta.* **1983**, *28*, 9–16.

(65) Bock, C.; Birss, V. I. Factors Influencing the Stability and Kinetics of Hydrous Ir Oxide Films. *J. Electrochem. Soc.* **1997**, *19*, 194–205.

(66) Cherevko, S.; Geiger, S.; Kasian, O.; Mingers, A.; Mayrhofer, K. J. J. Oxygen Evolution Activity and Stability of Iridium in Acidic Media. Part 2. – Electrochemically Grown Hydrous Iridium Oxide. *J. Electroanal. Chem.* **2016**, *774*, 102–110. https://doi.org/10.1016/j.jelechem.2016.05.015.

(67) Rand, D. A. J.; Woods, R. Cyclic Voltammetry Studies on Iridium Electrodes in

Sulphuric Acid Solutions. *Electroanal. Chem. Interfacial Electrochem.* **1974**, *55*, 375.

(68) Pickup, P. G.; Birss, V. I. A Model for Anodic Hydrous Oxide Growth at Iridium. *J. Electroanal. Chem.* **1987**, *220*, 83–100.

(69) Birss, V.; Myers, R.; Conway, B. E. Electron Microscopy Study of Formation of Thick Oxide Films on Ir and Ru Electrodes. **1984**, *12* (24), 1502–1510.

(70) Wen, R. T.; Niklasson, G. A.; Granqvist, C. G. Electrochromic Iridium Oxide Films: Compatibility with Propionic Acid, Potassium Hydroxide, and Lithium Perchlorate in Propylene Carbonate. *Sol. Energy Mater. Sol. Cells* **2014**, *120(A)*, 151–156.

(71) Zhang, H.; Pei, W. H.; Zhao, S. S.; Yang, X. W.; Liu, R. C.; Liu, Y. Y.; Wu, X.; Guo, D. M.; Gui, Q.; Guo, X. H.; et al. Fabrication of Iridium Oxide Neural Electrodes at the Wafer Level. *Sci. China Technol. Sci.* **2016**, *59* (9), 1399–1406. https://doi.org/10.1007/s11431-016-6099-x.

(72) Hackwood, S.; Dayem, A. H.; Beni, G. Amorphous-Nonmetal to Cyrstalline Metal Transition in Electrochromic Iridium Oxide Films. *Phys. Rev. B.* **1982**, *25* (2), 471–478.

(73) Sanjinés, R.; Aruchamy, A.; Lévy, F. Thermal Stability of Sputtered Iridium Oxide Films. *J. Electrochem. Soc.* **2006**, *136* (6), 1740–1743. https://doi.org/10.1149/1.2097002.

(74) Slavcheva, E.; Radev, I.; Bliznakov, S.; Topalov, G.; Andreev, P.; Budevski, E. Sputtered Iridium Oxide Films as Electrocatalysts for Water Splitting via PEM Electrolysis. *Electrochim. Acta* **2007**, *52* (12), 3889–3894. https://doi.org/10.1016/j.electacta.2006.11.005.

(75) Hackwood, S.; Beni, G. Phase Transitions in Iridium Oxide Films. *Solid State Ionics* **1981**, *2*, 297–299.

(76) Cruz, A.; Abad, L.; Carretero, N. M.; Moral-Vico, J.; Fraxedas, J.; Lozano, P.; Subias, G.; Padial, V.; Carballo, M.; Collazos-Castro, J. E.; et al. Iridium Oxohydroxide , a Significant Member in the Family of Iridium Oxides . Iridium Oxohydroxide , a Significant Member in the Family of Iridium Oxides . Stoichiometry , Characterization , and Implications in Bioelectrodes. *J. Phys. Chem. C.* **2012**, *116*, 5155–5168. https://doi.org/10.1021/jp212275q.

(77) Zhao, Y.; Hernandez-Pagan, E. A.; Vargas-Barbosa, N. M.; Dysart, J. L.; Mallouk, T. E. A High Yield Synthesis of Ligand-Free Iridium Oxide Nanoparticles with High Electrocatalytic Activity. *J. Phys. Chem. Lett.* **2011**, *2* (5), 402–406. https://doi.org/10.1021/jz200051c.

(78) Zhao, Y.; Vargas-Barbosa, N. M.; Hernandez-Pagan, E. A.; Mallouk, T. E. Anodic Deposition of Colloidal Iridium Oxide Thin Films from Hexahydroxyiridate(IV) Solutions. *Small* **2011**, *7* (14), 2087–2093.

https://doi.org/10.1002/smll.201100485.

(79) Petit, M. A.; Plichon, V. Anodic Electrodeposition of Iridium Oxide Films. *J Electroanal Chem* **1998**, *444*, 247–252.

(80) Yamanaka, K. Anodically Electrodeposited Iridium Oxide Films (AEIROF) from Alkaline Solutions for Electrochromic Display Devices. *Jpn. J. Appl. Phys.* **1989**, *28* (4), 632–637. https://doi.org/10.1143/JJAP.28.632.

(81) Abbott, D. F.; Lebedev, D.; Waltar, K.; Povia, M.; Nachtegaal, M.; Fabbri, E.; Copéret, C.; Schmidt, T. J. Iridium Oxide for the Oxygen Evolution Reaction: Correlation between Particle Size, Morphology, and the Surface Hydroxo Layer from Operando XAS. *Chem. Mater.* **2016**, *28* (18), 6591–6604. https://doi.org/10.1021/acs.chemmater.6b02625.

(82) Katsounaros, I.; Cherevko, S.; Zeradjanin, A. R.; Mayrhofer, K. J. J. Oxygen Electrochemistry as a Cornerstone for Sustainable Energy Conversion. *Angew. Chemie - Int. Ed.* **2014**, *53* (1), 102–121. https://doi.org/10.1002/anie.201306588.

(83) Li, G.; Li, S.; Xiao, M.; Ge, J.; Liu, C.; Xing, W. Nanoporous IrO2 Catalyst with Enhanced Activity and Durability for Water Oxidation Owing to Its Micro/Mesoporous Structure. *Nanoscale* **2017**, *9* (27), 9291–9298. https://doi.org/10.1039/c7nr02899g.

(84) Kong, F. D.; Zhang, S.; Yin, G. P.; Liu, J.; Xu, Z. Q. IrO2-Graphene Hybrid as an Active Oxygen Evolution Catalyst for Water Electrolysis. *Int. J. Hydrogen Energy* **2013**, *38* (22), 9217–9222. https://doi.org/10.1016/j.ijhydene.2013.05.023 Short Communication.

(85) Hu, W.; Wang, Y.; Hu, X.; Zhou, Y.; Chen, S. Three-Dimensional Ordered Macroporous IrO2 as Electrocatalyst for Oxygen Evolution Reaction in Acidic Medium. *J. Mater. Chem.* **2012**, *22* (13), 6010–6016. https://doi.org/10.1039/c2jm16506f.

(86) Feng, M.; Qu, R.; Wei, Z.; Wang, L.; Sun, P.; Wang, Z. Characterization of the Thermolysis Products of Nafion Membrane: A Potential Source of Perfluorinated Compounds in the Environment. *Sci. Rep.* **2015**, *5*, 1–8. https://doi.org/10.1038/srep09859.

(87) Lyons, M. E. G.; Floquet, S. Mechanism of Oxygen Reactions at Porous Oxide Electrodes. Part 2. Oxygen Evolution at Ruthenium Dioxide, Iridium Dioxide and Mixed Ruthenium Iridium Oxide Electrodes in Aqueous Acid and Alkaline Solution. *Phys. Chem. Chem. Phys.* **2011**, *13*, 5314–5335. https://doi.org/10.1039/C0CP02875D.

(88) Xu, L.; Xin, Y.; Wang, J. A Comparative Study on IrO2-Ta2O5 Coated Titanium Electrodes Prepared with Different Methods. *Electrochim. Acta* **2009**, *54* (6), 1820–1825. https://doi.org/10.1016/j.electacta.2008.10.004.

(89) De Pauli, C. P.; Trasatti, S. Electrochemical Surface Characterization of IrO2 +

SnO2 Mixed Oxide Electrocatalysts. *J Electroanal Chem* **1995**, *396*, 161–168.

(90) Trasatti, S. Electrocatalysis in the Anodic Evolution of Oxygen and Chlorine. *Electrochim. Acta* **1984**, *29*, 1503–1512.

(91) Trasatti, S. Physical Electrochemistry of Ceramic Oxides. *Electrochim. Acta* **1991**, *36*, 225–241.

(92) Krýsa, J.; Maixner, J.; Mráz, R.; Roušar, I. Effect of Coating Thickness on the Properties of IrO2-Ta2O5 Anodes. *J. Appl. Electrochem.* **1998**, *28* (3), 369–372. https://doi.org/10.1023/A:1003284204458.

(93) Oakton, E.; Lebedev, D.; Povia, M.; Abbott, D. F.; Fabbri, E.; Fedorov, A.; Nachtegaal, M.; Cope, C.; Schmidt, T. J. IrO2 - TiO2: A High-Surface-Area, Active, and Stable Electrocatalyst for the Oxygen Evolution Reaction. *ACS Catal.* **2017**, *7*, 2346–2352. https://doi.org/10.1021/acscatal.6b03246.

(94) Mohammed-Ibrahim, J.; Xiaoming, S. Recent Progress on Earth Abundant Electrocatalysts for Hydrogen Evolution Reaction (HER) in Alkaline Medium to Achieve Efficient Water Splitting – A Review. *J. Energy Chem.* **2019**, *400* (July), 111–160. https://doi.org/10.1016/j.jechem.2018.09.016.

(95) Chatti, M.; Gardiner, J. L.; Fournier, M.; Johannessen, B.; Williams, T.; Gengenbach, T. R.; Pai, N.; Nguyen, C.; MacFarlane, D. R.; Hocking, R. K.; et al. Intrinsically Stable in Situ Generated Electrocatalyst for Long-Term Oxidation of Acidic Water at up to 80 °C. *Nat. Catal.* **2019**, *2* (5), 457–465. https://doi.org/10.1038/s41929-019-0277-8.

(96) Mondschein, J. S.; Kumar, K.; Holder, C. F.; Seth, K.; Kim, H.; Schaak, R. E. Intermetallic Ni2Ta Electrocatalyst for the Oxygen Evolution Reaction in Highly Acidic Electrolytes. *Inorg. Chem.* **2018**, *57* (10), 6010–6015. https://doi.org/10.1021/acs.inorgchem.8b00503.

(97) Mondschein, J. S.; Callejas, J. F.; Read, C. G.; Chen, J. Y. C.; Holder, C. F.; Badding, C. K.; Schaak, R. E. Crystalline Cobalt Oxide Films for Sustained Electrocatalytic Oxygen Evolution under Strongly Acidic Conditions. *Chem. Mater.* **2017**, *29* (3), 950–957. https://doi.org/10.1021/acs.chemmater.6b02879.

(98) Kirshenbaum, M. J.; Richter, M. H.; Dasog, M. Electrochemical Water Oxidation in Acidic Solution Using Titanium Diboride (TiB2) Catalyst. *ChemCatChem* **2019**. https://doi.org/10.1002/cctc.201801736.

(99) Blasco-Ahicart, M.; Soriano-Lopez, J.; Carbo, J. J.; Poblet, J. M.; Galan-Mascaros, J. R. Polyoxometalate Electrocatalysts Based on Earthabundant Metals for Efficient Water Oxidation in Acidic Media. *Nat. Chem.* **2018**, *10* (1), 24–30. https://doi.org/10.1038/NCHEM.2874.

(100) Moreno-hernandez, I. A.; Macfarland, C. A.; Papadantonakis, K. M.; Brunschwig, B. S.; Read, C. G.; Lewis, N. S. Crystalline Nickel Manganese Antimonate as a Stable Water-Oxidation Catalyst in Aqueous 1.0 M H2SO4. *Energy Environ. Sci.*

**2017**, *10*, 2103–2108. https://doi.org/10.1039/C7EE01486D.

(101) Sichkar, S. M.; Antonov, V. N.; Antropov, V. P. Comparative Study of the Electronic Structure, Phonon Spectra, and Electron-Phonon Interaction of ZrB2 and TiB2. *Phys. Rev. B - Condens. Matter Mater. Phys.* **2013**, *87* (6), 1–13. https://doi.org/10.1103/PhysRevB.87.064305.

(102) Volonakis, G.; Tsetseris, L.; Logothetidis, S. Electronic and Structural Properties of TiB2: Bulk, Surface, and Nanoscale Effects. *Mater. Sci. Eng. B* **2011**, *176* (6), 484–489. https://doi.org/10.1016/j.mseb.2010.03.063.

(103) Kumar, R.; Mishra, M. C.; Sharma, B. K.; Sharma, V.; Lowther, J. E.; Vyas, V.; Sharma, G. Electronic Structure and Elastic Properties of TiB 2 and ZrB 2. *Comput. Mater. Sci.* **2012**, *61*, 150–157. https://doi.org/10.1016/j.commatsci.2012.03.055.

(104) Skoog, D. A. *Principles of Instrumental Analysis*, 7th ed.; Cengage Learning, 2016.

(105) Hitachi. *Hitachi S-4700 SEM Training and Reference Guide*; 2007.

(106) Goldstein, J.; Newbury, D. E.; Joy, D. C.; Lyman, C. E.; Echlin, P.; Lifshin, E.; Sawyer, L.; Michaels, J. R. *Scanning Electron Microscope and X-Ray Microanalysis*; Kluwer Academic Publishers, 2003.

(107) Hawkes, P. W.; Spence, J. C. *Science of Microscopy, Vol. I*; Springer US, 2008.

(108) Huang, T. C.; Predecki, P. K. *Advances in X-Ray Analysis: Grazing-Incidence X-Ray Technique for Surface, Interface and Thin-Film Analysis*; 1997.

(109) Sakata, O.; Nakamura, M. Grazing Incidence X-Ray Diffraction. In *Surface Science Techniques*; Springer US, 2013; pp 165–190.

(110) Hou, X.; Jones, B. T. ICP/OES. In *Encyclopedia of Analytical Chemistry*; John Wiley & Sons, Inc., 2000; pp 9468–9485.

(111) Boss, C. B.; Fredeen, K. J. *Concepts, Instrumentation and Techniques in ICP-OES*; 2004.

(112) Alfonso, E.; Olaya, J.; Cubillos, G. Thin FIlm Growth Through Sputtering Technique and Its Application. In *Crystallization- Science and Technology*; IntechOpen, 2012.

(113) Geiger, S.; Kasian, O.; Mingers, A. M.; Nicley, S. S.; Haenen, K.; Mayrhofer, K. J. J.; Cherevko, S. Catalyst Stability Benchmarking for the Oxygen Evolution Reaction: The Importance of Backing Electrode Material and Dissolution in Accelerated Aging Studies. *ChemSusChem* **2017**, *10* (21), 4140–4143. https://doi.org/10.1002/cssc.201701523.

(114) Xue, Q.; Gao, W.; Zhu, J.; Peng, R.; Xu, Q.; Chen, P.; Chen, Y. Carbon Nanobowls Supported Ultrafine Iridium Nanocrystals: An Active and Stable

Electrocatalyst for the Oxygen Evolution Reaction in Acidic Media. *J. Colloid Interface Sci.* **2018**, *529*, 325–331. https://doi.org/10.1016/j.jcis.2018.06.014.

(115) Kim, D. H.; Park, S. H.; Choi, J.; Yi, M. H.; Kim, H. S. Fabrication of Iridium Oxide Nanoparticles Supported on Activated Carbon Powder by Flashlight Irradiation for Oxygen Evolutions. *Mater. Sci. Eng. B Solid-State Mater. Adv. Technol.* **2015**, *201*, 29–34. https://doi.org/10.1016/j.mseb.2015.06.004.

(116) Lettenmeier, P.; Wang, L.; Golla-Schindler, U.; Gazdzicki, P.; Cañas, N. A.; Handl, M.; Hiesgen, R.; Hosseiny, S. S.; Gago, A. S.; Friedrich, K. A. Nanosized IrOx-Ir Catalyst with Relevant Activity for Anodes of Proton Exchange Membrane Electrolysis Produced by a Cost-Effective Procedure. *Angew. Chemie - Int. Ed.* **2016**, *55* (2), 742–746. https://doi.org/10.1002/anie.201507626.

(117) Sun, K.; Moreno-Hernandez, I. A.; Schmidt, W. C.; Zhou, X.; Crompton, J. C.; Liu, R.; Saadi, F. H.; Chen, Y.; Papadantonakis, K. M.; Lewis, N. S. A Comparison of the Chemical, Optical and Electrocatalytic Properties of Water-Oxidation Catalysts for Use in Integrated Solar-Fuel Generators. *Energy Environ. Sci.* **2017**, *10* (4), 987–1002. https://doi.org/10.1039/c6ee03563a.

(118) Lee, Y.; Suntivich, J.; May, K. J.; Perry, E. E.; Shao-Horn, Y. Synthesis and Activities of Rutile IrO 2 and RuO 2 Nanoparticles for Oxygen Evolution in Acid and Alkaline Solutions. *J. Phys. Chem. Lett.* **2012**, *3* (3), 399–404. https://doi.org/10.1021/jz2016507.

(119) Oh, H.; Nong, H. N.; Reier, T.; Bergmann, A.; Gliech, M.; Ferreira, J.; Arau, D.; Willinger, E.; Schlo, R.; Teschner, D.; et al. Electrochemical Catalyst − Support Effects and Their Stabilizing Role for IrO x Nanoparticle Catalysts during the Oxygen Evolution Reaction. *J Am Chem Soc* **2016**, *138*, 12552–12563. https://doi.org/10.1021/jacs.6b07199.

(120) Geiger, S.; Kasian, O.; Mingers, A. M.; Mayrhofer, K. J. J.; Cherevko, S. Stability Limits of Tin-Based Electrocatalyst Supports. *Sci. Rep.* **2017**, *7* (1), 3–9. https://doi.org/10.1038/s41598-017-04079-9.

(121) Frydendal, R.; Paoli, E. A.; Knudsen, B. P.; Wickman, B.; Malacrida, P.; Stephens, I. E. L.; Chorkendorff, I. Benchmarking the Stability of Oxygen Evolution Reaction Catalysts: The Importance of Monitoring Mass Losses. *ChemElectroChem* **2014**, *1* (12), 2075–2081. https://doi.org/10.1002/celc.201402262.

(122) Badam, R.; Hara, M.; Huang, H. H.; Yoshimura, M. Synthesis and Electrochemical Analysis of Novel IrO2 Nanoparticle Catalysts Supported on Carbon Nanotube for Oxygen Evolution Reaction. *Int. J. Hydrogen Energy* **2018**, *43* (39), 18095–18104. https://doi.org/10.1016/j.ijhydene.2018.08.034.

(123) Mamaca, N.; Mayousse, E.; Arrii-Clacens, S.; Napporn, T. W.; Servat, K.; Guillet, N.; Kokoh, K. B. Electrochemical Activity of Ruthenium and Iridium Based Catalysts for Oxygen Evolution Reaction. *Appl. Catal. B Environ.* **2012**, *111–112*,

376–380. https://doi.org/10.1016/j.apcatb.2011.10.020.

(124) Li, G.; Li, S.; Ge, J.; Liu, C.; Xing, W. Discontinuously Covered IrO2-RuO2@Ru Electrocatalysts for the Oxygen Evolution Reaction: How High Activity and Long-Term Durability Can Be Simultaneously Realized in the Synergistic and Hybrid Nano-Structure. *J. Mater. Chem. A* **2017**, *5* (33), 17221–17229. https://doi.org/10.1039/c7ta05126c.

(125) Pickup, P. G.; Birss, V. I. The Influence of the Aqueous Growth Medium on the Growth Rate, Composition, and Structure of Hydrous Iridium Oxide Films. *J Electrochem Soc* **1988**, *135*, 126–133.

(126) Weber, M. F. Efficiency of Splitting Water with Semiconducting Photoelectrodes. *J. Electrochem. Soc.* **2006**, *131* (6), 1258. https://doi.org/10.1149/1.2115797.

(127) Cherevko, S.; Reier, T.; Zeradjanin, A. R.; Pawolek, Z.; Strasser, P.; Mayrhofer, K. J. J. Stability of Nanostructured Iridium Oxide Electrocatalysts during Oxygen Evolution Reaction in Acidic Environment. *Electrochem. commun.* **2014**, *48*, 81–85. https://doi.org/10.1016/j.elecom.2014.08.027.

(128) Cherevko, S.; Zeradjanin, A. R.; Topalov, A. A.; Kulyk, N.; Katsounaros, I.; Mayrhofer, K. J. J. Dissolution of Noble Metals during Oxygen Evolution in Acidic Media. *ChemCatChem* **2014**, *6* (8), 2219–2223. https://doi.org/10.1002/cctc.201402194.

(129) Tripkovic, D. V.; Strmcnik, D.; van der Vliet, D.; Stamenkovic, V.; Markovic, N. M. The Role of Anions in Surface Electrochemistry. *Faraday Discuss.* **2008**, *140*, 25–40. https://doi.org/10.1080/00031305.1985.10479463.

(130) Mi, Q.; Zhanaidarova, A.; Brunschwig, B. S.; Gray, H. B.; Lewis, N. S. A Quantitative Assessment of the Competition between Water and Anion Oxidation at WO3 Photoanodes in Acidic Aqueous Electrolytes. *Energy Environ. Sci.* **2012**, *5* (2), 5694–5700.

(131) Park, S.; Shao, Y.; Liu, J.; Wang, Y. Oxygen Electrocatalysts for Water Electrolyzers and Reversible Fuel Cells: Status and Perspectives. *Energy Environ. Sci.* **2012**, *5*, 9331–9343.

(132) Trasatti, S. Electrocatalysis by Oxides- Attempt at a Unifying Approach. *J. Electroanal. Chem.* **1980**, *111*, 125–131.

(133) Lyons, M. E. G.; Brandon, M. P. A Comparative Study of the Oxygen Evolution Reaction on Oxidised Nickel, Cobalt and Iron Electrodes in Base. *J. Electroanal. Chem.* **2010**, *641* (1–2), 119–130. https://doi.org/10.1016/j.jelechem.2009.11.024.

(134) Goodenough, J. B.; Manoharan, R.; Paranthaman, M. Surface Protonation and Electrochemical Activity of Oxides in Aqueous Solution. *J Am Chem Soc* **1999**, *112*, 2076–2082. https://doi.org/10.1021/ja00162a006.

(135) Steegstra, P.; Busch, M.; Panas, I.; Ahlberg, E. Revisiting the Redox Properties of

Hydrous Iridium Oxide Films in the Context of Oxygen Evolution. *J. Phys. Chem. C* **2013**, *117* (40), 20975–20981. https://doi.org/10.1021/jp407030r.

(136) Minguzzi, A.; Fan, F. F.; Vertova, A.; Rondinini, S.; Bard, A. J. Dynamic Potential – PH Diagrams Application to Electrocatalysts for Water Oxidation †. *Chem Sci* **2012**, *3*, 217–229. https://doi.org/10.1039/c1sc00516b.

(137) Ooka, H.; Yamaguchi, A.; Takashima, T.; Hashimoto, K.; Nakamura, R. Efficiency of Oxygen Evolution on Iridium Oxide Determined from the PH Dependence of Charge Accumulation. *J. Phys. Chem. C* **2017**, *121* (33), 17873–17881. https://doi.org/10.1021/acs.jpcc.7b03749.

(138) Burke, L. D.; Whelan, D. P. A Voltammetric Investigation of the Charge Storage Reactions of Hydrous Iridium Oxide Layers. *J. Electroanal. Chem.* **1984**, *162*, 121–141.

(139) Kötz, R.; Neff, H.; Stucki, S. Anodic Iridium Oxide Films. *J. Electrochem. Soc.* **1984**, *131* (1), 72. https://doi.org/10.1149/1.2115548.

(140) Yagi, M.; Tomita, E.; Kuwabara, T. Remarkably High Activity of Electrodeposited IrO 2 Film for Electrocatalytic Water Oxidation. *J. Electroanal. Chem.* **2005**, *579*, 83–88. https://doi.org/10.1016/j.jelechem.2005.01.030.

(141) Swanson, H. E.; Morris, M. C.; Evans, E. H. *Standard X-Ray Diffraction Powder Patterns: Section 4. Data for 103 Substances*; 1966.

(142) Mozota, J.; Conway, B. E. Modification of Apparent Electrocatalysis for Anodic Chlorine Evolution on Electrochemically Conditioned Oxide Films at Iridium Anodes. *J Electrochem Soc* **1981**, *128* (20), 2142–2149.

(143) Trasatti, S.; Petrii, O. A. Real Surface Area Measurements. *Pure Appl. Chem.* **1991**, *63* (5), 711–734. https://doi.org/10.1351/pac199163050711.

(144) Harriman, A.; Pickering, I. J.; Thomas, J. M.; Christensen, P. A. Metal Oxides as Heterogeneous Catalysts for Oxygen Evolution under Photochemical Conditions. *J. Chem. Soc. Faraday Trans. 1 Phys. Chem. Condens. Phases* **1988**, *84* (8), 2795–2806. https://doi.org/10.1039/F19888402795.

(145) Burke, L. D.; McCarthy, F.; O'Meara, T. O. The Oxygen Electrode Part 3. Inhibition of the Oxygen Evolution Reaction. *J Chem Soc Faraday Trans* **1971**, *604*, 1086–1092.

(146) Burke, L. D.; Healy, J. F. The Importance of Reactive Surface Groups with Regard to the Electrocatalytic Behaviour of Oxide Anodes. *J Electroanal Chem* **1981**, *124*, 327–332.

(147) Boodts, J. C. F.; Trasatti, S. Hydrogen Evolution on Iridium Oxide Cathodes. *J. Appl. Electrochem.* **1989**, *19* (2), 255–262. https://doi.org/10.1007/BF01062309.

(148) Li, X.; Hao, X.; Guan, G. Nanostructured Catalysts for Electrochemical Water Splitting : Current State and Prospects. *J Mater Chem A* **2016**, *4*, 11973–12000.

https://doi.org/10.1039/c6ta02334g.

(149) Kang, D.; Kim, T. W.; Kubota, S. R.; Cardiel, A. C.; Cha, H. G.; Choi, K. S. Electrochemical Synthesis of Photoelectrodes and Catalysts for Use in Solar Water Splitting. *Chem. Rev.* **2015**, *115* (23), 12839–12887. https://doi.org/10.1021/acs.chemrev.5b00498.

(150) Jensen, S. H.; Larsen, P. H.; Mogensen, M. Hydrogen and Synthetic Fuel Production from Renewable Energy Sources. *Int. J. Hydrogen Energy* **2007**, *32* (15 SPEC. ISS.), 3253–3257. https://doi.org/10.1016/j.ijhydene.2007.04.042.

(151) Dincer, I.; Zamfirescu, C. Hydrogen Production by Electrical Energy. In *Sustainable Hydrogen Production*; Elsevier Inc., 2017; pp 99–161.

(152) Sun, Z.; Ma, T.; Tao, H.; Fan, Q.; Han, B. Fundamentals and Challenges of Electrochemical CO2 Reduction Using Two-Dimensional Materials. *CHEM* **2017**, *3* (4), 560–587. https://doi.org/10.1016/j.chempr.2017.09.009.

(153) Wu, J.; Huang, Y.; Ye, W.; Li, Y. CO2 Reduction: From Electrochemical to Photoelectrochemical Approach. *Adv Sci* **2017**, *4*, 1700194.

(154) Kyriakou, V.; Garagounis, I.; Vasileiou, E.; Vourros, A.; Stoukides, M. Progress in the Electrochemical Synthesis of Ammonia. *Catal. Today* **2017**, *286*, 2–13. https://doi.org/10.1016/j.cattod.2016.06.014.

(155) Li, J.; Güttinger, R.; Moré, R.; Song, F.; Wan, W.; Patzke, G. R. Frontiers of Water Oxidation: The Quest for True Catalysts. *Chem. Soc. Rev.* **2017**, *46* (20), 6124–6147. https://doi.org/10.1039/c7cs00306d.

(156) Shao, Q.; Yang, J.; Huang, X. The Design of Water Oxidation Electrocatalysts from Nanoscale Metal – Organic Frameworks. *Chem Eur J* **2018**, *24*, 15143–15155. https://doi.org/10.1002/chem.201801572.

(157) Mahala, C.; Basu, M. Nanosheets of NiCo2O4/NiO as Efficient and Stable Electrocatalyst for Oxygen Evolution Reaction. *ACS Omega* **2017**, *2*, 7559–7567. https://doi.org/10.1021/acsomega.7b00957.

(158) Regier, T.; Wei, F.; Dai, H. An Advanced Ni − Fe Layered Double Hydroxide Electrocatalyst for Water Oxidation. *J Am Chem Soc* **2013**, *135*, 8452–8455. https://doi.org/10.1021/ja4027715.

(159) Lu, X.; Zhao, C. Electrodeposition of Hierarchically Structured Three-Dimensional Nickel-Iron Electrodes for Efficient Oxygen Evolution at High Current Densities. *Nat. Commun.* **2015**, *6*, 1–7. https://doi.org/10.1038/ncomms7616.

(160) Jeong, D.; Jin, K.; Jerng, S. E.; Seo, H.; Kim, D.; Nahm, S. H.; Kim, S. H.; Nam, K. T. Mn5O8 Nanoparticles as Efficient Water Oxidation Catalysts at Neutral PH. *ACS Catal.* **2015**, *5* (8), 4624–4628. https://doi.org/10.1021/acscatal.5b01269.

(161) Yang, L.; Liu, D.; Hao, S.; Kong, R.; Asiri, A. M.; Zhang, C.; Sun, X. A Cobalt-

Borate Nanosheet Array: An Efficient and Durable Non-Noble-Metal Electrocatalyst for Water Oxidation at near Neutral PH. *J. Mater. Chem. A* **2017**, *5* (16), 7305–7308. https://doi.org/10.1039/c7ta00982h.

(162) Roger, I.; Symes, M. D. Efficient Electrocatalytic Water Oxidation at Neutral and High PH by Adventitious Nickel at Nanomolar Concentrations. *J. Am. Chem. Soc.* **2015**, *137* (43), 13980–13988. https://doi.org/10.1021/jacs.5b08139.

(163) Orlandi, M.; Dalle Carbonare, N.; Caramori, S.; Bignozzi, C. A.; Berardi, S.; Mazzi, A.; El Koura, Z.; Bazzanella, N.; Patel, N.; Miotello, A. Porous versus Compact Nanosized Fe(III)-Based Water Oxidation Catalyst for Photoanodes Functionalization. *ACS Appl. Mater. Interfaces* **2016**, *8* (31), 20003–20011. https://doi.org/10.1021/acsami.6b05135.

(164) Frydendal, R.; Paoli, E. A.; Chorkendorff, I.; Rossmeisl, J.; Stephens, I. E. L. Toward an Active and Stable Catalyst for Oxygen Evolution in Acidic Media: Ti-Stabilized MnO 2. *Adv Energy Mater* **2015**, *5*. https://doi.org/10.1002/aenm.201500991.

(165) Kariofillis, G. K.; Kiourtsidis, G. E.; Tsipas, D. N. Corrosion Behavior of Borided AISI H13 Hot Work Steel. *Surf Coat. Technol* **2006**, *201*, 19–24. https://doi.org/10.1016/j.surfcoat.2005.10.025.

(166) Martini, C.; Palombarini, G.; Poli, G.; Prandstraller, D. Sliding and Abrasive Wear Behaviour of Boride Coatings. *wear* **2004**, *256*, 608–613. https://doi.org/10.1016/j.wear.2003.10.003.

(167) Tavakoli, H.; Khoie, S. M. M. An Electrochemical Study of the Corrosion Resistance of Boride Coating Obtained by Thermo-Reactive Diffusion. *Mater. Chem. Phys.* **2010**, *124* (2–3), 1134–1138. https://doi.org/10.1016/j.matchemphys.2010.08.047.

(168) Carenco, S.; Portehault, D. Nanoscaled Metal Borides and Phosphides : Recent Developments and Perspectives. *Chem. Rev.* **2013**, *113*, 7981. https://doi.org/10.1021/cr400020d.

(169) Marie, J.; Nsanzimana, V.; Reddu, V.; Peng, Y.; Huang, Z. Ultrathin Amorphous Iron – Nickel Boride Nanosheets for Highly Efficient Electrocatalytic Oxygen Production. *Chem Eur J* **2018**, *24*, 18502–18511. https://doi.org/10.1002/chem.201802092.

(170) Masa, J.; Weide, P.; Peeters, D.; Sinev, I.; Xia, W.; Sun, Z.; Somsen, C.; Muhler, M.; Schuhmann, W. Amorphous Cobalt Boride (Co 2B) as a Highly Efficient Nonprecious Catalyst for Electrochemical Water Splitting: Oxygen and Hydrogen Evolution. *Adv Energy Mater* **2016**, *6*, 1–10. https://doi.org/10.1002/aenm.201502313.

(171) Wdowik, U. D.; Twardowska, A.; Rajchel, B. B. Vibrational Spectroscopy of Binary Titanium Borides : First-Principles and Experimental Studies. *Adv. Condens. Matter Phys.* **2017**.

(172) Guo, S.; Meng, Q.; Zhao, X.; Wei, Q.; Xu, H. Design and Fabrication of a Metastable β -Type Titanium Alloy with Ultralow Elastic Modulus and High Strength. *Nat. Publ. Gr.* **2015**, 1–9. https://doi.org/10.1038/srep14688.

(173) Mi, Q.; Coridan, R. H.; Brunschwig, B. S.; Gray, H. B.; Lewis, N. S. Photoelectrochemical Oxidation of Anions by WO3 in Aqueous and Nonaqueous Electrolytes. *Energy Env. Sci* **2013**, *6*, 2646–2653. https://doi.org/10.1039/c3ee40712h.

(174) Paiva, J. M.; Shalaby, M. A. M.; Chowdhury, M.; Shuster, L.; Chertovskikh, S.; Covelli, D.; Junior, E. L.; Stolf, P.; Elfizy, A.; Bork, C. A. S.; et al. Tribological and Wear Performance of Carbide Tools with TiB2 PVD Coating under Varying Machining Conditions of TiAl6V4 Aerospace Alloy. *Coatings* **2017**, *7* (11), 187. https://doi.org/10.3390/coatings7110187.

(175) Andrievskii, R. A.; Shul, Y. M.; Volkova, L. S.; Korobov, I. I.; Dremova, N. N.; Kabachkov, E. N.; Kalinnikov, G. V; Shilkin, S. P. Oxidation Behavior of TiB 2 Micro- and Nanoparticles. *Inorg Mater* **2016**, *52* (7), 686–693. https://doi.org/10.1134/S0020168516070013.

(176) Prakash, B.; Ftikos, C.; Pierre, J. Fretting Wear Behavior of PVD TiB2 Coatings. *Surf. Coatings Technol.* **2002**, *154*, 182–188.

(177) Korobov, I. I.; Kalinnikov, G. V.; Ivanov, A. V.; Dremova, N. N.; Vinokurov, A. A.; Shilkin, S. P.; Andrievskii, R. A. Behavior of Titanium Diboride Nanofilms and Nanopowders in Hydrochloric Acid Solutions. *Inorg. Mater.* **2017**, *53* (5), 548–551. https://doi.org/10.1134/s0020168517050120.

(178) Korobov, I. I.; Kalinnikov, G. V; Ivanov, A. V; Dremova, N. N.; Andrievski, R. A.; Shilkin, S. P. Corrosion Resistance of Nanostructured Films of Titanium Diboride in Mineral Acid Solutions. *Prot Met Phys Chem Surfaces* **2016**, *52* (4), 618–621. https://doi.org/10.1134/S2070205116040171.

(179) Oudrhiri-Hassani, F.; Presmanes, L.; Barnabé, A.; Tailhades, P. Microstructure, Porosity and Roughness of RF Sputtered Oxide Thin Films: Characterization and Modelization. *Appl. Surf. Sci.* **2008**, *254* (18), 5796–5802. https://doi.org/10.1016/j.apsusc.2008.03.149.

(180) BATTAGLIN, G.; CARNERA, A.; LODI, G.; GIORGI, E.; DAGHETTI, A.; TRASATTI, S. EFFECT OF THE SUPPORT ON THE SURFACE PROPERTIES OF RUTHENIUM DIOXIDE ON SILICA GLASS. *J. Chem. Soc. Faraday Trans.* **1984**, *1* (27), 913–917. https://doi.org/10.1002/chin.198427023.

(181) Ganassin, A.; Maljusch, A.; Colic, V.; Spanier, L.; Brandl, K.; Schuhmann, W.; Bandarenka, A. Benchmarking the Performance of Thin-Film Oxide Electrocatalysts for Gas Evolution Reactions at High Current Densities. *ACS Catal.* **2016**, *6* (5), 3017–3024. https://doi.org/10.1021/acscatal.6b00455.

## APPENDIX A. COPYRIGHT PERMISSION LETTER

# JOHN WILEY AND SONS LICENSE TERMS AND CONDITIONS

Apr 26, 2019

This Agreement between Maxine Kirshenbaum ("You") and John Wiley and Sons ("John Wiley and Sons") consists of your license details and the terms and conditions provided by John Wiley and Sons and Copyright Clearance Center.

| | |
|---|---|
| License Number | 4565520488895 |
| License date | Apr 10, 2019 |
| Licensed Content Publisher | John Wiley and Sons |
| Licensed Content Publication | ChemCatChem |
| Licensed Content Title | Electrochemical Water Oxidation in Acidic Solution Using Titanium Diboride (TiB2) Catalyst |
| Licensed Content Author | Maxine J. Kirshenbaum, Matthias H. Richter, Mita Dasog |
| Licensed Content Date | Jan 15, 2019 |
| Licensed Content Volume | 0 |
| Licensed Content Issue | 0 |
| Licensed Content Pages | 6 |
| Type of Use | Dissertation/Thesis |
| Requestor type | Author of this Wiley article |
| Format | Print and electronic |
| Portion | Full article |
| Will you be translating? | No |
| Title of your thesis / dissertation | ACID-STABLE ELECTROCATALYSTS FOR THE OXYGEN EVOLUTION REACTION |
| Expected completion date | Aug 2019 |
| Expected size (number of pages) | |
| Requestor Location | Maxine Kirshenbaum<br>2616 Windsor Street<br><br>Halifax, NS B3K 5C8<br>Canada<br>Attn: Maxine Kirshenbaum |
| Publisher Tax ID | EU826007151 |
| Total | **0.00 CAD** |
| Terms and Conditions | |

**TERMS AND CONDITIONS**

This copyrighted material is owned by or exclusively licensed to John Wiley & Sons, Inc. or one of its group companies (each a"Wiley Company") or handled on behalf of a society with which a Wiley Company has exclusive publishing rights in relation to a particular work (collectively "WILEY"). By clicking "accept" in connection with completing this licensing transaction, you agree that the following terms and conditions apply to this transaction (along with the billing and payment terms and conditions established by the Copyright Clearance Center Inc., ("CCC's Billing and Payment terms and conditions"), at the time that you opened your RightsLink account (these are available at any time at http://myaccount.copyright.com).

**Terms and Conditions**

- The materials you have requested permission to reproduce or reuse (the "Wiley Materials") are protected by copyright.

- You are hereby granted a personal, non-exclusive, non-sub licensable (on a stand-alone basis), non-transferable, worldwide, limited license to reproduce the Wiley Materials for the purpose specified in the licensing process. This license, **and any CONTENT (PDF or image file) purchased as part of your order**, is for a one-time use only and limited to any maximum distribution number specified in the license. The first instance of republication or reuse granted by this license must be completed within two years of the date of the grant of this license (although copies prepared before the end date may be distributed thereafter). The Wiley Materials shall not be used in any other manner or for any other purpose, beyond what is granted in the license. Permission is granted subject to an appropriate acknowledgement given to the author, title of the material/book/journal and the publisher. You shall also duplicate the copyright notice that appears in the Wiley publication in your use of the Wiley Material. Permission is also granted on the understanding that nowhere in the text is a previously published source acknowledged for all or part of this Wiley Material. Any third party content is expressly excluded from this permission.

- With respect to the Wiley Materials, all rights are reserved. Except as expressly granted by the terms of the license, no part of the Wiley Materials may be copied, modified, adapted (except for minor reformatting required by the new Publication), translated, reproduced, transferred or distributed, in any form or by any means, and no derivative works may be made based on the Wiley Materials without the prior permission of the respective copyright owner.**For STM Signatory Publishers clearing permission under the terms of the STM Permissions Guidelines only, the terms of the license are extended to include subsequent editions and for editions in other languages, provided such editions are for the work as a whole in situ and does not involve the separate exploitation of the permitted figures or extracts,** You may not alter, remove or suppress in any manner any copyright, trademark or other notices displayed by the Wiley Materials. You may not license, rent, sell, loan, lease, pledge, offer as security, transfer or assign the Wiley Materials on a stand-alone basis, or any of the rights granted to you hereunder to any other person.

- The Wiley Materials and all of the intellectual property rights therein shall at all times remain the exclusive property of John Wiley & Sons Inc, the Wiley Companies, or their respective licensors, and your interest therein is only that of having possession of and the right to reproduce the Wiley Materials pursuant to Section 2 herein during the continuance of this Agreement. You agree that you own no right, title or interest in or to the Wiley Materials or any of the intellectual property rights therein. You shall have no rights hereunder other than the license as provided for above in Section 2. No right, license or interest to any trademark, trade name, service mark or other branding ("Marks") of WILEY or its licensors is granted hereunder, and you agree that you shall not assert any such right, license or interest with respect thereto

- NEITHER WILEY NOR ITS LICENSORS MAKES ANY WARRANTY OR REPRESENTATION OF ANY KIND TO YOU OR ANY THIRD PARTY, EXPRESS, IMPLIED OR STATUTORY, WITH RESPECT TO THE MATERIALS OR THE ACCURACY OF ANY INFORMATION CONTAINED IN THE MATERIALS, INCLUDING, WITHOUT LIMITATION, ANY IMPLIED WARRANTY OF MERCHANTABILITY, ACCURACY, SATISFACTORY QUALITY, FITNESS FOR A PARTICULAR PURPOSE, USABILITY, INTEGRATION OR NON-INFRINGEMENT AND ALL SUCH WARRANTIES ARE HEREBY EXCLUDED BY WILEY AND ITS LICENSORS AND WAIVED BY YOU.

- WILEY shall have the right to terminate this Agreement immediately upon breach of this Agreement by you.

- You shall indemnify, defend and hold harmless WILEY, its Licensors and their respective directors, officers, agents and employees, from and against any actual or threatened claims, demands, causes of action or proceedings arising from any breach of this Agreement by you.

- IN NO EVENT SHALL WILEY OR ITS LICENSORS BE LIABLE TO YOU OR ANY OTHER PARTY OR ANY OTHER PERSON OR ENTITY FOR ANY SPECIAL, CONSEQUENTIAL, INCIDENTAL, INDIRECT, EXEMPLARY OR PUNITIVE DAMAGES, HOWEVER CAUSED, ARISING OUT OF OR IN CONNECTION WITH THE DOWNLOADING, PROVISIONING, VIEWING OR USE OF THE MATERIALS REGARDLESS OF THE FORM OF ACTION, WHETHER FOR BREACH OF CONTRACT, BREACH OF WARRANTY, TORT, NEGLIGENCE, INFRINGEMENT OR OTHERWISE (INCLUDING, WITHOUT LIMITATION, DAMAGES BASED ON LOSS OF PROFITS, DATA, FILES, USE, BUSINESS OPPORTUNITY OR CLAIMS OF THIRD PARTIES), AND WHETHER OR NOT THE PARTY HAS BEEN ADVISED OF THE POSSIBILITY OF SUCH DAMAGES. THIS LIMITATION SHALL APPLY NOTWITHSTANDING ANY FAILURE OF ESSENTIAL PURPOSE OF ANY LIMITED REMEDY PROVIDED HEREIN.

- Should any provision of this Agreement be held by a court of competent jurisdiction to be illegal, invalid, or unenforceable, that provision shall be deemed amended to achieve as nearly as possible the same economic effect as the original provision, and the legality, validity and enforceability of the remaining provisions of this Agreement shall not be affected or impaired thereby.

- The failure of either party to enforce any term or condition of this Agreement shall not constitute a waiver of either party's right to enforce each and every term and condition of this Agreement. No breach under this agreement shall be deemed waived or

excused by either party unless such waiver or consent is in writing signed by the party granting such waiver or consent. The waiver by or consent of a party to a breach of any provision of this Agreement shall not operate or be construed as a waiver of or consent to any other or subsequent breach by such other party.

- This Agreement may not be assigned (including by operation of law or otherwise) by you without WILEY's prior written consent.
- Any fee required for this permission shall be non-refundable after thirty (30) days from receipt by the CCC.
- These terms and conditions together with CCC's Billing and Payment terms and conditions (which are incorporated herein) form the entire agreement between you and WILEY concerning this licensing transaction and (in the absence of fraud) supersedes all prior agreements and representations of the parties, oral or written. This Agreement may not be amended except in writing signed by both parties. This Agreement shall be binding upon and inure to the benefit of the parties' successors, legal representatives, and authorized assigns.
- In the event of any conflict between your obligations established by these terms and conditions and those established by CCC's Billing and Payment terms and conditions, these terms and conditions shall prevail.
- WILEY expressly reserves all rights not specifically granted in the combination of (i) the license details provided by you and accepted in the course of this licensing transaction, (ii) these terms and conditions and (iii) CCC's Billing and Payment terms and conditions.
- This Agreement will be void if the Type of Use, Format, Circulation, or Requestor Type was misrepresented during the licensing process.
- This Agreement shall be governed by and construed in accordance with the laws of the State of New York, USA, without regards to such state's conflict of law rules. Any legal action, suit or proceeding arising out of or relating to these Terms and Conditions or the breach thereof shall be instituted in a court of competent jurisdiction in New York County in the State of New York in the United States of America and each party hereby consents and submits to the personal jurisdiction of such court, waives any objection to venue in such court and consents to service of process by registered or certified mail, return receipt requested, at the last known address of such party.

**WILEY OPEN ACCESS TERMS AND CONDITIONS**

Wiley Publishes Open Access Articles in fully Open Access Journals and in Subscription journals offering Online Open. Although most of the fully Open Access journals publish open access articles under the terms of the Creative Commons Attribution (CC BY) License only, the subscription journals and a few of the Open Access Journals offer a choice of Creative Commons Licenses. The license type is clearly identified on the article.

**The Creative Commons Attribution License**

The Creative Commons Attribution License (CC-BY) allows users to copy, distribute and transmit an article, adapt the article and make commercial use of the article. The CC-BY license permits commercial and non-

**Creative Commons Attribution Non-Commercial License**

The Creative Commons Attribution Non-Commercial (CC-BY-NC)License permits use, distribution and reproduction in any medium, provided the original work is properly cited and is not used for commercial purposes.(see below)

**Creative Commons Attribution-Non-Commercial-NoDerivs License**

The Creative Commons Attribution Non-Commercial-NoDerivs License (CC-BY-NC-ND) permits use, distribution and reproduction in any medium, provided the original work is properly cited, is not used for commercial purposes and no modifications or adaptations are made. (see below)

**Use by commercial "for-profit" organizations**

Use of Wiley Open Access articles for commercial, promotional, or marketing purposes requires further explicit permission from Wiley and will be subject to a fee.

Further details can be found on Wiley Online Library http://olabout.wiley.com/WileyCDA/Section/id-410895.html

**Other Terms and Conditions:**